JAN 0

orml

OAK RIDGE NATIONAL LABORATORY

MARTIN MARIETTA

DEVELOPMENT OF PERFORMANCE MODELS FOR THICK COMPOSITES IN COMPRESSION

H. W. Blake
H. J. Grimsby
J. M. Starbuck
D. E. Welch

November 1991

Applied Technology Division

DEVELOPMENT OF PERFORMANCE MODELS FOR THICK COMPOSITES IN COMPRESSION

H. W. Blake
H. J. Grimsby
J. M. Starbuck
D. E. Welch

Date Published—November 1991

CONTENTS

FIGURES

TABLES

ABSTRACT

This report details initial activities and results from an investigation into the failure of thick-section composite cylinders loaded in compression. The efforts are aimed at the development of models for predicting cylinder performance based on composite material strengths derived from ring and cylinder tests of unidirectional materials. Initial results indicate that existing failure theories are applicable provided that material strength allowables are based on representative tests, and that appropriate solutions for cylinder stresses are used. Both the failure criteria and stress solution must allow for the three-dimensional stress state and for the discrete layer construction. Predictions for an initial test cylinder, which achieved a record pressure in hydrotest, are consistent with the observed performance. Performance model results obtained for a range of laminate constructions indicate this design to be optimum. Improvements in test fixturing also contributed to the record performance for this first cylinder. This work is sponsored by the Director as a three-year project funded from the Oak Ridge National Laboratory seed-money program.

INTRODUCTION

Basic to this Oak Ridge National Laboratory (ORNL) project is the understanding of the operative failure modes of composites under compression and the definition of designs that have optimum compression performance. Failure modes and design are interdependent because composites contain a polymer component and a fiber component which can be fabricated with a variety of laminate designs that give a variety of properties, most of which are directional. Added to this, is a variety of candidate fibers, each having different strength and modulus properties. Also, two or more fiber types can be blended to afford other design options. The flexibility for designing composites to meet specific requirements is great, as is the complexity. This requires analysis at the micromechanical level using sophisticated codes that will require development or modification.

In work, to date, by a variety of organizations in the United States, experience has fallen far short of analytical predictions.[1-4] Also, stress values in test cylinders have not achieved strengths achieved on flat coupon tests.[3,5] The overall difficulty of the task explains, in part, the current lack of success. However, a major contributing factor to the current lack of understanding is the complexity of the fracture process in thick-section composites. The short time scale of the fracture propagation across the test specimen has prevented the identification of the initiating modes of failure. Success in this area will require careful experimentation and the parallel development of supporting failure theories.

The development of a failure prediction model for composites subjected to compressive loading requires a combined experimental/analytical approach. Analytical tools are needed for the determination of ply-level stress states and elastic stability and the application of various failure criteria. The validity of a certain failure criterion can be established by testing a series of articles to identify the possible failure modes for a given specimen configuration. The results of the experimental program can then be correlated with the analytic predictions for the stresses and deformations.

At present, standardized test methods for cylinders and rings have not been developed. The variety of test methods and fixturing has contributed to the variability in results for compression performance of thick section cylinders. Standardized test methods will be required before consistent data can be obtained.

1. DESIGN/FAILURE ANALYSIS

The objective of this task is the development of the analytical methodology for design/analysis of the composite test articles for compression testing. These include test cylinders loaded in external hydrostatic compression and rings loaded in radial compression. The activities include the analytical investigations into the stresses and modes of failure of thick-section composite cylinders and rings, the formulation of predictive models for performance, and finally the definition of designs that have optimum compression performance.

The project deliverables under this task are the analytical codes for designing composite cylinders for optimum performance under compression as well as the analysis results for the various test articles.

The approach taken is an iterative design/analysis/test sequence that will be repeated on a series of demonstration test articles (see Fig. 1-1). This repetitive sequence, together with the evolution of the various test articles, provides a basis for an optimized design. The initial phase of this study will establish failure modes of selected test articles. This will involve analysis using state-of-the art analytical and numerical techniques for determination of internal stresses and elastic stability. Closed-form analytical solutions for stress and buckling of thick-section composite cylinders will be developed. Finite element stress analysis methods will be applied at the ply level to validate analytical solutions and to extend the range of solutions to complex boundary conditions. This will lead to the development of innovative solution methods for large-scale models and postprocessing of results. The product of this research will be a failure prediction model that couples stress analysis and failure analysis on a ply-by-ply basis.

CYLINDER TEST PROGRAM
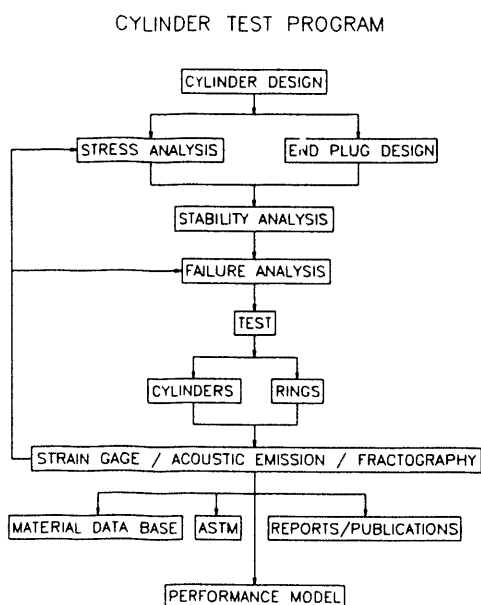
Fig. 1-1. Cylinder test program flow chart.

Material selection for the test articles was based on earlier projects involving tests of rings and cylinders.[5-9] These earlier efforts involved both S-Glass and graphite composite materials. On the basis of these test results, two fibers and one matrix material were selected for this project. These were IM6 graphite and S-Glass fibers and ERL-2258/MPDA matrix.

The selected materials will be tested during a three-year evaluation. The plan was to evaluate each fiber with the selected resin for a one-year period. During the first year, the IM6/ERL-2258 system was tested. The second year focused on the S-Glass/ERL-2258 system. In the third year, the best performing material will be selected between these two. Hybrids of the two fibers will also be considered. The selection will be based on the maximum achievable compression strengths and cylinder weight/displacement ratios. The best material will be tested during the third year to investigate its ultimate performance and modes of failure. The emphasis will be on identification of the operational failure modes and the validation of the performance model rather than on optimizing the cylinder design for a particular application.

The selected materials will be tested in unidirectional and cross-ply laminated cylinders. The unidirectional cylinders will be all-circ-wound construction. The cross-ply cylinders will be made with several different ply ratios to investigate the effect of ply ratio on compression strength and mode of failure. These cylinders will be made with a dispersed alternating repeating pattern to simplify the processing and to limit the variables for this initial investigation. This also will provide information on the buckling of cylinders for a range of ply ratios.

The unidirectional material cylinders are expected to fail in a matrix dominated mode (i.e., transverse compression or shear). The circ-wound cylinders should, therefore, fail in an axial compression mode rather than a circumferential mode. Results from these tests will also provide estimates of the transverse compression strength under hydrostatic loading conditions. These results will be used to revise the transverse strength for the unidirectional plies in the cross-ply laminated cylinders. The initial values of transverse strength were obtained from tests on thin flat coupons by using the Celanese test fixture. These data are not expected to be accurate for thick-section laminated cylinders because of differences in process, specimen size, and loading conditions.

1.1 ANALYTIC STRESS ANALYSIS

This subtask consists of the acquisition and development of analytic solutions for stresses and deformations of thick-section laminated composite cylinders. Analytic, closed-form solutions are being pursued because of advantages of accuracy and flexibility over other solution methods. Analytic solutions are potentially more accurate than numerical methods such as finite element and finite difference. Also, analytic solutions are computationally fast once the equations are developed and coded for solution. Analytic solutions can be evaluated computationally much faster than the numerical techniques. This speed of solution facilitates the design iteration process whenever a large number of cases or range of parameters is to be explored.

During the first year of the project, three existing cylinder models were acquired in coded form and installed on various mainframe and desktop computers. In addition, a new code was developed and installed on a PC.

The codes were validated by executing several sample problems with each code and comparing solution results. Analytic results were also compared with finite element solutions. The applicability of these analytic solutions to actual test assemblies, consisting of the cylinder together with metal end closures, was also investigated. The analytic solutions are restricted to idealized deformations and boundary conditions and are, therefore, applicable only to regions of the cylinder sufficiently far removed from the ends. The influence of the end closures on cylinder deformations was investigated to define the region of applicability of the analytic solutions. Finite element models of the test assemblies were constructed and solutions were obtained to quantify the effect of the end closures on cylinder stresses. These results defined the extent of axial bending and shear stresses near each end of the cylinder and defined the axial length of the cylinder mid-region where the end effects can be neglected. This, in turn, defined the region of applicability of the analytic solutions. Analytic results were compared to the finite element results from elements located at the cylinder mid-region for each test assembly.

Analytic solutions for stress were obtained at the ply level. Additional results from using smeared elastic properties were obtained to provide the composite stresses and for comparison to the ply-by-ply solution. Layer stress values were referred to principal material coordinates for the ply-level solutions.

Initial finite element solutions were obtained by using smeared elastic properties only. Only exploratory cases were done at the ply level. Extending these initial small models to an entire cylinder model will require extreme mesh refinement and associated increase in number of solution degrees of freedom. In addition, execution of these large models will consume significant computing resources. However, because of the current limitations of the analytic solutions, only the finite element method is available to evaluate ply stresses in the regions adjacent to the end closures. Additional finite element analyses will be performed to explore this approach and to provide the ply stress values for comparison with the analytic solution at points away from the cylinder ends.

Selected analytic solutions were interfaced to various failure criteria (see Sect. 1.4). The resulting failure codes were applied to regions of the cylinder where validity had been established on the basis of finite element results. Failure analyses of various test articles were performed, and the analytic results were compared with experimental results.

In the present study, the model problem of a laminated composite cylinder subjected to hydrostatic loading is investigated. The geometry of a laminated cylinder is shown in Figure 1.1-1, where the cylindrical coordinate system, x, θ, and r, represent the axial, circumferential, and radial directions, respectively. The cylinder has a total length of L, thickness, h, and mean radius, R. For hydrostatic loading the cylinder is subjected to a uniform external lateral pressure, p_o, and an axial compressive force, F_{ax}, due to the hydrostatic pressure acting on the end plugs.
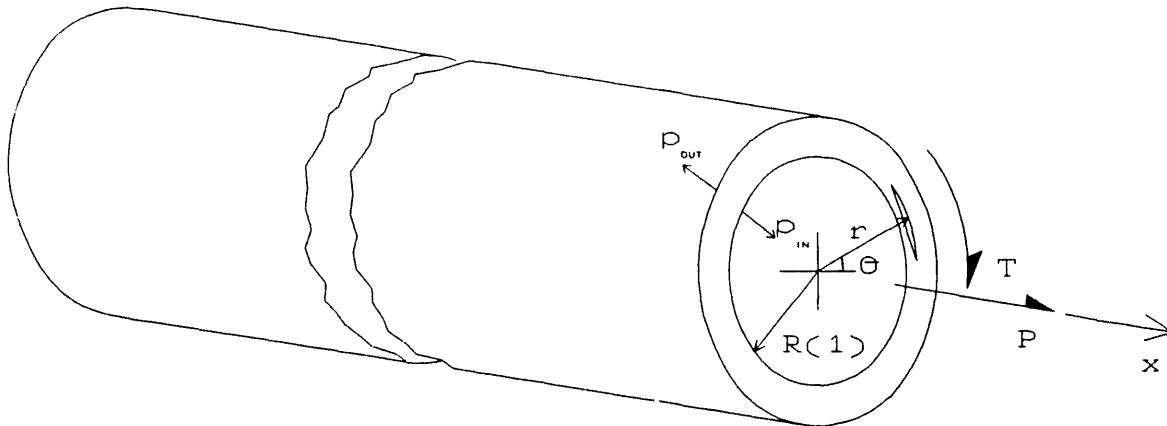
Fig. 1.1-1. Cylinder geometry and loading.

1.1.1 Solution Methods

The ply-level stresses and deformations in thick-wall laminated composite cylinders were determined in this investigation by acquiring existing analytic solutions in coded form and by developing a new code. The new code alleviated various shortcomings that were found to be present in the existing codes. Fortran source codes were obtained from M. W. Hyer at Virginia Polytechnic Institute and State University and from A. K. Roy at University of Dayton Research Institute. Hyer's program, ELCYL, and Roy's program, CYLIN, were both successfully compiled on a VAX computer and a PC. A third code, CYLAN, was acquired from the University of Delaware Engineering Research Center for Composites Manufacturing Science and Engineering (CCM). This code was written in BASIC and successfully installed on a PC. The newly developed code and the three acquired codes were all based on closed-form solutions to the problem of a laminated cylinder having idealized geometry, loading, and boundary conditions. The range of applicability of these solutions was examined by comparing their results to the results from a finite element analysis. A discussion of the solution methodology used in these codes and a brief description of their program capabilities follows.

The expressions for the stresses and displacements in the program developed by M. W. Hyer[10] were derived fro⌐ ⌐ the governing elasticity equations for a cylindrical anisotropic body. Axisymmetric thermal and mechanical loading were considered so the stresses, strains, and displacements were independent of the circumferential coordinate. Also, a state of generalized plane deformation was assumed so the stresses were independent of the axial coordinate. Consequently, the solution is only valid at points away from the ends of the cylinder and localized effects due to the end plugs cannot be accounted for. The solution for a single layer was obtained in terms of the unknown constants resulting from integration of the governing equations.

For a laminated cylinder the problem is reduced to solving a system of linear algebraic equations for the unknown constants in each layer by imposing traction and displacement continuity conditions at each interface, traction boundary conditions at the inner and outer radii, and conditions that involved integration of tractions over the cross-section. The specified tractions on the boundary considered in the program corresponded to internal and external lateral pressure, axial force, and torque. For the case of hydrostatic pressure, the axial component of stress due to the end plugs is input as a compressive axial force. The program calculates stresses in both the cylindrical and principal material coordinate systems, and total (thermal + mechanical) and mechanical strains at three points in each layer. The program is capable of analyzing hybrid cylinders, but numerical difficulties were encountered for isotropic layers. In the case of an isotropic layer, the roots to the characteristic equation are repeated and equal to 1.0, which in Hyer's formulation resulted in a division by zero. The same numerical difficulties occurred for axial layers because they are transversely isotropic in the $r\theta$-plane, i.e., $E_r = E_\theta$. Hyer overcomes this problem by specifying E_r to be slightly different from E_θ.

The stresses and displacements in A. K. Roy's[11] code were determined by solving the governing elasticity equations for a cylindrically orthotropic cylinder. The state of stress was assumed to be generalized plane strain and axisymmetric. For helical wound layers, adjacent $\pm\theta$ lay-ups, which act as an orthotropic unit, were assumed. In Roy's formulation, a layered analysis was performed, and the solution to the governing equations was reduced to solving a system of linear algebraic equations for the unknown interfacial normal tractions. The mechanical loadings considered in the analysis were uniform internal and external lateral pressures and an axial force. The program assumed hydrostatic loading so the specified value of the axial force was in addition to the axial compressive stress due to the hydrostatic pressure acting on the end plugs. The calculation of the axial force associated with the hydrostatic pressure was modified in the program to use the outer radius of the cylinder instead of the mean radius. The use of the mean radius for this calculation is only valid for thin-wall cylinders. The analysis of a laminated cylinder subjected to an applied torque and/or thermal loading cannot be performed.

Roy's program was capable of analyzing hybrid cylinders by defining different layer properties in a material data file. However, the same numerical difficulties as discussed above for Hyer's code were encountered if isotropic properties were specified in the data file and/or if axial, i.e., 0°, layers were used. Instead of inputting slightly different values for the moduli, Roy specifies a minimum fiber orientation of 0.001°. Output from the program consisted of stresses and strains in the cylindrical coordinate system and the results from a failure analysis using the Tsai-Wu criterion.[12] The failure analysis was based on degraded properties where the degradation factor is a prescribed quantity. Roy typically uses a value of 0.3. Initially, the program was entirely interactive, which required the stacking sequence to be typed in during every execution. For the large number of layers dealt with in the present study this became very cumbersome. Consequently, the program was modified to specify the stacking sequence in a data file. Additional modifications included converting from single precision to double precision and increasing the maximum number of layers from 25 to 64.

The third program acquired, CYLAN, was based on using a Vlasov-Ambartsumyan[13] type laminated shell theory for calculating ply-level stresses and deformations in a laminated cylinder. Although this is essentially a two-dimensional theory, the program includes the

effects of through-the-thickness normal strains (see Whitney[14]). This theory is based on Love's[15] first approximation in which transverse shear and normal strains are neglected, and terms of the order h/R are negligible compared to unity. A modification to this theory based on Love's second approximation takes into account the presence of transverse normal strains, which are assumed to be independent of the radial coordinate. Analogous to classical lamination theory (CLT) for laminated plates, the problem is formulated in terms of the in-plane force and moment resultants, and the solution is in terms of the midplane strains and curvatures. The Vlasov-Ambartsumyan theory is valid for analyzing thin shells, i.e., R, $L \gg h$, constructed of orthotropic layers, and having small displacements, i.e., $|u|$, $|v|$, $|w| \leq h$. The applied external loads in the program consist of internal or external pressure, axial stress, torsional shear stress, and a uniform temperature change. The program calculates average quantities for the stresses and strains in each layer, and strength predictions are based on Tsai's quadratic interaction criterion.[16]

A new linear-elastic thick laminated cylinder analysis code was developed during this study that incorporated various aspects of the acquired codes and also accounted for some of their shortcomings. The solution procedure in the program is based on Hyer's[10] elasticity formulation, with two noteworthy exceptions. First, the program contains the exact solution for isotropic and transversely isotropic layers, i.e., the solution to the governing differential equation for the case of repeated roots equal to 1.0. This eliminated the numerical difficulty of division by zero that exists in Hyer's and Roy's codes. Second, in addition to axisymmetric thermal and mechanical loading, the program can determine the hygroscopic response of a laminated cylinder. The mechanical loading consists of uniform internal and external lateral pressure, axial force, torque, and hydrostatic pressure. The number of stress calculation points in each layer is a specified variable, and hybrid cylinders can be analyzed. Also, the program performs a first-ply failure analysis based on Hashin's[17] criterion and the Tsai-Wu criterion.[12]

1.1.2 Stress Analysis Results

The four composite cylinder stress analysis programs described in Sect. 1.1.1 were used to analyze three different cylinder configurations. Cylinder C6-1 had a 2:1 hoop to axial ply ratio, C6-2 had a 3:1 ratio, and C6-3 had a 1:1 ratio (see Sect. 2.2 for a detailed description of these cylinders). The results obtained from the different programs were compared to each other, compared with laminated shell theory (LST) results when a layered analysis was performed, and compared with results from the finite element method (FEM) when equivalent smeared properties were used. For the layered analysis, where the layers consisted of IM6 graphite fibers, ERL-2258 matrix, and a 67% fiber volume fraction, the following material properties were used:

$$E_1 = 22.63 \text{ MSI} \qquad \nu_{12} = 0.3117 \qquad G_{12} = 0.8571 \text{ MSI}$$
$$E_2 = 1.489 \text{ MSI} \qquad \nu_{13} = 0.3117 \qquad G_{13} = 0.8571 \text{ MSI}$$
$$E_3 = 1.489 \text{ MSI} \qquad \nu_{23} = 0.3781 \qquad G_{23} = 0.5400 \text{ MSI}$$

The analyses utilized the cylinder geometries described in Table 1.1.2-1. In the as-fabricated condition, all three cylinders had 74 layers (see Sect. 2.2). However, the model cylinders treated in the analyses had 38, 29, and 56 layers, respectively, for C6-1, C6-2, and C6-3, where adjacent plies in the repeating pattern having the same fiber orientation were modeled as a single layer.

Table 1.1.2-1. Model cylinder geometries

Cylinder	Inner radius (in.)	Outer radius (in.)	Thickness (in.)	Ply thickness. (in.)
C6-1	2.6590	3.1540	0.495	0.006689
C6-2	2.6575	3.1465	0.489	0.006608
C6-3	2.6585	3.1775	0.519	0.007014

1.1.2.1 Radial displacement

The distribution of the radial displacement, w, through the thickness for cylinder C6-1 is plotted in Fig. 1.1.2.1-1 for an applied unit pressure of 1.0 ksi. The results are shown only for the CCAP, ELCYL, and CYLIN programs because the fourth program, CYLAN, is a two-dimensional analysis and cannot predict radial displacements and stresses. The same plots are shown in Figures 1.1.2.1-2 and 1.1.2.1-3 for cylinders C6-2 and C6-3, respectively. The results indicate an excellent agreement between the CCAP program and the ELCYL program (the two curves superimpose in the plots). The CYLIN program, which is based on a slightly different formulation, predicts a larger radial displacement at the outer radius and a smaller radial displacement at the inner radius than the other two analyses. It is not clear from the details of the formulation why this behavior is demonstrated in the results. In any case, all three programs predict slightly larger radial deflections at the outer radius compared to the inner radius (except for cylinder C6-2). Also, Figures 1.1.2.1-1 through 1.1.2.1-3 clearly show the 3:1 cylinder (C6-2) to have the least amount of radial deflection and the 1:1 cylinder (C6-3) to have the largest radial deflection. The magnitudes of the radial displacement at the inner and outer radii in the three cylinders are compared in Table 1.1.2.1-1 for the three different programs. The results from the smeared property analyses are also given and are seen to be in close agreement with the layered analyses.

A finite element analyses was performed for cylinder C6-1, and the results for the radial displacement are compared to CCAP's elasticity solution in Figure 1.1.2.1-4. The agreement between the two solutions is excellent, with a nearly identical distribution across the cylinder wall. The magnitudes of the FEM prediction for the radial displacements at the midbay (i.e., cylinder midlength) inner and outer radii are given in Table 1.1.2.1-1 and are in excellent agreement with the CCAP predictions using smeared properties. Details of the finite element modeling are described in Sect. 1.3.

Cylinder C6−1
Radial Displacement
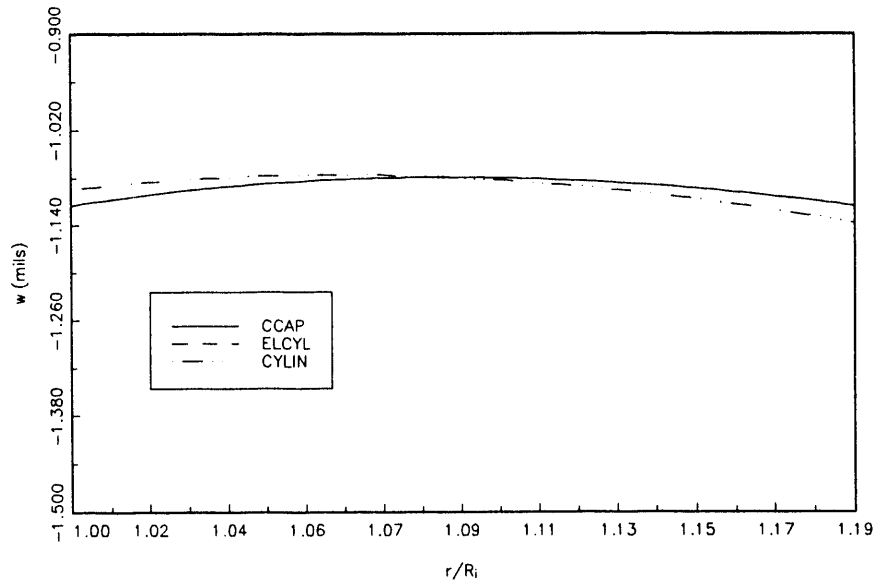
Fig. 1.1.2.1-1. Radial displacement for cylinder C6-1.

Cylinder C6−2
Radial Displacement
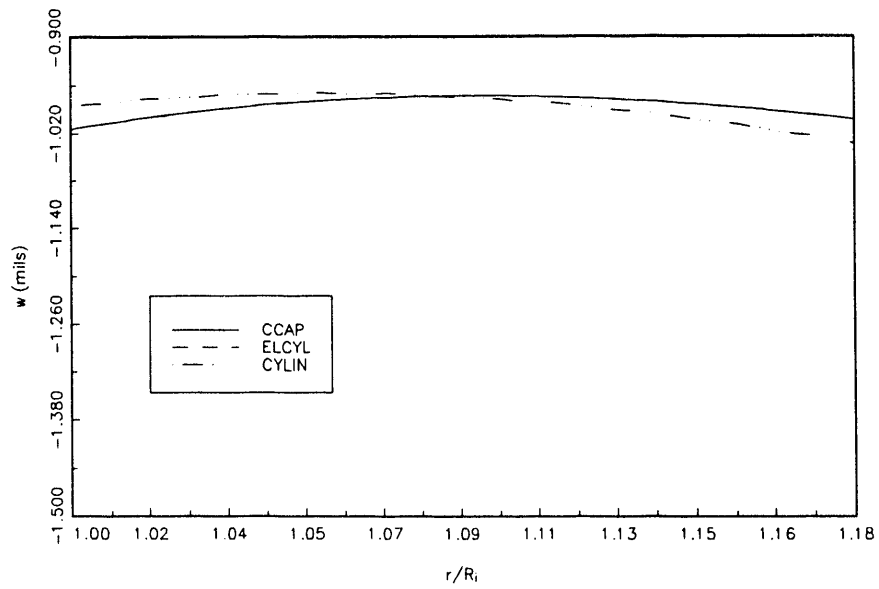
Fig. 1.1.2.1-2. Radial displacement for cylinder C6-2.

Cylinder C6−3
Radial Displacement
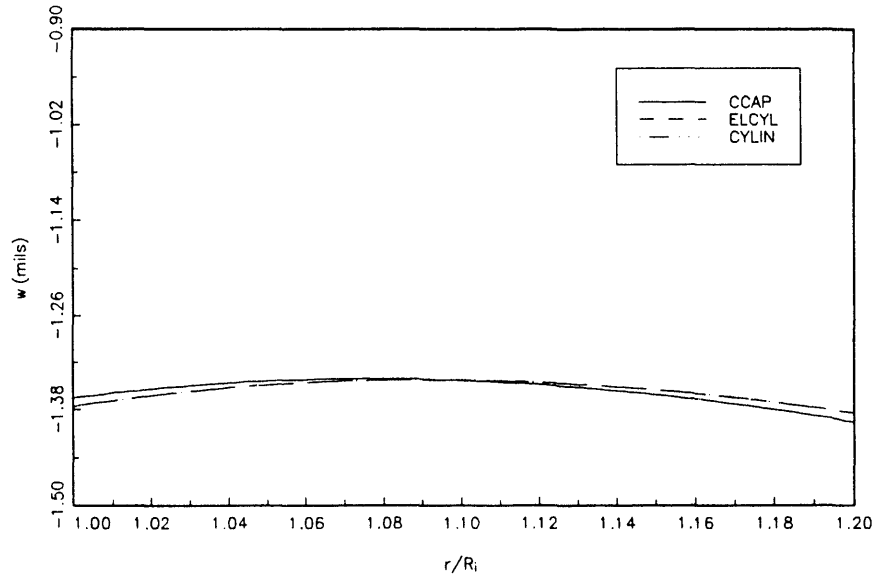
Fig. 1.1.2.1-3. Radial displacement for cylinder C6-3.

Cylinder C6−1
Radial Displacement
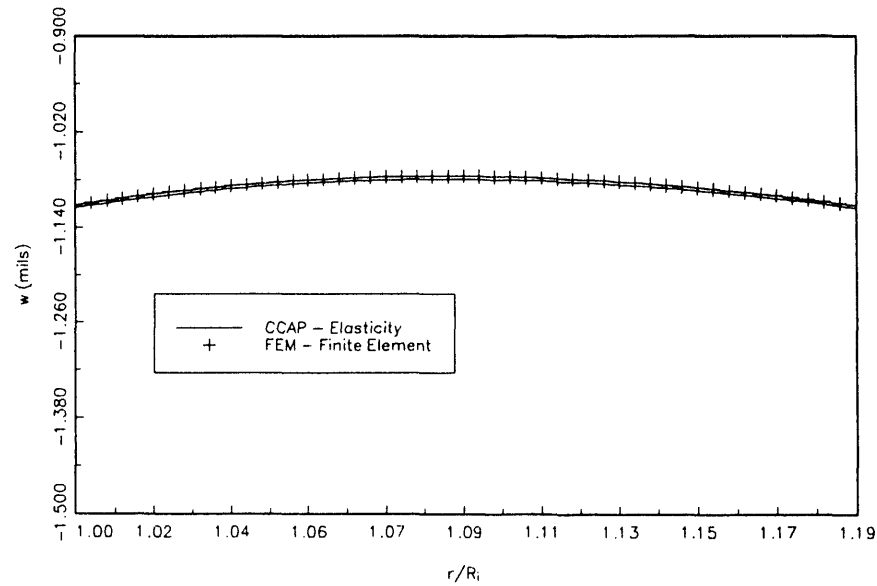
Fig. 1.1.2.1-4. CCAP and FEM results for the radial displacement in cylinder C6-1.

Table 1.1.2.1-1. Radial displacement at the inner and outer radii

	Layered properties					
Program	Cylinder C6-1		Cylinder C6-2		Cylinder C6-3	
	w_i [a] (mils)	w_o [b] (mils)	w_i (mils)	w_o (mils)	w_i (mils)	w_o (mils)
CCAP	-1.1149	-1.1157	-1.0145	-1.0029	-1.3761	-1.3841
ELCYL	-1.1150	-1.1156	-1.0145	-1.0028	-1.3762	-1.3840
CYLIN	-1.0942	-1.1376	-0.9852	-1.0339	-1.3650	-1.3958

	Smeared properties					
Program	Cylinder C6-1		Cylinder C6-2		Cylinder C6-3	
	w_i [a] (mils)	w_o [b] (mils)	w_i (mils)	w_o (mils)	w_i (mils)	w_o (mils)
CCAP	-1.1155	-1.1163	-1.0149	-1.0032	-1.3774	-1.3851
ELCYL	-1.1155	-1.1163	-1.0149	-1.0032	-1.3774	-1.3851
CYLIN	-1.1276	-1.0599	-1.0183	-0.9561	-1.4002	-1.3165
FEM	-1.1113	-1.1121	-1.0115	-0.9997	-1.3767	-1.3846

[a] Inner radius
[b] Outer radius

Note: Applied pressure = 1.0 ksi

1.1.2.2 Strains

For the cylinder constructions considered in this investigation, i.e., only axial and circumferential plies, the analytical formulations described in Sect. 1.1.1 predict vanishing shear strains. The normal components of strain (axial, hoop, and radial) have a distribution through the cylinder wall of C6-1 as predicted by CCAP, ELCYL, and CYLIN as shown in Figures 1.1.2.2-1, 1.1.2.2-2, and 1.1.2.2-3, respectively. Also presented in Figure 1.1.2.2-1 is a comparison of the CCAP results with the finite element results at the cylinder midbay. These three figures show that the results from the three programs and the finite element method are in excellent agreement with each other and that the normal strains are uniform through the thickness, i.e., continuous across the interfaces. The distribution of the axial strain is constant across the wall thickness, whereas the radial and hoop strains have gradients. The radial component of strain has an almost linear distribution with steps resulting from the layered analysis and varies from being tensile at the inner radius to compressive at the outer radius. The FEM models the laminated cylinder as a single homogeneous layer having equivalent smeared orthotropic properties. The slight disagreement between the elasticity solution and the FEM results for the radial strain near the inner and outer radii is a result of the numerical extrapolation from the Gauss points to the boundary used in the finite element method. For the C6-1 cylinder the ratio of hoop to axial plies is 2:1 and the analytic results predict approximately a 1:1 ratio of hoop to axial strain over the exterior half of the cylinder wall. Over the interior half, the hoop strains become increasingly larger than the axial strains (up to 15% larger at the inner radius). In Figure 1.1.2.2-4 the distribution of the axial and hoop strains in C6-1 from CCAP are compared with the two-dimensional predictions of CYLAN. The results indicate that assuming a two-dimensional stress state under predicts the hoop strains by 7.9% at the inner radius and over predicts the axial strain by 7.6% compared to a three-dimensional analysis. Also, the ratio of the hoop to axial strain exhibits a different behavior in the two-dimensional analysis than in the three-dimensional analysis. For the two-dimensional stress state the hoop to axial strain ratio is approximately equal to 1.0 at the inner radius. However, the ratio of hoop to axial strain decreases to a value of 0.84 at the outer radius.

Similar observations were seen in the strain distributions for cylinders C6-2 and C6-3 but with different results for the ratio of hoop to axial strain. Figures 1.1.2.2-5 to 1.1.2.2-8 show the analytic predictions for the normal strains in cylinder C6-2, and the results for cylinder C6-3 are presented in Figures 1.1.2.2-9 through 1.1.2.2-12. The axial strains in cylinder C6-2 are larger than the hoop strains across the entire wall thickness. The ratio of the hoop to axial strain for this 3:1 hoop to axial ply ratio cylinder is equal to 0.82 at the inner radius. For the 1:1 ply ratio cylinder, i.e., C6-3, the ratio of hoop to axial strain at the inner radius is equal to 2.12. The magnitudes of the normal strain components at the inner and outer radii are given in Tables 1.1.2.2-1, 1.1.2.2-2 and 1.1.2.2-3 for cylinders C6-1, C6-2, and C6-3, respectively. The results from using smeared properties are also given and indicate accurate strains can be predicted by modeling a laminated cylinder as a single layer having equivalent smeared properties. The largest hoop strain is seen in the 1:1 cylinder, whereas the largest axial strain is in the 3:1 cylinder. Conversely, the 3:1 cylinder has the smallest hoop strain, and the 1:1 cylinder has the smallest axial strain. The percentage decrease in the hoop strain obtained by increasing the number of hoop plies from a 1:1 ratio to a 3:1 ratio is equal to 26%. The gradient of the radial strain across the cylinder wall is seen to be comparable for all three cylinder constructions.

Cylinder C6−1
Normal Strains − CCAP & FEM
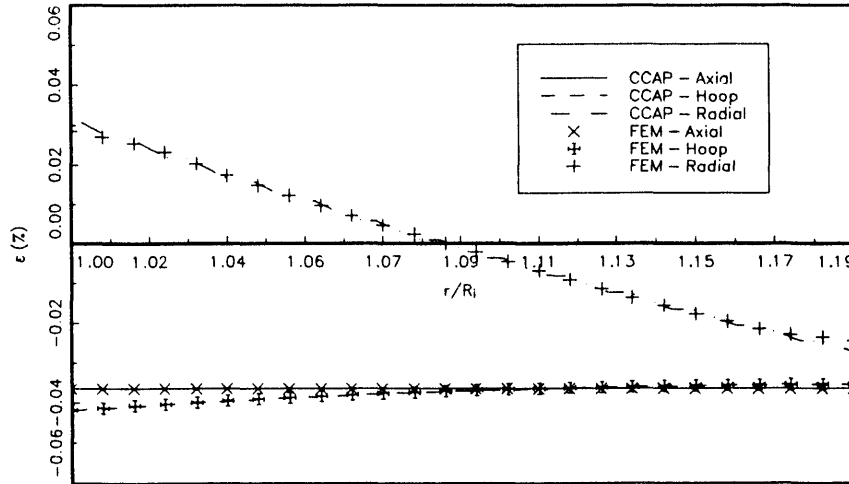
Fig. 1.1.2.2-1. Normal strains in cylinder C6-1 from CCAP program and FEM.

Cylinder C6−1
Normal Strains − ELCYL
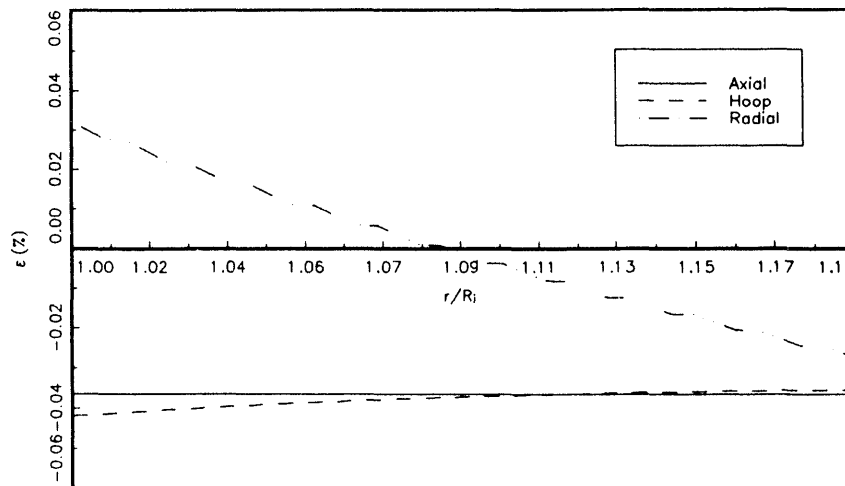
Fig. 1.1.2.2-2. Normal strains in cylinder C6-1 from ELCYL program.

Cylinder C6−1
Normal Strains − CYLIN
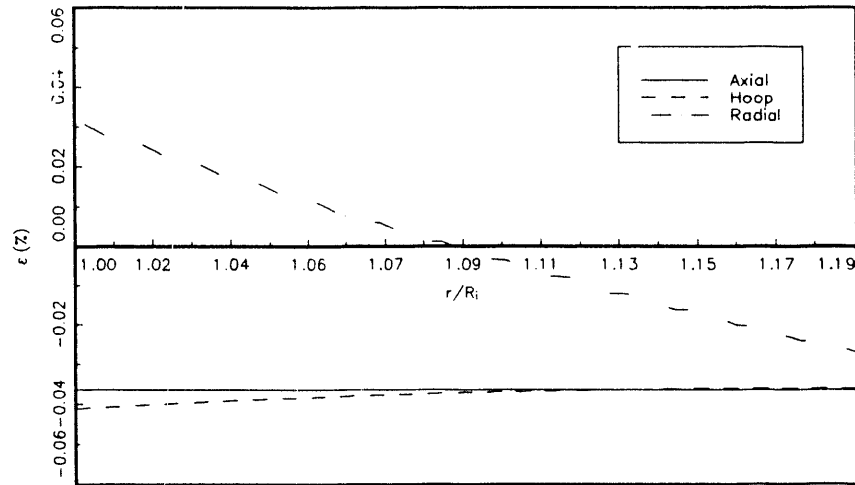
Fig. 1.1.2.2-3. Normal strains in cylinder C6-1 from CYLIN program.

Cylinder C6−1
Normal Strains
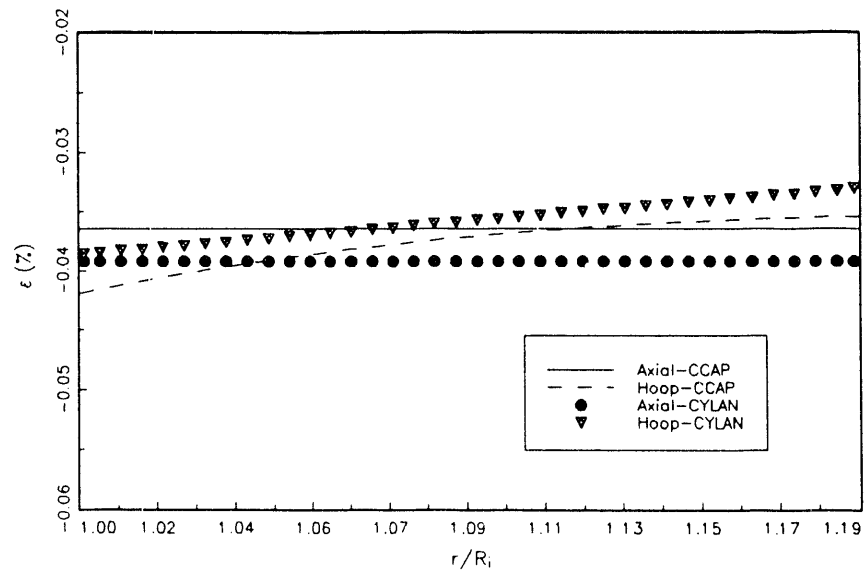
Fig. 1.1.2.2-4. Axial and hoop strains in cylinder C6-1 from CCAP and CYLAN programs.

Cylinder C6—2
Normal Strains — CCAP
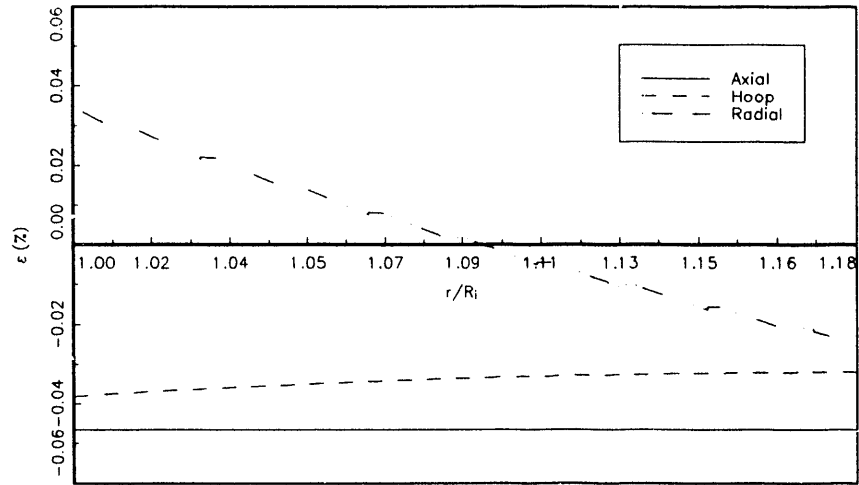
Fig. 1.1.2.2-5. Normal strains in cylinder C6-2 from CCAP program.

Cylinder C6—2
Normal Strains — ELCYL
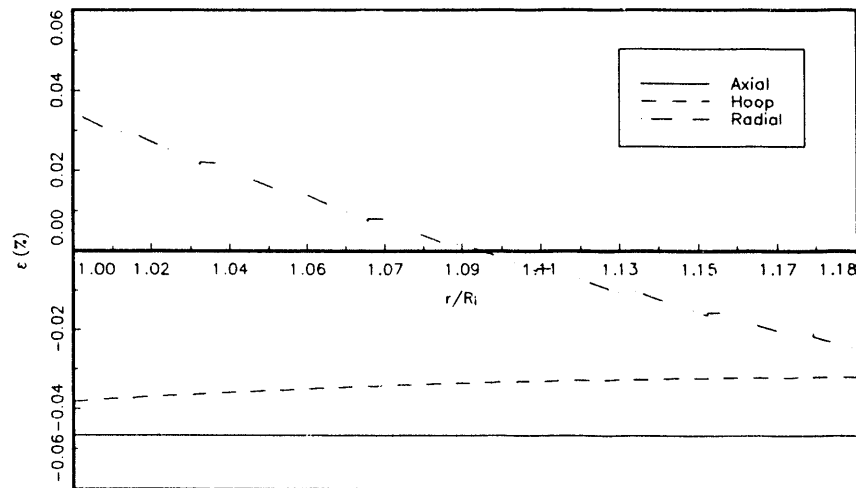
Fig. 1.1.2.2-6. Normal strains in cylinder C6-2 from ELCYL program.
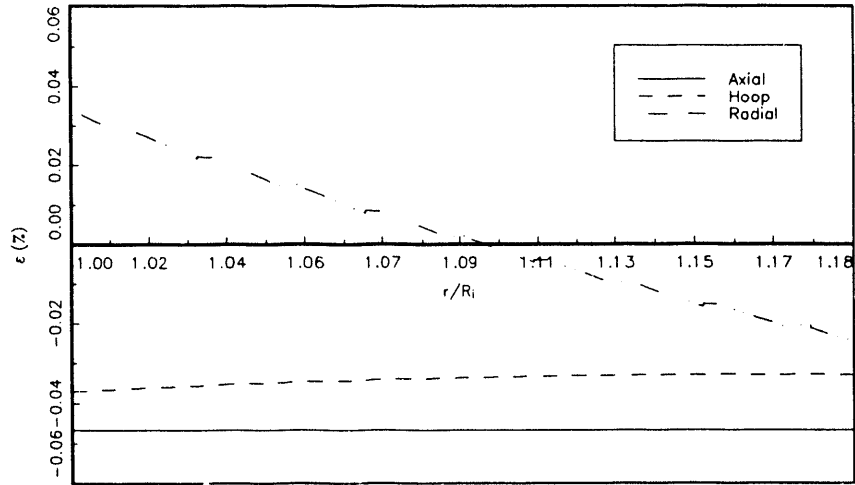
Fig. 1.1.2.2-7. Normal strains in cylinder C6-2 from CYLIN program.
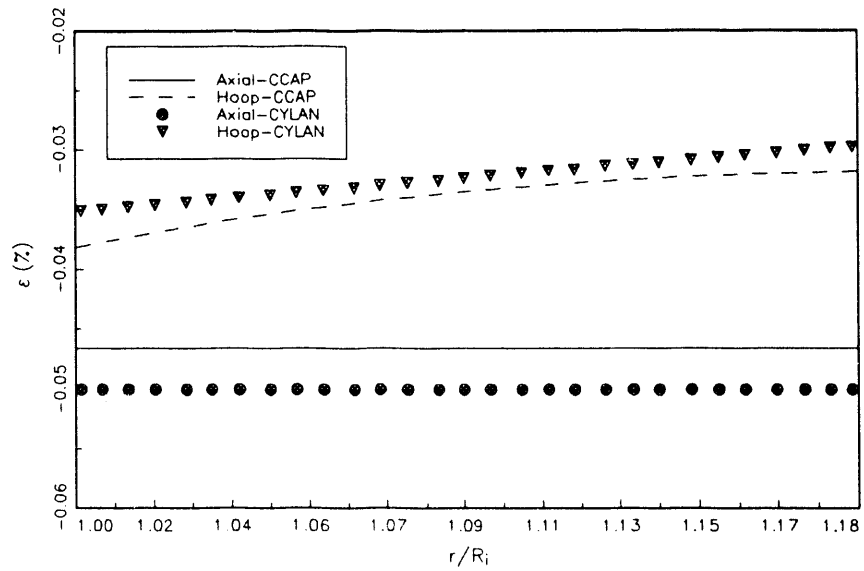
Fig. 1.1.2.2-8. Axial and hoop strains in cylinder C6-2 from CCAP and CYLAN programs.

Cylinder C6−3
Normal Strains − CCAP
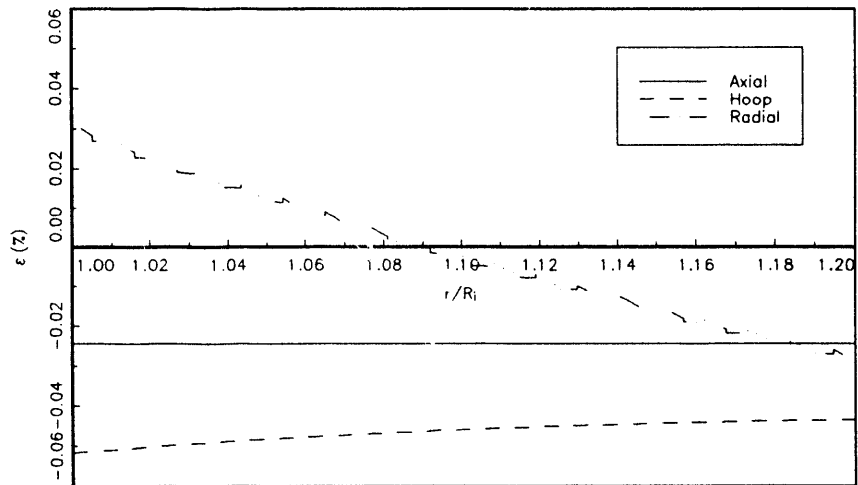
Fig. 1.1.2.2-9. Normal strains in cylinder C6-3 from CCAP program.

Cylinder C6−3
Normal Strains − ELCYL
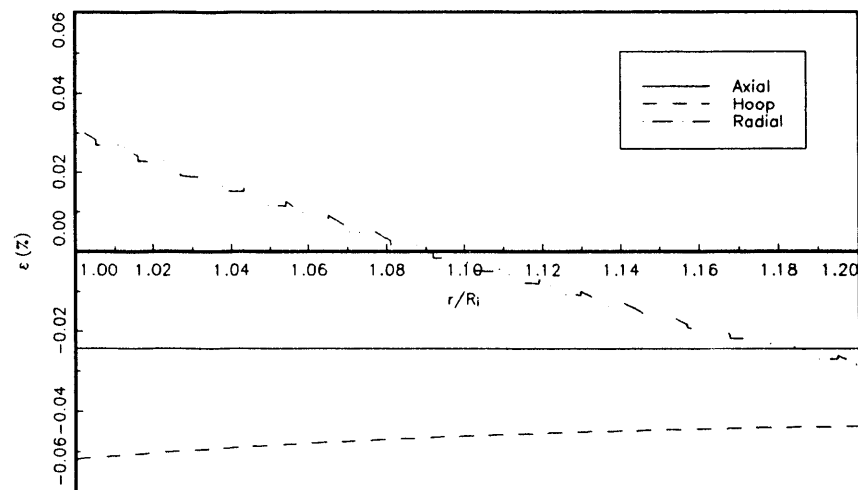
Fig. 1.1.2.2-10. Normal strains in cylinder C6-3 frcm ELCYL program.

Cylinder C6−3
Normal Strains − CYLIN
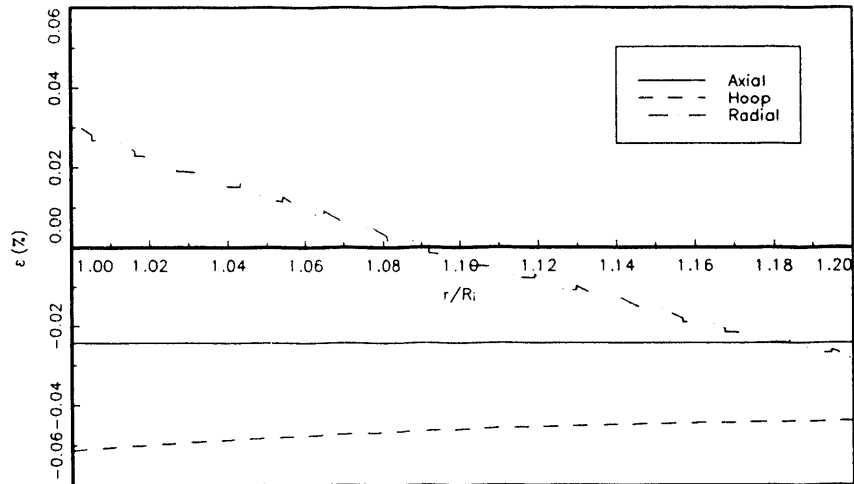
Fig. 1.1.2.2-11. Normal strains in cylinder C6-3 from CYLIN program.

Cylinder C6−3
Normal Strains
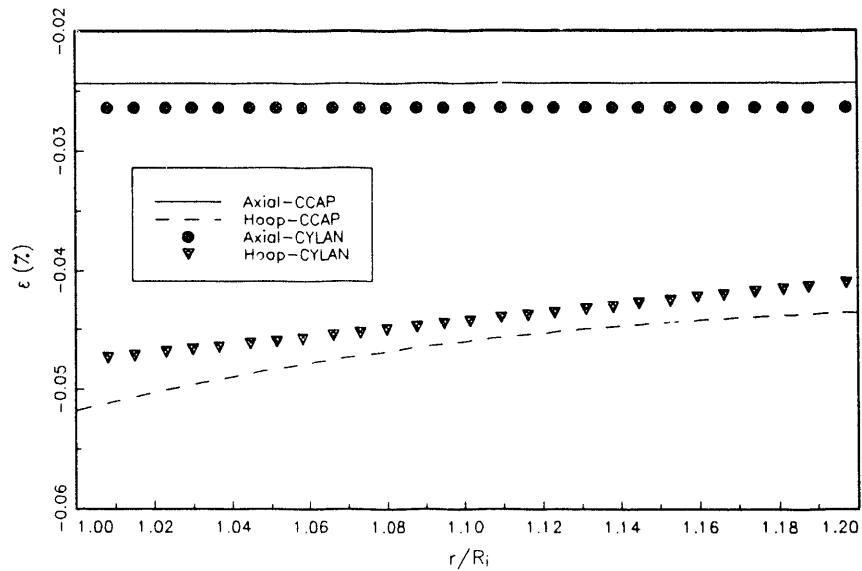
Fig. 1.1.2.2-12. Axial and hoop strains in cylinder C6-3 from CCAP and CYLAN programs.

Table 1.1.2.2-1. Cylinder C6-1 strains at the inner and outer radii

	Layered properties					
	Axial (%)		Hoop (%)		Radial (%)	
Program	$\epsilon_x^{i\ a}$	$\epsilon_x^{o\ b}$	ϵ_y^i	ϵ_y^o	ϵ_r^i	ϵ_r^o
CCAP	-0.036435	-0.036435	-0.041931	-0.035373	+0.032226	-0.027346
ELCYL	-0.036435	-0.036435	-0.041932	-0.035371	+0.032227	-0.027302
CYLIN	-0.036449	-0.036449	-0.041153	-0.036069	+0.031895	-0.027040
CYLAN	-0.0392	-0.0392	-0.0386	-0.0330	-	-
LST	-0.039167	-0.039167	-0.035835	-0.035835	-	-

	Smeared properties					
	Axial (%)		Hoop (%)		Radial (%)	
Program	ϵ_x^i	ϵ_x^o	ϵ_y^i	ϵ_y^o	ϵ_r^i	ϵ_r^o
CCAP	-0.036432	-0.036432	-0.041952	-0.035794	+0.032157	-0.027427
ELCYL	-0.036432	-0.036432	-0.041952	-0.035394	+0.032157	-0.027427
CYLIN	-0.038798	-0.038798	-0.042407	-0.033605	+0.018456	+0.009653
CYLAN	-0.0392	-0.0392	-0.0369	-0.0347	-	-
FEM	-0.036454	-0.036472	-0.041783	-0.035256	-0.028527	-0.024432

[a] Inner radius
[b] Outer radius

Note: Applied pressure = 1.0 ksi

Table 1.1.2.2-2. Cylinder C6-2 strains at the inner and outer radii

Program	Layered properties					
	Axial (%)		Hoop (%)		Radial (%)	
	$\epsilon_x^{i\ a}$	$\epsilon_x^{o\ b}$	ϵ_y^i	ϵ_y^o	ϵ_r^i	ϵ_r^o
CCAP	-0.046601	-0.046601	-0.038173	-0.031874	+0.034536	-0.024925
ELCYL	-0.046601	-0.046601	-0.038175	-0.031871	+0.034637	-0.024881
CYLIN	-0.046630	-0.046630	-0.037074	-0.032858	+0.034072	-0.024488
CYLAN	-0.0500	-0.0500	-0.0351	-0.0298	-	-
LST	-0.0500	-0.0500	-0.032392	-0.032392	-	-

Program	Smeared properties					
	Axial (%)		Hoop (%)		Radial (%)	
	ϵ_x^i	ϵ_x^o	ϵ_y^i	ϵ_y^o	ϵ_r^i	ϵ_r^o
CCAP	-0.046597	-0.046597	-0.038189	-0.031884	+0.034637	-0.024768
ELCYL	-0.046597	-0.046597	-0.038189	-0.031884	+0.034637	-0.024768
CYLIN	-0.049579	-0.049579	-0.038318	-0.030387	+0.017013	+0.009082
CYLAN	-0.0500	-0.0500	-0.0334	-0.0314	-	-
FEM	-0.046200	-0.047278	-0.038064	-0.031781	+0.027442	-0.019628

^{a} Inner radius
^{b} Outer radius

Note: Applied pressure = 1.0 ksi

Table 1.1.2.2-3. Cylinder C6-3 strains at the inner and outer radii

Layered properties

Program	Axial (%)		Hoop (%)		Radial (%)	
	ϵ_x^i [a]	ϵ_x^o [b]	ϵ_y^i	ϵ_y^o	ϵ_r^i	ϵ_r^o
CCAP	-0.024388	-0.024388	-0.051762	-0.043669	+0.031818	-0.028469
ELCYL	-0.024388	-0.024388	-0.051763	-0.043557	+0.031816	-0.028425
CYLIN	-0.024393	-0.024393	-0.051346	-0.043929	+0.031637	-0.028307
CYLAN	-0.0264	-0.0264	-0.0476	-0.0411	-	-
LST	-0.026386	-0.026386	-0.044260	-0.044260	-	-

Smeared properties

Program	Axial (%)		Hoop (%)		Radial (%)	
	ϵ_x^i	ϵ_x^o	ϵ_y^i	ϵ_y^o	ϵ_r^i	ϵ_r^o
CCAP	-0.024390	-0.024390	-0.051813	-0.043591	+0.031235	-0.028888
ELCYL	-0.024390	-0.024390	-0.051813	-0.043591	+0.031235	-0.028888
CYLIN	-0.026054	-0.026054	-0.052669	-0.041433	+0.022235	+0.011000
CYLAN	-0.0264	-0.0264	-0.0457	-0.0428	-	-
FEM	-0.024056	-0.024177	-0.051761	-0.043577	+0.023723	-0.023937

[a] Inner radius
[b] Outer radius

Note: Applied pressure = 1.0 ksi

1.1.2.3 Stresses

In contrast to the strains, which are continuous functions across the cylinder wall for a layered analysis, the hoop and axial stresses are discontinuous. However, continuity of the normal radial component of stress was ensured as part of the analytical development. The assumed state of stress and the axisymmetry considered in the analyses resulted in $\tau_{x\theta}$ being the only nonzero shear stress, but for the case of having only axial and hoop plies in the cylinder construction, $\tau_{x\theta}$ is zero. The distribution of the hoop and axial components of stress through the wall thickness was determined by using the four programs described in Sect. 1.1.1. A discussion of the results comparing the three cylinder configurations is presented below.

In Fig. 1.1.2.3-1 the hoop stress in C6-1 is plotted using the results from the CCAP and the CYLAN programs. The hoop stress has a maximum compressive value in the inner hoop ply of -9.7201 ksi for the CCAP program and -8.96 ksi for the CYLAN program with a unit hydrostatic pressure applied. Consequently, it is seen that the two-dimensional CYLAN analysis predicts a maximum hoop stress which is 7.8% less than the prediction from the three-dimensional analysis of CCAP. The results from the ELCYL and the CYLIN programs are shown in Figs. 1.1.2.3-2 and 1.1.2.3-3, respectively, and are in excellent agreement with the CCAP results. Similar results were obtained for cylinders C6-2 and C6-3 but with different maximum values for the hoop stress. The same plots as were generated for C6-1 are shown in Figs. 1.1.2.3-4 through 1.1.2.3-6 for C6-2 and in Figs. 1.1.2.3-7 through 1.1.2.3-9 for C6-3. The maximum hoop stress is seen to be -8.9119 ksi and -11.903 ksi for the C6-2 and C6-3 cylinders, respectively. These magnitudes correspond to an 8.3% decrease in the maximum hoop stress for the 3:1 lay-up and a 22.4% increase for the 1:1 lay-up as compared to the 2:1 cylinder configuration.

The axial stress profiles for the three cylinder constructions are illustrated in Figs. 1.1.2.3-10 through 1.1.2.3-12 for C6-1, Figs. 1.1.2.3-13 through 1.1.2.3-15 for C6-2, and Figs. 1.1.2.3-16 through 1.1.2.3-18 for C6-3. The results show that the axial stress is a maximum in the outermost axial ply of all three cylinders. These figures also show an excellent agreement between the results for CCAP, ELCYL, and CYLIN but with slightly larger compressive stresses in the axial plies predicted by CYLAN. Cylinder C6-2, which has the smallest percentage of axial plies, is seen to have the largest compressive axial stress; whereas cylinder C6-3, which has the largest percentage of axial plies, has the smallest axial stress. The axial stress in C6-2 is 25.9% larger than the axial stress in C6-1, and C6-3 has a 30% smaller axial stress than C6-1. For a unit applied pressure, the magnitudes of the maximum axial stress are reported in Table 1.1.2.3-1 along with the maximum hoop stresses. The ratio of the hoop to axial stress is 0.798, 1.095, and 1.298 for the 3:1, 2:1, and 1:1 hoop to axial ply ratio cylinders, respectively.

It was demonstrated in Sect. 1.1.2.2 that accurate predictions for the strains was possible by modeling the laminated cylinder as a single homogeneous layer having equivalent smeared properties. However, this is not the case for predicting stresses as seen in the smeared property results in Table 1.1.2.3-1. The single-layered composite cylinder analyses, which includes the FEM results, severely under predict the maximum hoop and axial stresses. It should be noted that the FEM results are in excellent agreement with the elasticity solution when smeared properties are used.
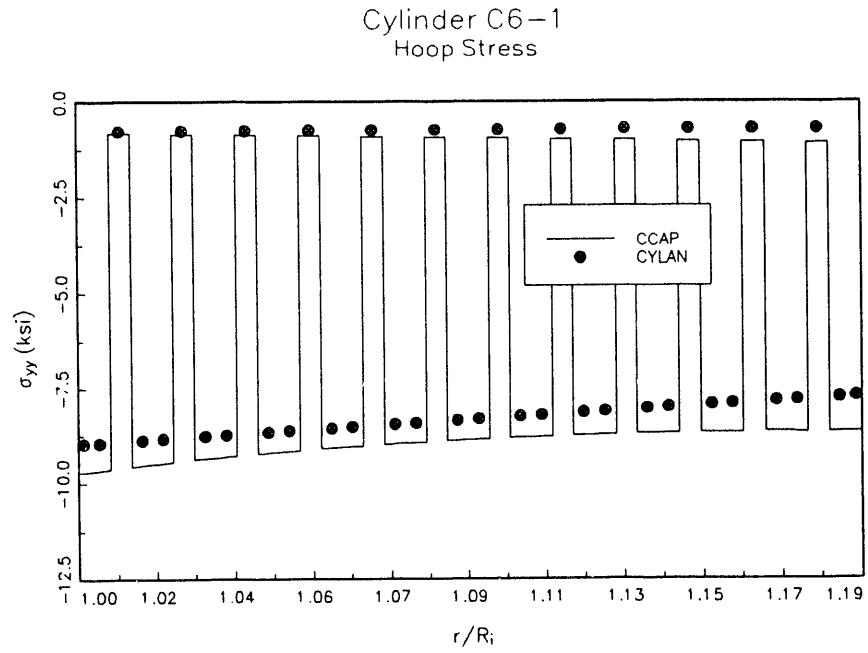
Fig. 1.1.2.3-1. Hoop stress in cylinder C6-1 from CCAP and CYLAN programs.
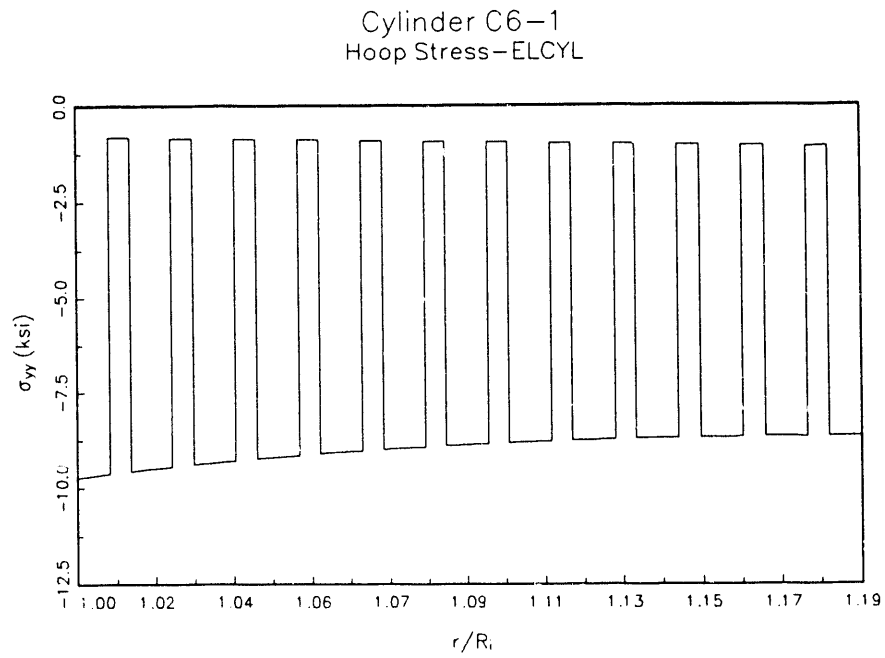
Fig. 1.1.2.3-2. Hoop stress in cylinder C6-1 from ELCYL program.

Cylinder C6–1
Hoop Stress–CYLIN
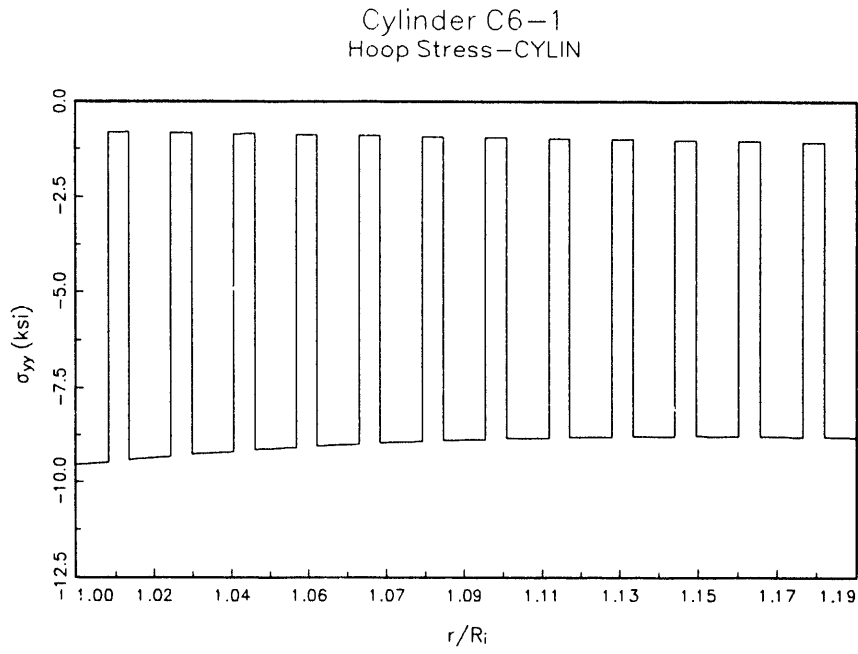
Fig. 1.1.2.3-3. Hoop stress in cylinder C6-1 from CYLIN program.

Cylinder C6–2
Hoop Stress
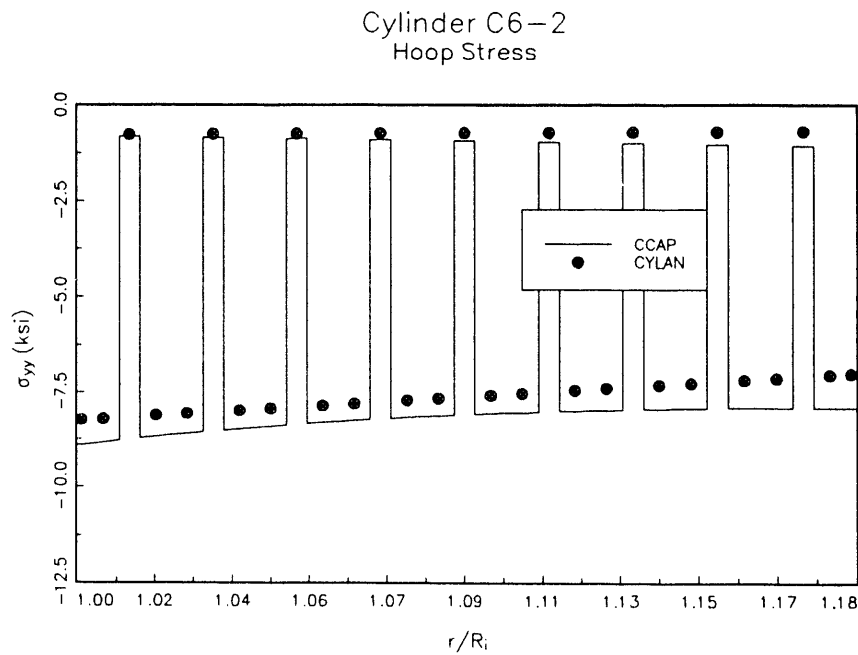
Fig. 1.1.2.3-4. Hoop stress in cylinder C6-2 from CCAP and CYLAN programs.

Cylinder C6—2
Hoop Stress—ELCYL
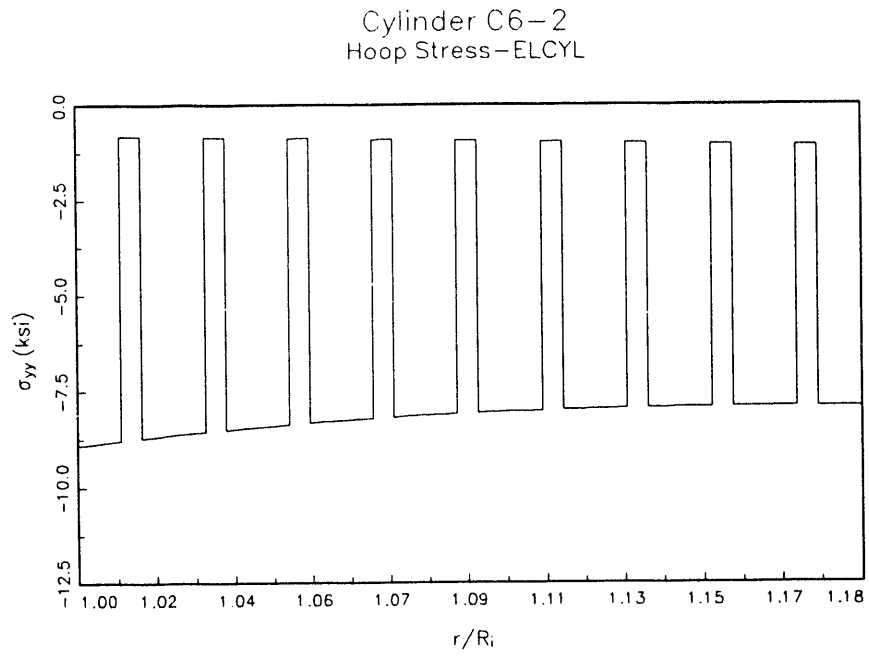
Fig. 1.1.2.3-5. Hoop stress in cylinder C6-2 from ELCYL program.

Cylinder C6—2
Hoop Stress—CYLIN
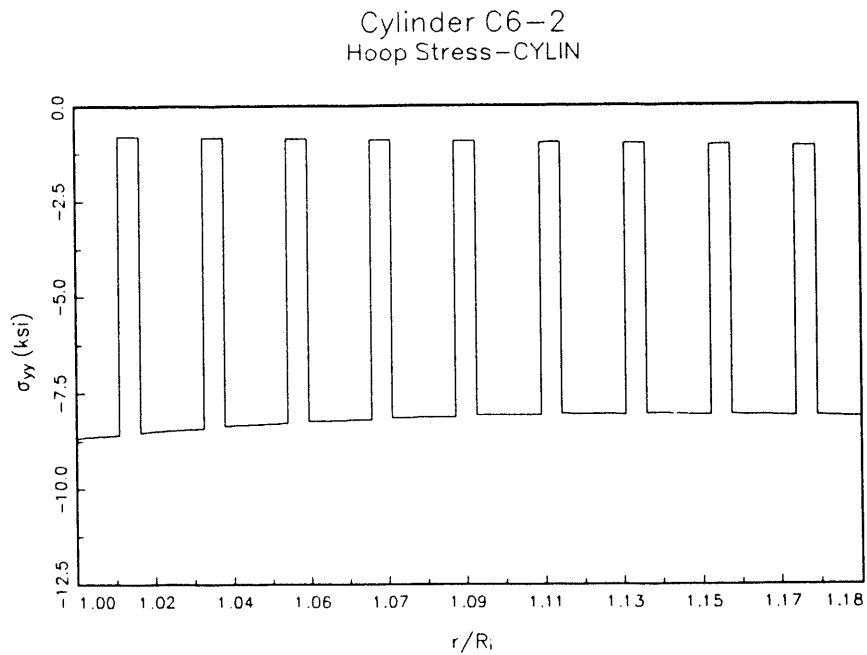
Fig. 1.1.2.3-6. Hoop stress in cylinder C6-2 from CYLIN program.
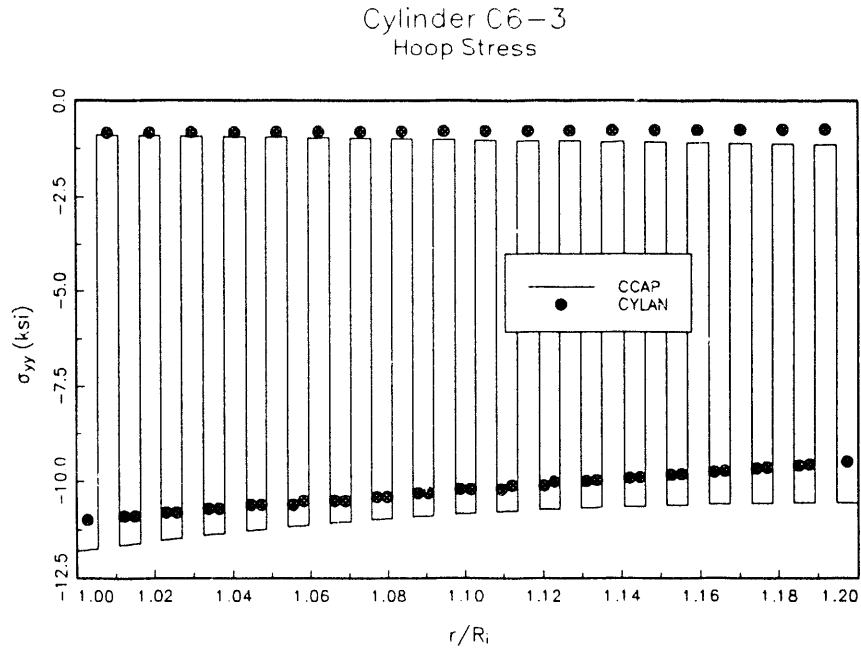
Fig. 1.1.2.3-7. Hoop stress in cylinder C6-3 from CCAP and CYLAN programs.
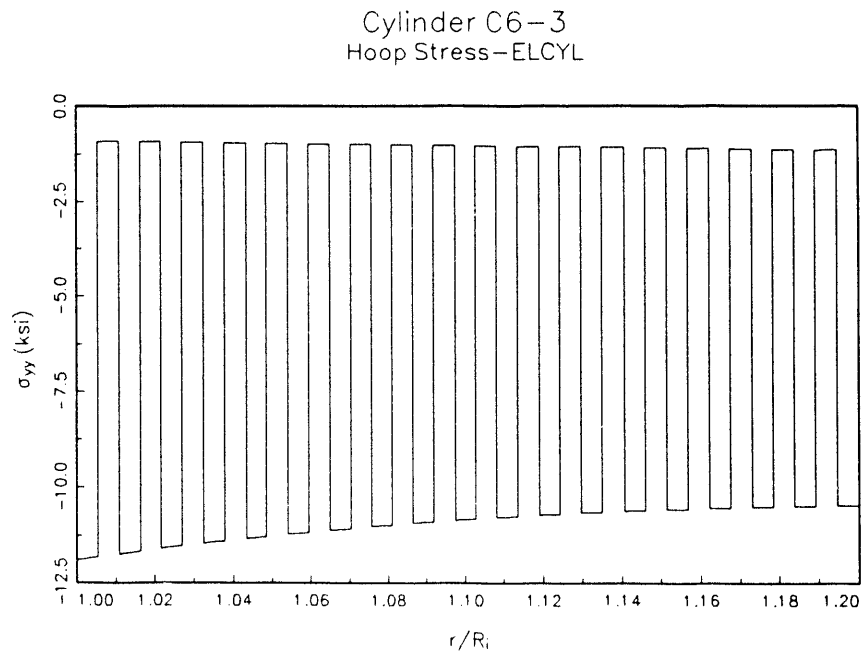
Fig. 1.1.2.3-8. Hoop stress in cylinder C6-3 from ELCYL program.

Cylinder C6−3
Hoop Stress−CYLIN
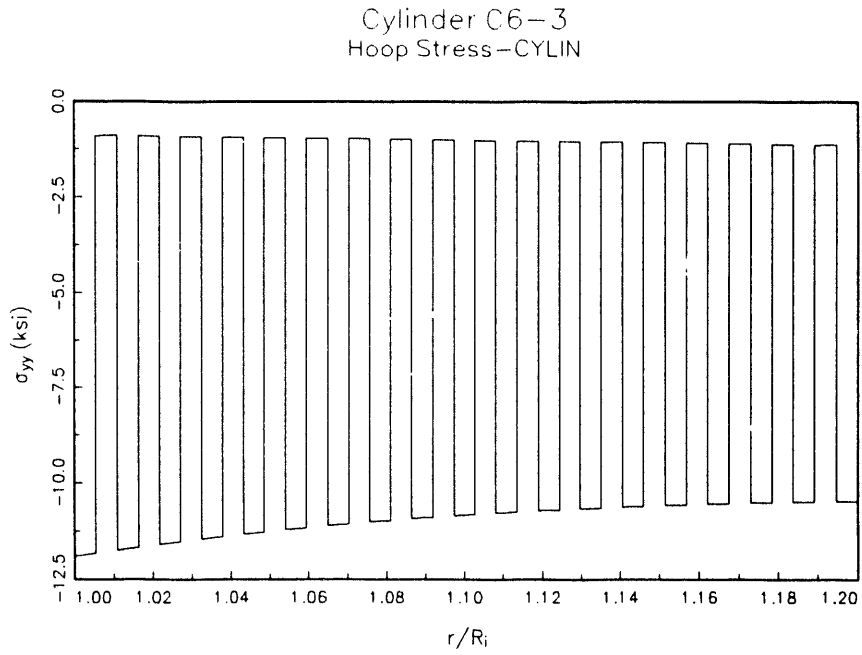
Fig. 1.1.2.3-9. Hoop stress in cylinder C6-3 from CYLIN program.

Cylinder C6−1
Axial Stress
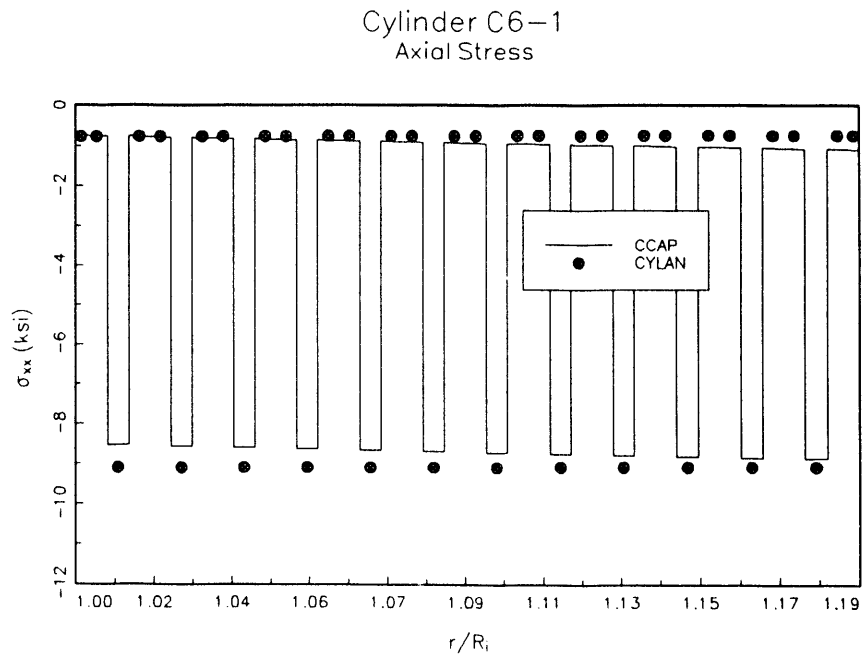
Fig. 1.1.2.3-10. Axial stress in cylinder C6-1 from CCAP and CYLAN programs.

Cylinder C6—1
Axial Stress—ELCYL
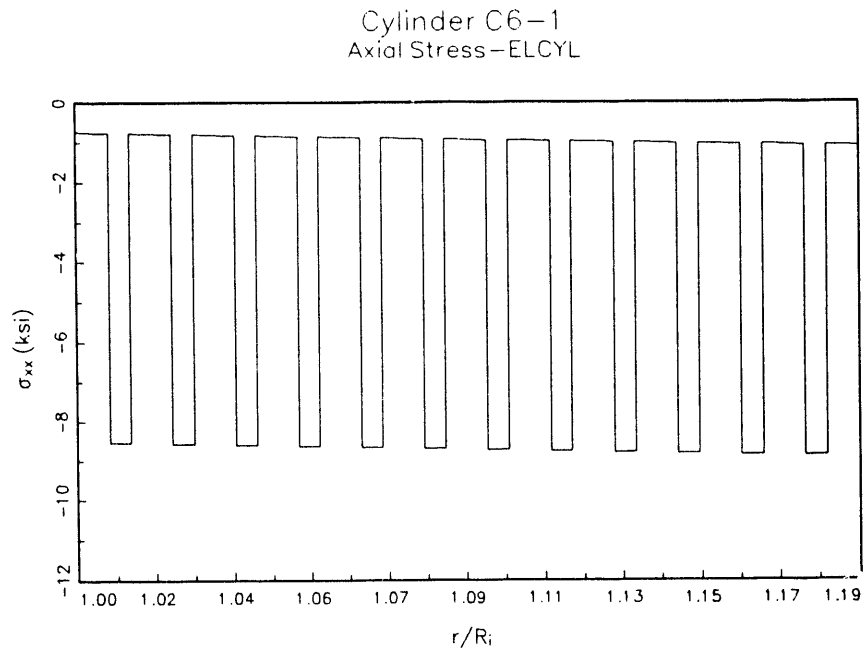
Fig. 1.1.2.3-11. Axial stress in cylinder C6-1 from ELCYL program.

Cylinder C6—1
Axial Stress—CYLIN
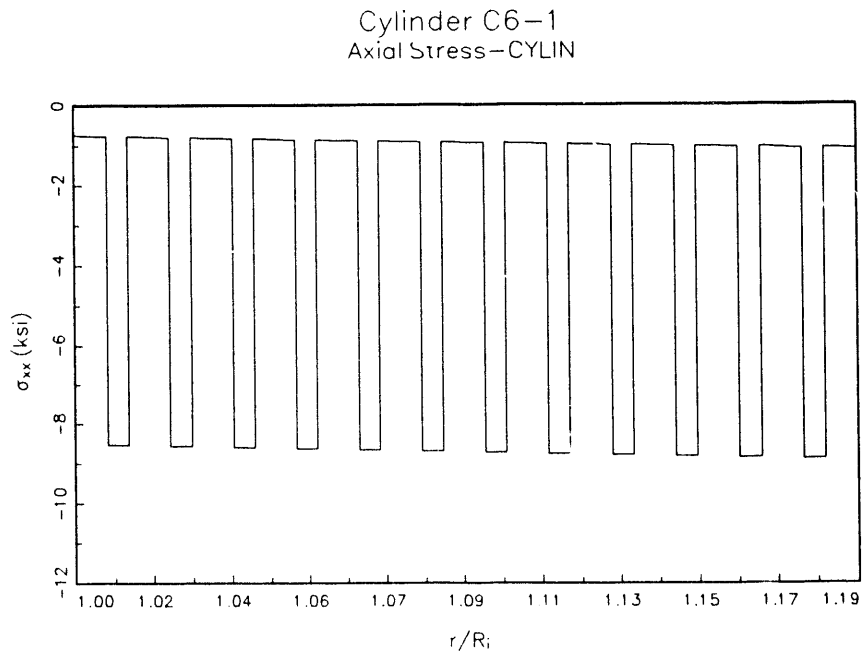
Fig. 1.1.2.3-12. Axial stress in cylinder C6-1 from CYLIN program.
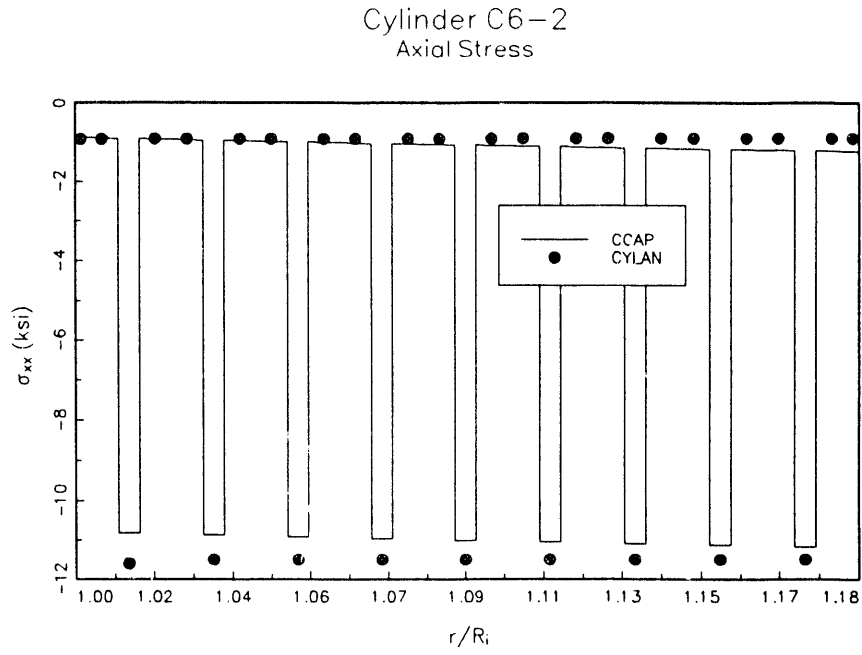
Fig. 1.1.2.3-13. Axial stress in cylinder C6-2 from CCAP and CYLAN programs.
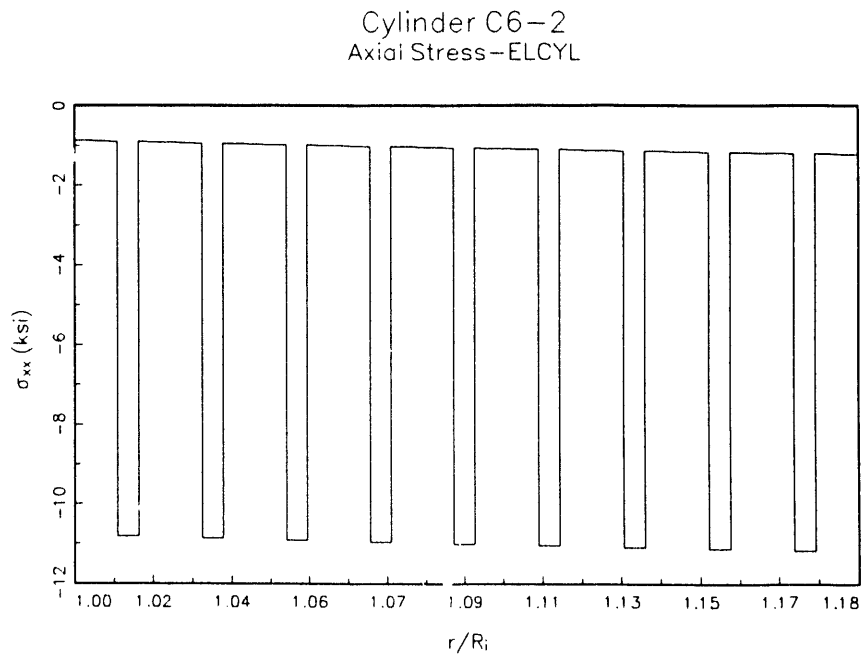
Fig. 1.1.2.3-14. Axial stress in cylinder C6-2 from ELCYL program.
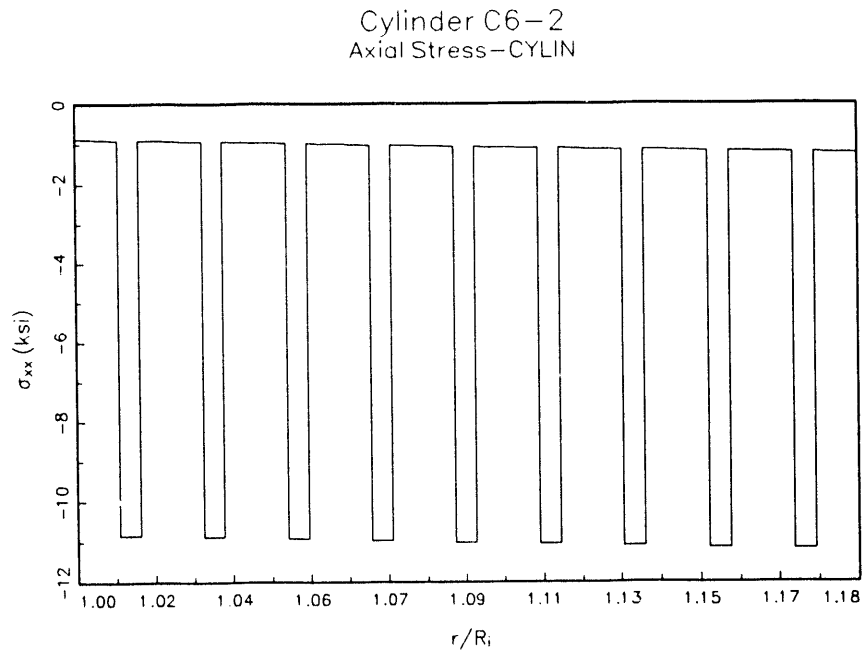
Fig. 1.1.2.3-15. Axial stress in cylinder C6-2 from CYLIN program.
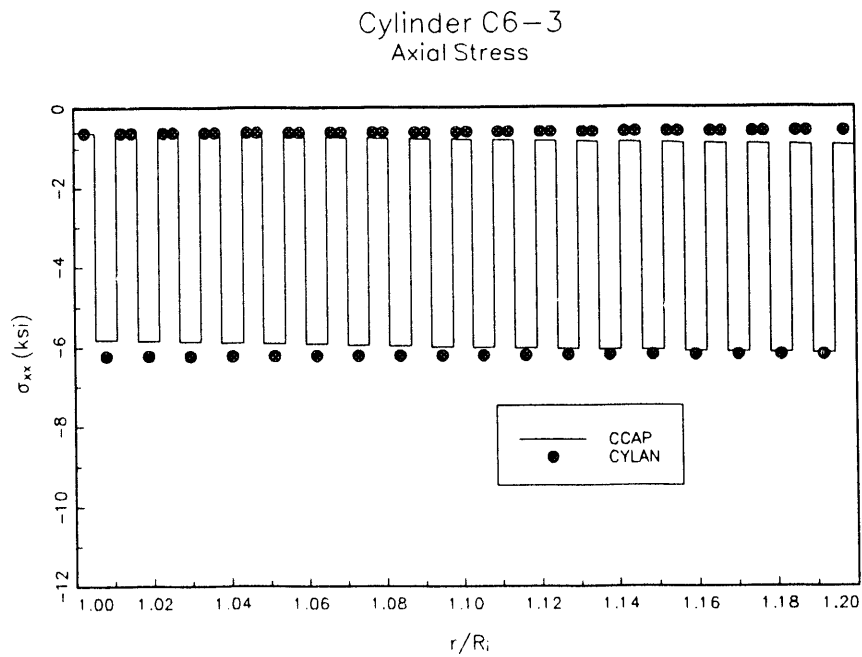
Fig. 1.1.2.3-16. Axial stress in cylinder C6-3 from CCAP and CYLAN programs.

Cylinder C6−3
Axial Stress−ELCYL
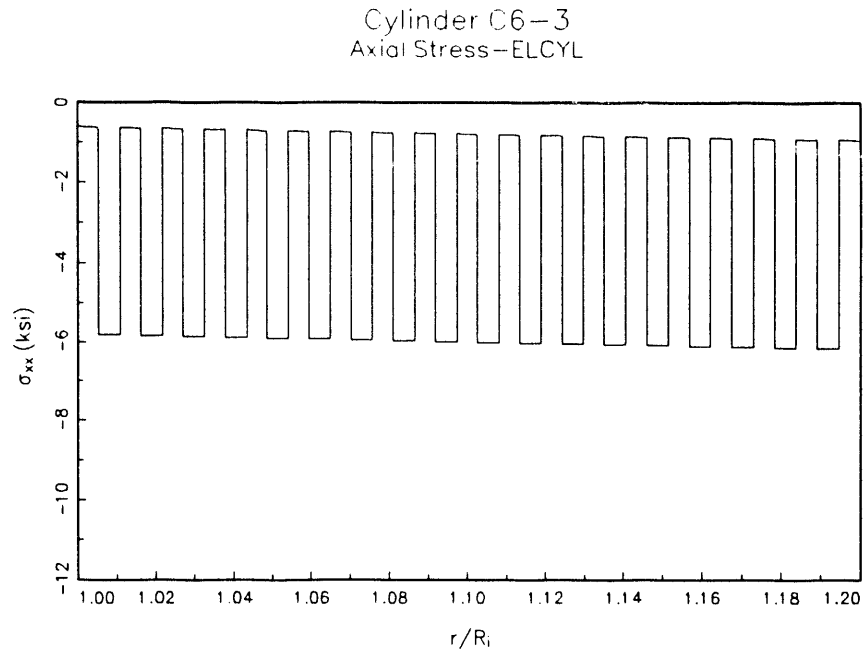
Fig. 1.1.2.3-17. Axial stress in cylinder C6-3 from ELCYL program.

Cylinder C6−3
Axial Stress−CYLIN
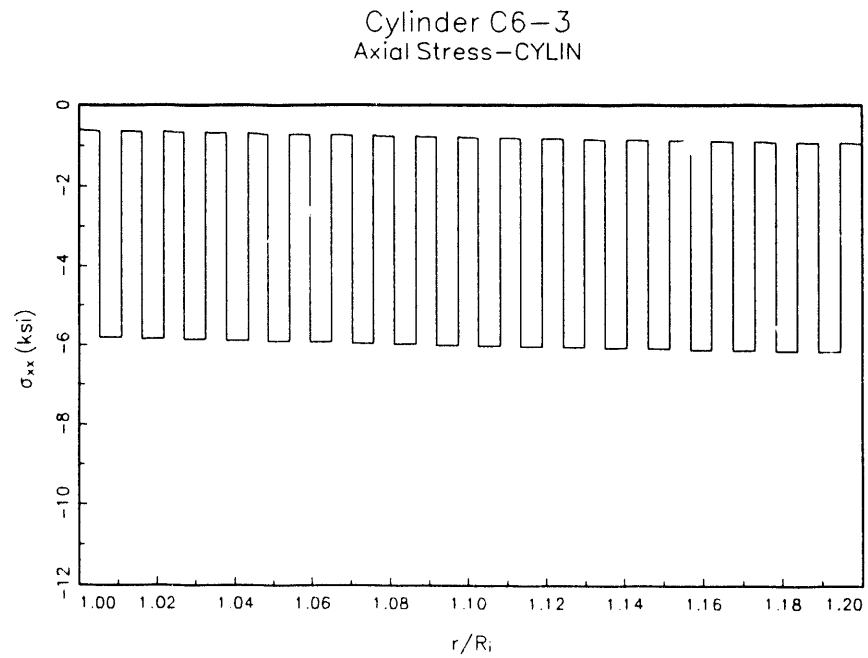
Fig. 1.1.2.3-18. Axial stress in cylinder C6-3 from CYLIN program.

Table 1.1.2.3-1. Maximum hoop and axial stresses

Program	Layered properties					
	Axial stress (ksi)			Hoop stress (ksi)		
	C6-1	C6-2	C6-3	C6-1	C6-2	C6-3
CCAP	-8.8748	-11.170	-6.1726	-9.7201	-8.9119	-11.903
ELCYL	-8.8748	-11.170	-6.1725	-9.7205	-8.9122	-11.903
CYLIN	-8.8806	-11.180	-6.1749	-9.5430	-8.6616	-11.808
CYLAN	-9.0800	-11.500	-6.2000	-8.9600	-8.2300	-11.000
LST	-9.0879	-11.539	-6.2164	-8.3445	-7.6110	-10.204

Program	Smeared properties					
	Axial stress (ksi)			Hoop stress (ksi)		
	C6-1	C6-2	C6-3	C6-1	C6-2	C6-3
CCAP	-3.6274	-3.6573	-3.5028	-6.8310	-6.9401	-6.5527
ELCYL	-3.6274	-3.6573	-3.5028	-6.8310	-6.9401	-6.5527
CYLIN	-3.4572	-3.4883	-3.3334	-6.9143	-6.9767	-6.6668
CYLAN	-3.4500	-3.4900	-3.3300	-6.0400	-6.1100	-5.8000
FEM	-3.6137	-3.6352	-3.4821	-6.8110	-6.8967	-6.5219

Note: Applied pressure = 1.0 ksi

1.2 ANALYTIC ELASTIC STABILITY ANALYSIS

This subtask is concerned with the development of analytical theories for the elastic instability (buckling) of laminated composite cylindrical shells. The activities include the evaluation of existing theories and also the development of advanced higher-order theories. Analytic solutions are acquired from the literature and are coded for evaluation and comparison. The advanced theories are being developed from higher-order shell theory or from elasticity solutions.

During this year a total of five existing closed-form solutions for buckling of laminated composite cylindrical shells were obtained from the literature and evaluated. These solutions were coded and installed on mainframe or desktop computers. Representative sample problems were formulated and executed to compare the coded solutions and to validate results against experimental data. Results were also compared to finite element solutions to determine the range of applicability of these shell theories to the buckling analysis of thick composite cylinders.

Selected theories were applied to the analysis of various test articles to predict buckling failure. Results were compared to finite element solutions and to experimental data. Results from this initial phase have indicated the direction for development of improved theories in subsequent years.

1.2.1 Buckling Equations

Existing closed form analytic solutions for buckling of laminated composite cylindrical shells are most commonly formulated by using an orthotropic stiffness layer approach or a laminated shell theory approach. For the orthotropic stiffness layer theory, eight material constants are required for each layer when transverse shear deformations are neglected. To include transverse shear deformations in this theory requires that 12 constants per layer be specified.[18] Coupling between bending and extension is ignored in this approach and the reference surface must be at the midplane of the shell cross section, which is the centroid of a symmetric laminate. The orthotropic laminated shell theory requires only four material constants per layer and coupling between bending an extension is included (i.e., unsymmetric laminates can be analyzed). To account for transverse shear deformations in laminated shell theory requires only 6 constants to be specified for each layer.

Five different existing formulations for determining the critical hydrostatic pressure for a laminated cylinder were reviewed and coded into a computer program. The five formulations were based on either one of the two approaches described above and are as follows:

1. Jacobsen[19] - Orthotropic stiffness layer theory, symmetric laminate, reference surface at the middle
2. Baker[20] - Orthotropic stiffness layer theory, symmetric laminate, reference surface at the centroid
3. Cheng[21] - Anisotropic laminated shell theory, unsymmetric laminate, reference surface at the middle
4. Jones[22] - Orthotropic laminated shell theory, unsymmetric laminate, reference surface at the centroid (unconventional notation)
5. Jones[23] - Orthotropic laminated shell theory, unsymmetric laminate, reference surface at the middle (conventional [A],[B],[D] notation)

All five of these formulations were based on small-deflection, thin-shell theory, i.e., Donnell type equilibrium equations, and no transverse shear deformations. The assumed form of the displacements satisfied simply-supported boundary conditions at the cylinder ends with the exception of Cheng's formulation. For a general anisotropic laminated shell, the solution in Ref. 21 will not satisfy a given set of boundary conditions unless numerical methods are employed to solve a boundary characteristic equation. Consequently, Cheng's closed form solution is only applicable to very long cylinders where the end effects can be ignored. Also, the formulation in Ref. 21 differs from the other formulations in that z/R terms are retained. Typically, in thin-shell theories the thickness is assumed to be small such that z/R terms are neglected in comparison to unity. As Bushnell[24] noted, it may be inconsistent to retain z/R terms and not include transverse shear deformations. In other words, if the cylinder wall is thick enough to warrant the retention of z/R terms, then the effects of transverse shear can no longer be neglected.

Preliminary results indicated some inconsistencies between Cheng's solution and the remaining four approaches. In further review of the existing closed-form buckling equations, the inconsistency was discovered in the expressions used for the midplane curvatures. The kinematic relations for the strains in laminated shell theory are expressed in terms of the midplane strains and the midplane curvatures. These equations are derived from the integration of the strain-displacement relations and vanishing transverse shear strains. The midplane curvatures were shown by Ambartsumyan[13] to have the following form:

$$\kappa_x = -w,_{xx} \quad ,$$

(1.2.1-1)

$$\kappa_\theta = -\frac{1}{a^2}\left(w,_{\theta\theta} + w\right) \quad ,$$

(1.2.1-2)

$$\kappa_{x\theta} = -\frac{1}{a}\left(2w,_{x\theta} + \frac{1}{a}u,_\theta - v,_x\right) \quad ,$$

(1.2.1-3)

where a is the mean radius of the cylinder. Instead of these equations, most authors (e.g., Timoshenko[25] and Love[15]) use the following expressions for the curvatures:

$$\kappa_x = -w,_{xx} \quad ,$$

(1.2.1-4)

$$\kappa_\theta = -\frac{1}{a^2}\left(w,_{\theta\theta} - v,_\theta\right) \quad ,$$

(1.2.1-5)

$$\kappa_{x\theta} = -\frac{2}{a}\left(w,_{x\theta} - v,_x\right) \quad .$$

(1.2.1-6)

Cheng used Eqs. (1.2.1-1)-(1.2.1-3) for the curvatures, whereas Jones used the Donnell approximation which retains only those terms having derivatives of w, i.e.,

$$\kappa_x = -w,_{xx} \quad ,$$

(1.2.1-7)

$$\kappa_\theta = -\frac{1}{a^2}w,_{\theta\theta} \quad ,$$

(1.2.1-8)

$$\kappa_{x\theta} = -\frac{2}{a}w,_{x\theta} \quad .$$

(1.2.1-9)

Whitney[14] accounted for transverse normal strains by modifying the curvature expressions in Eqs. (1.2.1-1)-(1.2.1-3). To determine if the different results obtained by the

different approaches was directly related to the different expressions used for the curvatures, and to also include transverse normal strain, an additional solution was derived. This solution was based on modifying Flugge's[26] governing buckling equations for an isotropic cylinder to analyze a composite cylinder. The modifications used the underlying concepts of orthotropic laminated shell theory. Separate solutions were derived for each of the three different set of curvature expressions and for transverse normal strains. The assumptions were the same as stated in the above solutions, i.e., small-deflections, thin-shell theory, and no transverse shear deformations. The laminated cylinder was not restricted to being symmetric, i.e., coupling between bending and extension was included, and simply-supported boundary conditions were satisfied. In addition to the case of hydrostatic pressure loading, solutions were derived for determining the critical uniform axial pressure and the critical uniform lateral pressure. It should be noted that under the combined loading of lateral pressure and large axial compression, e.g., hydrostatic pressure, large deflection theory may be required (see Cheng[21]). The necessary buckling calculations for determining the critical pressures were incorporated into the computer program developed previously for the five existing formulations. The program also included the stress/strain calculations for an infinite cylinder based on laminated shell theory.

1.2.2 Stability Analysis Results

The buckling analyses described in Sect. 1.2.1 were performed for the case of a composite cylinder having both layered properties and equivalent smeared properties. The analytic predictions for the critical hydrostatic pressure are presented in Tables 1.2.2-1, 1.2.2-2, and 1.2.2-3 for cylinders C6-1, C6-2, and C6-3, respectively, and three different lengths, L = 18 in., 10 in., and 6 in. The results obtained from Jones' two equations are shown on a single line because the two approaches gave identical results. In comparing the different closed-form expressions for calculating the buckling pressure for a laminated cylinder, the tabulated results show that Jacobsen, Baker, and Jones equations all predict approximately the same values. Nearly identical values were obtained when the Donnell approximation for the curvatures was made in the extension of Flugge's work. In Cheng's equation and in the equation derived from Flugge's governing equation where the Donnell approximation is not used, lower buckling pressures are predicted. The tabulated results also indicate that the curvature expressions given by Timoshenko and the expressions given by Ambartsumyan[13] predict essentially the same critical pressure. For the cylinders analyzed in the present investigation, the results from using Whitney's curvature expressions indicate that the effects of a transverse normal strain are negligible. Also, the results show that modeling the laminated cylinders as single layers having equivalent smeared properties predicts almost the same buckling pressures as the layered analyses.

For the three lengths, all of the analyses predict cylinder C6-2 to have the highest buckling pressure and cylinder C6-3 to have the lowest. For example, the results based on the present extension of Flugge's work and on using curvature expressions from Ambartsumyan and L = 10 in. predict a 1.9% increase in the buckling pressure for C6-2 over C6-1 and predict C6-1 to have a 0.76% larger pressure than C6-3. The result that a 3:1 hoop to axial ply ratio cylinder has a larger buckling pressure than a 2:1 lay-up which has a larger buckling pressure than a 1:1 ratio of hoop to axial plies is not surprising. However, what is surprising is that only a 2.6% larger buckling pressure was predicted when 3 times as many hoop plies as axial plies were used compared to a 1:1 ratio. The buckling pressure for a homogeneous, infinitely long, orthotropic cylinder is proportional to the

flexural stiffness in the hoop direction, D_{yy}. Cylinders C6-1, C6-2, and C6-3 have flexural hoop stiffnesses, D_{yy}, of 164.3, 174.4, and 151.2 kip-in., respectively. This corresponds to a 14.8% increase in the flexural hoop stiffness from the 1:1 cylinder to the 3:1 cylinder. Therefore, in the case for the cylinder being considered in this investigation, it was unexpected that only a 2.6% increase in the buckling pressure was predicted for a length-to-diameter (L/D) ratio of approximately 1.7.

Further comparisons were made by plotting the critical pressure as a function of the L/D ratio. For all L/D ratios considered, the predicted buckling pressures based on using the curvature expressions from Timoshenko were nearly identical to the pressures predicted from using the Ambartsumyan curvatures. Also, it was seen that for the cylinders being studied, i.e., cylinders having only axial and hoop layers, the transverse normal strains had a negligible effect on the buckling pressures independent of the L/D ratio. Results were generated for hydrostatic pressure loading, uniform lateral pressure loading, and uniform axial compression based on Jones' equation and the present extension of Flugge's work using Ambartsumyan curvatures and the Donnell curvature approximation.

37

Table 1.2.2-1. C6-1 buckling analysis

Layered properties			
	Critical pressure (ksi)		
Equation	L=18 in.	L=10 in.	L=6 in.
Jacobsen	27.054	30.102	39.676
Baker	27.356	30.761	41.072
Jones	27.206	30.254	39.498
Cheng & Ho	20.873	24.902	35.312
Starbuck[a]	20.812	24.829	35.210
Starbuck[b]	20.881	24.948	35.424
Starbuck[c]	20.804	24.813	35.277
Starbuck[d]	27.387	30.916	40.296

Smeared properties			
	Critical pressure (ksi)		
Equation	L=18 in.	L=10 in.	L=6 in.
Jacobsen	26.536	29.649	39.461
Baker	26.712	30.182	40.728
Jones	26.565	29.685	39.167
Cheng & Ho	20.398	24.511	35.190
Starbuck[a]	20.339	24.435	35.074
Starbuck[b]	20.406	24.552	35.289
Starbuck[c]	20.330	24.420	35.145
Starbuck[d]	26.752	30.378	40.050

[a] Curvature expressions from Timoshenko and Love
[b] Curvature expressions from Ambartsumyan
[c] Curvature expressions from Whitney
[d] Curvature expressions from the Donnell approximation

38

Table 1.2.2-2. C6-2 buckling analysis

Layered properties			
	Critical pressure (ksi)		
Equation	L=18 in.	L=10 in.	L=6 in.
Jacobsen	28.634	31.161	39.574
Baker	28.931	31.802	40.924
Jones	28.774	31.285	39.376
Cheng & Ho	21.972	25.429	34.697
Starbuck[a]	21.907	25.355	34.592
Starbuck[b]	21.977	25.422	34.801
Starbuck[c]	21.886	25.306	34.621
Starbuck[d]	28.915	31.848	39.993

Smeared properties			
	Critical pressure (ksi)		
Equation	L=18 in.	L=10 in.	L=6 in.
Jacobsen	28.253	30.831	39.427
Baker	28.423	31.346	40.652
Jones	28.269	30.836	39.114
Cheng & Ho	21.596	25.119	34.602
Starbuck[a]	21.533	25.043	34.484
Starbuck[b]	21.601	25.159	34.694
Starbuck[c]	21.513	24.996	34.516
Starbuck[d]	28.414	31.422	39.798

[a] Curvature expressions from Timoshenko and Love
[b] Curvature expressions from Ambartsumyan
[c] Curvature expressions from Whitney
[d] Curvature expressions from the Donnell approximation

Table 1.2.2-3. C6-3 buckling analysis

	Layered properties		
	Critical pressure (ksi)		
Equation	L=18 in.	L=10 in.	L=6 in.
Jacobsen	25.024	29.083	41.414
Baker	25.346	29.815	43.000
Jones	25.199	29.298	41.269
Cheng & Ho	19.526	24.704	37.938
Starbuck[a]	19.465	24.627	37.836
Starbuck[b]	19.539	24.759	38.076
Starbuck[c]	19.480	24.659	37.962
Starbuck[d]	25.460	30.194	42.555

	Smeared properties		
	Critical pressure (ksi)		
Equation	L=18 in.	L=10 in.	L=6 in.
Jacobsen	24.109	28.276	41.000
Baker	24.311	28.887	42.453
Jones	24.170	28.385	40.743
Cheng & Ho	18.763	24.080	37.743
Starbuck[a]	18.707	23.999	37.624
Starbuck[b]	18.777	24.129	37.865
Starbuck[c]	18.720	24.032	37.755
Starbuck[d]	24.443	29.336	42.169

[a] Curvature expressions from Timoshenko and Love
[b] Curvature expressions from Ambartsumyan
[c] Curvature expressions from Whitney
[d] Curvature expressions from the Donnell approximation

Shown in Figs. 1.2.2-1 through 1.2.2-3 are the predicted critical hydrostatic pressures for cylinders C6-1, C6-2, and C6-3, respectively. In all three figures the results show that as L/D becomes large, the solutions based on the Donnell approximation for the curvatures approach a magnitude of $4D_{yy}/R^3$. The same expression, where R is the mean radius, was obtained analytically by letting the length of the cylinder, L, approach infinity. For an orthotropic cylinder,

$$D_{yy} = \frac{E_{yy}I}{1 - v_{xy}v_{yx}} \quad , \tag{1.2.2-1}$$

where $I = h^3/12$, and h is the cylinder thickness. When derivatives of the axial and hoop displacement components are retained in the curvature expressions (e.g., Ambartsumyan and Timoshenko) lower critical hydrostatic pressures are predicted that approach $3D_{yy}/R^3$ as L/D becomes large. This agrees with Timoshenko's[25] well-known result for an isotropic tube. Again, it was analytically shown that by letting L go to infinity in the solution, the expression for the critical hydrostatic pressure reduces to $3D_{yy}/R^3$. These three figures also illustrate that the critical pressure approaches the infinite length solution very rapidly and at a rather small L/D ratio equal to approximately 7.0. The same observations were made when uniform lateral pressure was considered, as shown in Figs. 1.2.2-4 through 1.2.2-6. The magnitude of the critical lateral pressure is the same as the case of hydrostatic pressure when L approaches infinity, which indicates the axial component of pressure in the hydrostatic loading becomes negligible when L becomes large.

A comparison between the predicted critical hydrostatic pressure and the critical uniform lateral pressure as a function of L/D is made in Fig. 1.2.2-7. The results are for cylinder C6-1, and they show larger pressures are predicted for the case of uniform lateral pressure. As the L/D ratio increases, the decrease in the critical pressure due to the axial compression associated with hydrostatic pressure is seen to decrease. Presented in Figs. 1.2.2-8 through 1.2.2-10 are the results for cylinders C6-1, C6-2, and C6-3, respectively, and uniform axial compression. The predicted critical pressures are nearly identical when Flugge's equations are used with Ambartsumyan curvatures and with the Donnell approximations. However, the predicted pressures based on Jones' formulation are significantly different with the critical pressure increasing as the L/D ratio is increased. In fact, the analytic solution from Jones predicts an infinite critical pressure as the length of the cylinder approaches infinity.

As stated previously, there was only a 2.6% difference between the critical hydrostatic pressures for cylinders C6-3 and C6-2 when the L/D ratio was equal to 1.7. In Fig. 1.2.2-11 the critical hydrostatic pressures are shown as a function of L/D for the three different cylinder configurations. As L/D becomes large the differences in the predicted pressures are directly proportional to the differences in the flexural hoop stiffness. Consequently, C6-3 has a smaller critical pressure than C6-1, which has a smaller critical pressure than C6-2. It is interesting to note that at an L/D of approximately 1.5 there is no difference in the critical pressure for all three cylinders. Also, for L/D less than 1.5, the results show that C6-3 has the largest critical pressure and C6-2 has the smallest. Still, the differences predicted for the critical hydrostatic pressures in the three cylinders are not as great as were expected over the entire range of L/D ratios shown. Similar trends were observed in Fig. 1.2.2-12 for the critical uniform lateral pressure. For uniform axial compression, the

critical pressures for the three cylinders are compared in Fig. 1.2.2-13. Cylinder C6-3, which has the largest percentage of axial plies, has the largest critical pressure for all L/D ratios considered. This is not surprising because the mode of buckling in this case is governed by the axial stiffness of the cylinder. This figure also shows that cylinder C6-2 has the lowest critical axial compression.

CRITICAL HYDROSTATIC PRESSURE
Cylinder C6-1
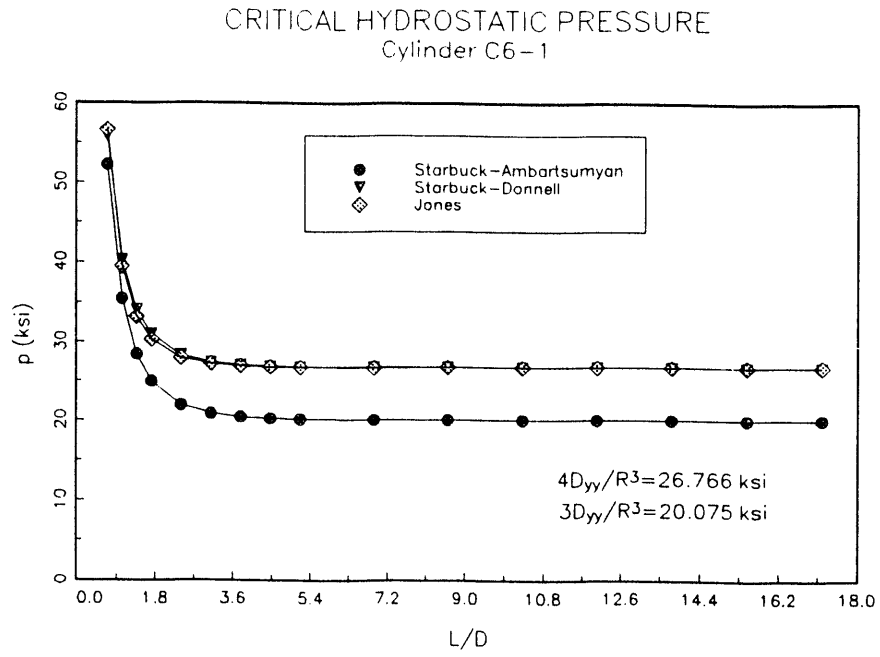
Fig. 1.2.2-1. Critical hydrostatic pressure for cylinder C6-1.

CRITICAL HYDROSTATIC PRESSURE
Cylinder C6-2
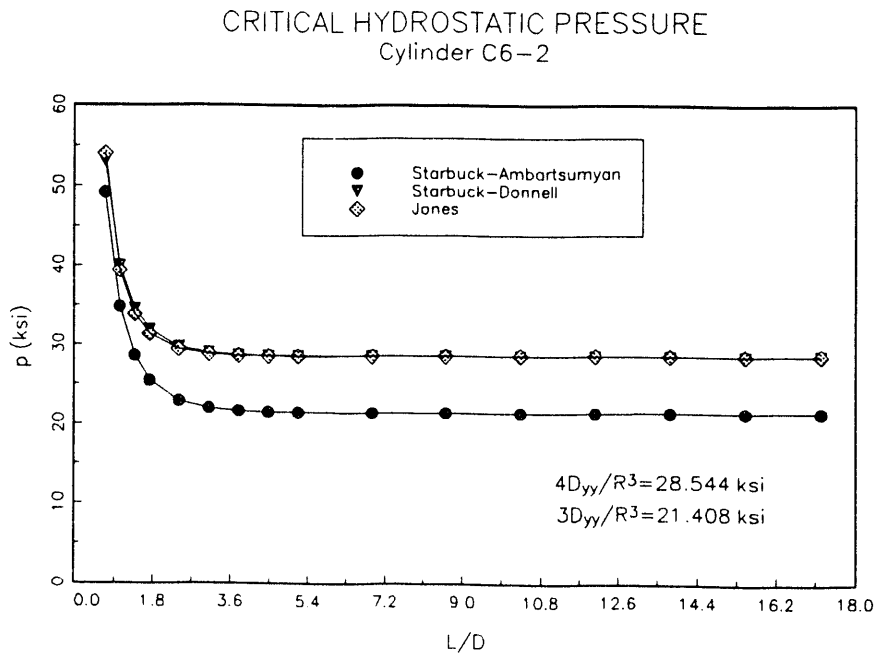
Fig. 1.2.2-2. Critical hydrostatic pressure for cylinder C6-2.

CRITICAL HYDROSTATIC PRESSURE
Cylinder C6-3
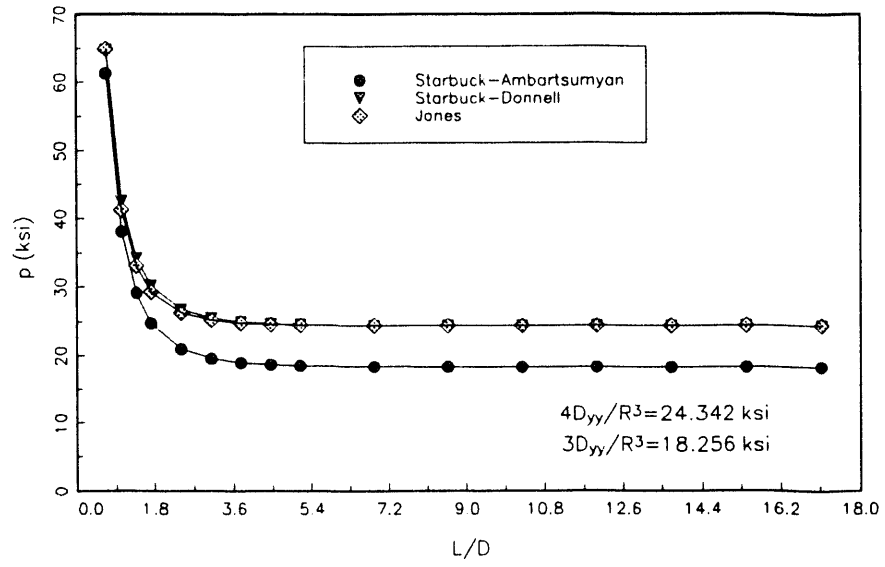
Fig. 1.2.2-3. Critical hydrostatic pressure for cylinder C6-3.

CRITICAL LATERAL PRESSURE
Cylinder C6-1
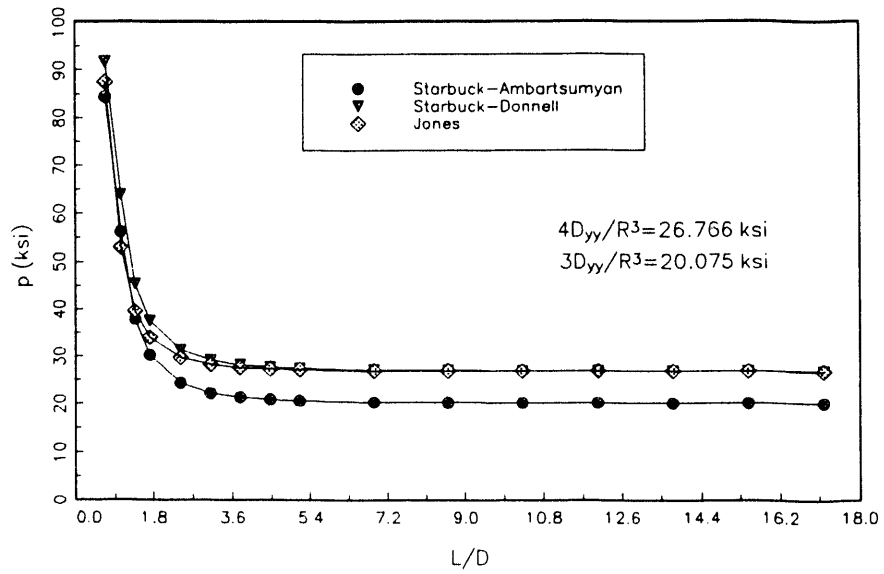
Fig. 1.2.2-4. Critical lateral pressure for cylinder C6-1.

CRITICAL LATERAL PRESSURE
Cylinder C6-2

$4D_{yy}/R^3=28.544$ ksi
$3D_{yy}/R^3=21.408$ ksi
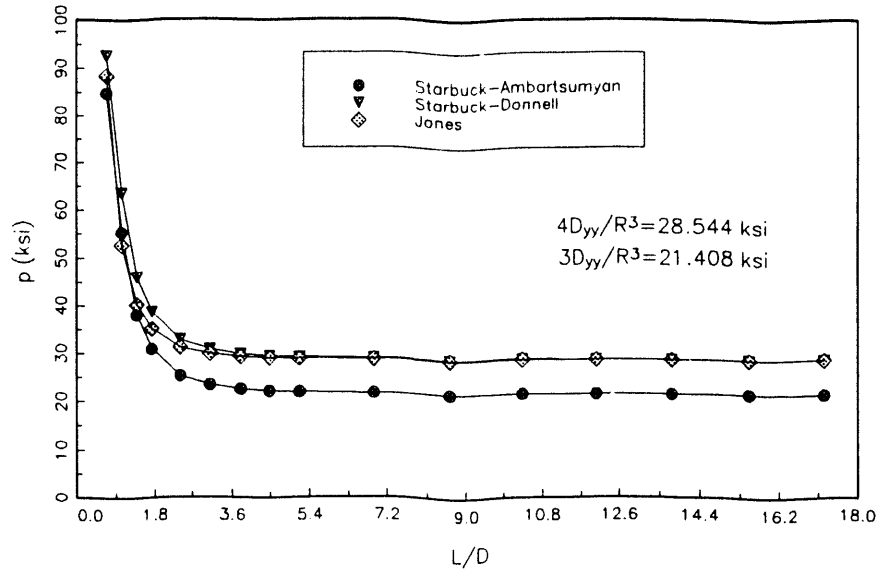
Fig. 1.2.2-5. Critical lateral pressure for cylinder C6-2.

CRITICAL LATERAL PRESSURE
Cylinder C6-3

$4D_{yy}/R^3=24.342$ ksi
$3D_{yy}/R^3=18.256$ ksi
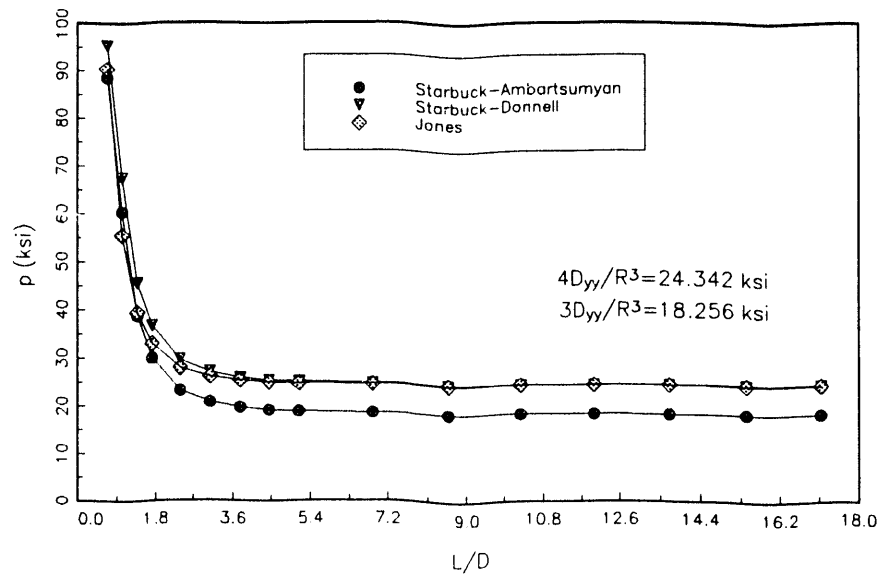
Fig. 1.2.2-6. Critical lateral pressure for cylinder C6-3.

CRITICAL HYDROSTATIC AND LATERAL PRESSURE
Cylinder C6-1
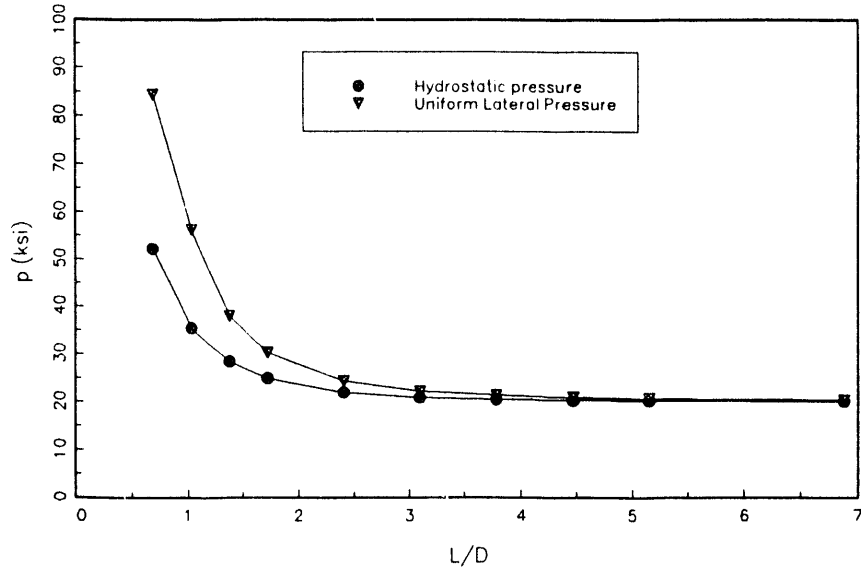
Fig. 1.2.2-7. Comparison between critical hydrostatic and lateral pressure for cylinder C6-1.

CRITICAL AXIAL PRESSURE
Cylinder C6-1
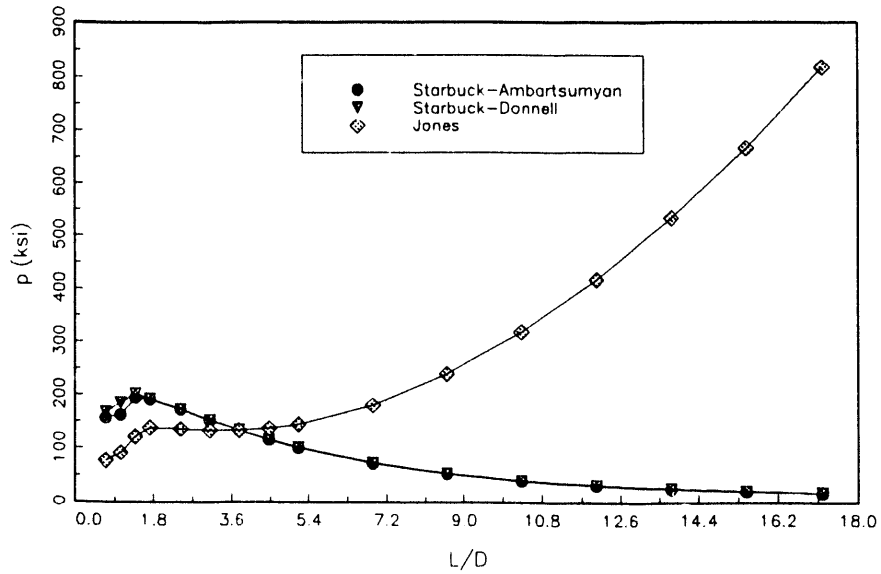
Fig. 1.2.2-8. Critical axial pressure for cylinder C6-1.

CRITICAL AXIAL PRESSURE
Cylinder C6-2
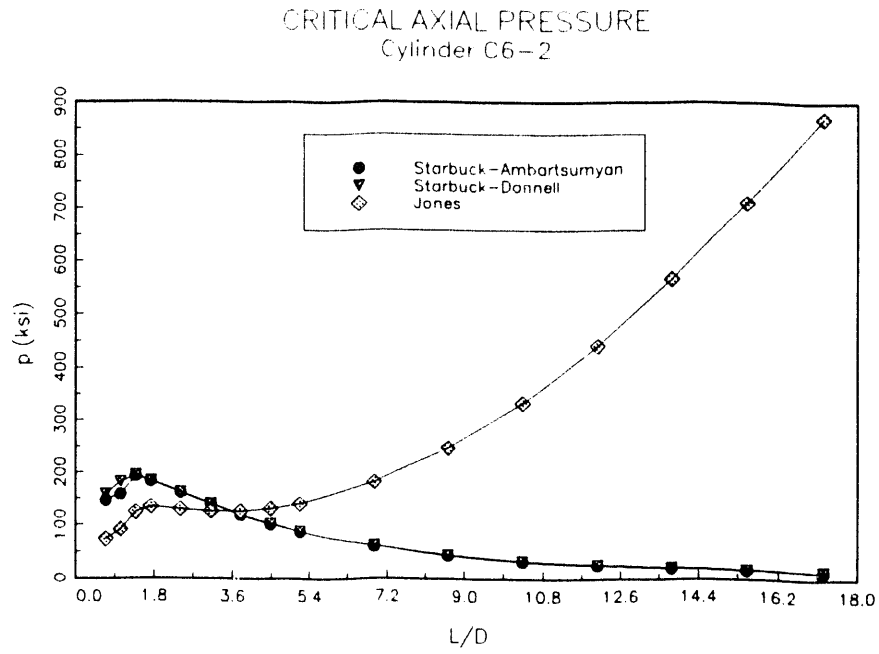
Fig. 1.2.2-9. Critical axial pressure for cylinder C6-2.

CRITICAL AXIAL PRESSURE
Cylinder C6-3
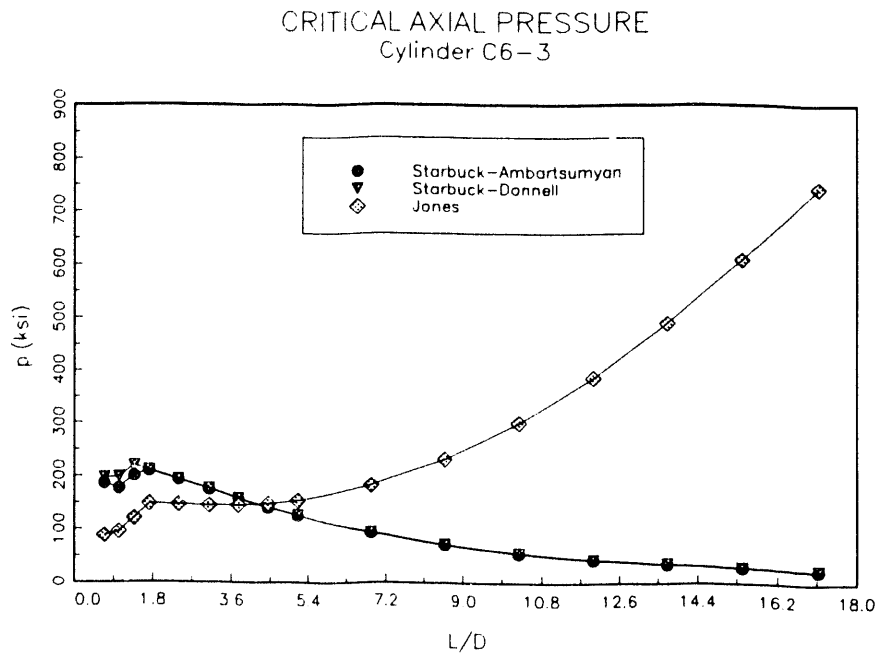
Fig. 1.2.2-10. Critical axial pressure for cylinder C6-3.

47
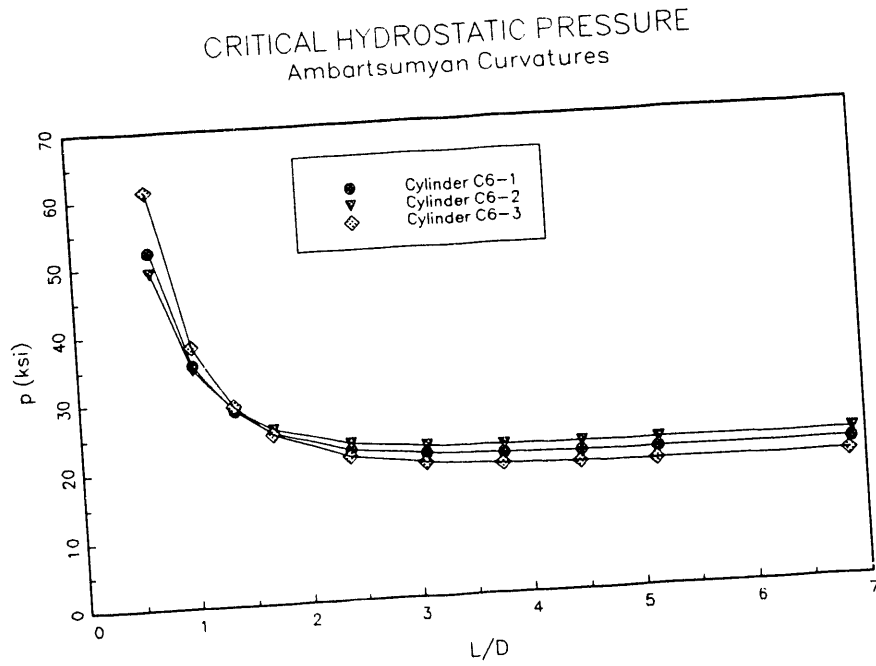
Fig. 1.2.2-11. Critical hydrostatic pressures versus L/D for C6-1, C6-2, and C6-3.
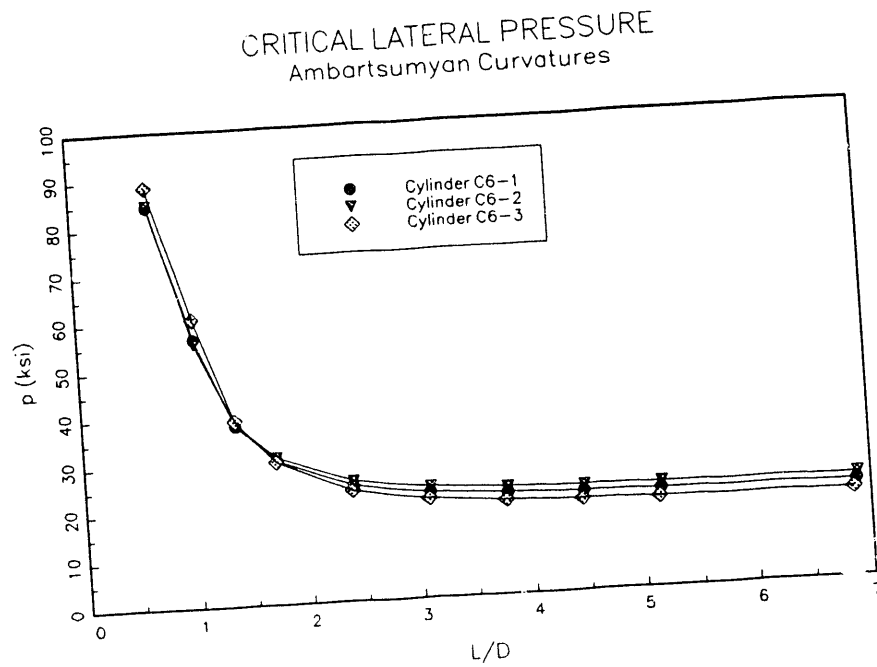
Fig. 1.2.2-12. Critical lateral pressures versus L/D for C6-1, C6-2, and C6-3.
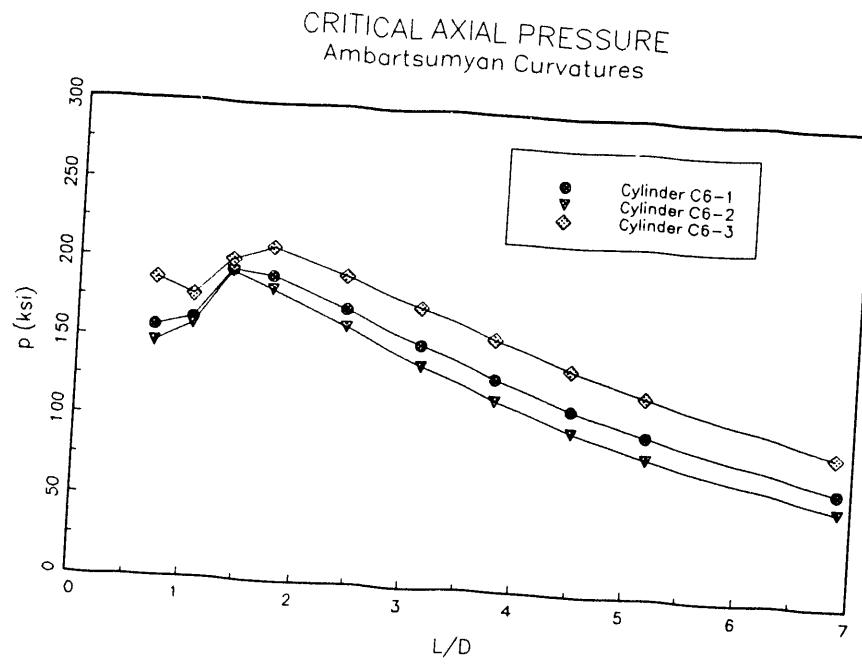
Fig. 1.2.2-13. Critical axial pressures versus L/D for C6-1, C6-2, and C6-3.

1.3 FINITE ELEMENT STRESS ANALYSIS

The finite element (FE) stress analysis method is also being used to determine internal stresses and deformations of the various test articles. In general, the FE method provides detailed stress results for complex loading or boundary conditions. In the present work, the FE method is being used to augment the analytic solutions. FE methods are applied to analyze regions of the cylinder where the analytic solutions do not apply or are not yet available. This is the case near the ends of the cylinder where complex bending and shear stresses occur.

The analytic solutions that were available at the start of this project were limited to generalized plane strain assumptions. Axial gradients of all state variables are zero in the plane strain formulation. These conditions are met (approximately) only in the region near the cylinder midplane where axial bending and shear stresses are negligible. These solutions do not apply in the regions adjacent to the end closures where high axial bending and shear stresses occur. FE stress analysis is used to provide detailed stress results in these regions. FE models of various ring specimens and cylinder test assemblies are constructed to provide detailed stresses. These models provide results for evaluating cylinder end effects caused by the interaction of the cylinder with the end closures.

State-of-the-art FE codes and computing capabilities are being sought that will permit the determination of stresses on a ply-by-ply basis. Substructuring techniques and extreme mesh refinement will be employed as required to model the individual layers of the composite laminate. Volume averaged (smeared) elastic properties will be utilized in regions of uniform stress to reduce model degrees of freedom. Substructured or refined model regions will be interfaced to regions where smeared properties are applied using appropriate continuity or equilibrium conditions. FE results will be compared to analytic solutions to validate results. Selected FE codes will also be interfaced to the failure analysis codes developed under Task 1.4. This capability will eventually allow the study of laminate free edge effects which are expected to influence failure initiation at the cylinder ends.

FE models are constructed for each test cylinder assembly and analyzed to determine local stress values within the volume and on the surfaces of the cylinder and the metal end closures. The drawing of a typical test assembly is shown in Fig. 1.3-1.

In addition to the detailed models of entire test assemblies that include the cylinder and end closures, models of the cylinders without the end closures were also constructed. The effect of the axial thrust of the hydrostatic pressure acting on the end closures was approximated by the application of a uniform pressure on the cylinder ends. This pressure value was derived from the hydrostatic pressure and the ratio of the cylinder end area to cross-sectional area. These "cylinder only" models provided displacements, strains, and composite stress values for comparison with the analytic solutions. In these cases, smeared elastic properties were used in the analytic solutions to obtain the composite stress values for comparison with the FE results.

Initially, smeared elastic properties are being used for the composite material until the analysis capability to model the individual layers has been developed. Stress values from these initial analyses are, therefore, the composite stresses rather than the layer stresses.
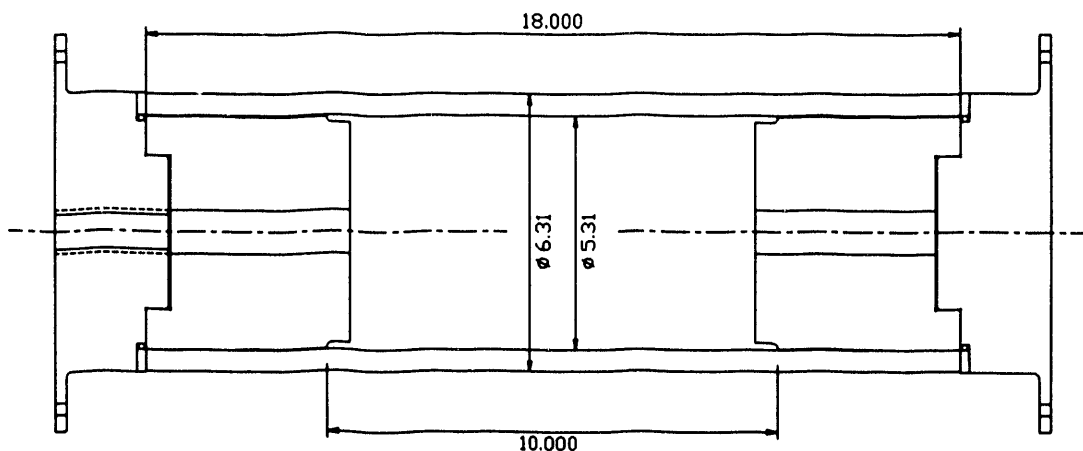
Fig. 1.3-1. Cylinder test assembly.

Results from the initial FE analysis on the first test cylinder assembly are summarized in Sect. 1.3.1. These values are representative of the typical cylinder, although actual stress values vary depending on the cylinder composite material properties and the end closures.

1.3.1 Finite Element Model

The FE model of the test assembly for cylinder C6-1 is described in this section. This initial model is typical of the models for all cylinders in this project. A separate model is required for each test cylinder assembly because of differences in cylinder dimensions, material properties, and end closure design.

This cylinder was the first to be designed, fabricated, and tested under the present project. It was also the first test cylinder assembly that utilized the end closures of the improved linear taper design. This cylinder was subjected to external pressurization[27] and sustained a maximum hydrostatic pressure of 20,000 psig without failure. This was the highest pressure achieved, to date, for this material and cylinder configuration.

An axisymmetric FE model of the cylinder test assembly was constructed for analysis with the Lawrence Livermore National Laboratory (LLNL) generated FE program NIKE2D.[28] The model was generated by using the LLNL mesh generation program MAZE.[29] Postprocessing of the analysis results from NIKE2D was done with the LLNL program ORION.[30] The model outline is shown in Fig. 1.3.1-1.

The model included only one quadrant of the test assembly cross section as shown in Fig. 1.3.1-1. This "one quarter" model was sufficient because of the axisymmetric geometry and symmetry of the stress distributions at the cylinder midplane. The model included the cylinder and the end closure assembly.

```
DR&D  CYL  6-1
TIME:   0.00000E+00
DSF  =   0.10000E+01
```
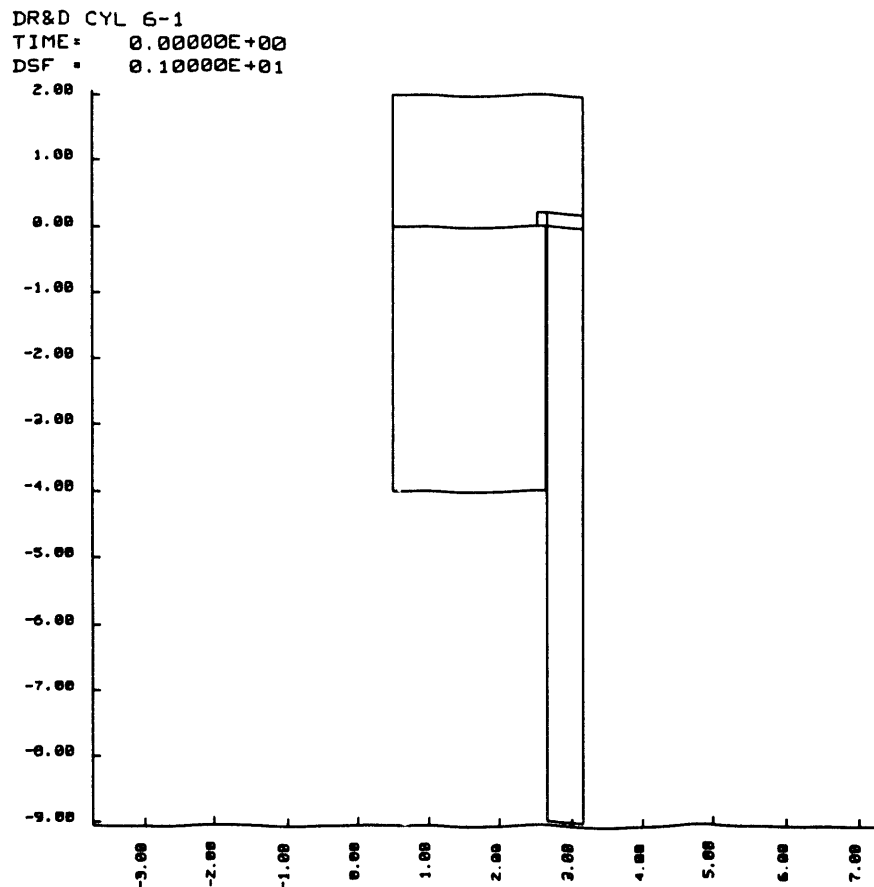
Fig. 1.3.1-1. Outline plot of axisymmetric model.

The end closure assembly is made of four parts: a steel end plate, an aluminum end plug, a steel end ring, and an o-ring seal (see Figs. 1.3-1 and 3.2-1). The aluminum end plug is joined to the end plate by thermal shrink fit of the plug over a boss on the end plate. The two-piece design of the end plate/end plug assembly allows the end plates to be used with several different end plug designs and facilitates the replacement of the plug whenever it is damaged during a cylinder failure. The use of an aluminum end plug instead of an all steel closure reduces the weight of the end closure assembly.

Several simplifications were made in the FE model to facilitate the analysis. The end plug and end plate were perfectly joined across a plane interface in the FE analysis, whereas the actual parts are joined by thermal shrink fit of the plug onto the protrusion on the end plate. These details were not modeled in the FE representation because the primary objective of the analysis was to determine the cylinder stresses rather than detailed stresses in the end closure. The robust design of the end plate and end plug insured that the stresses in the metal components were low.

The end plates have an integral flange and bolt circle that provide points of attachment for threaded tie rods which connect between the two end closures. The tie rods are tensioned via locking nuts to obtain an initial clamping force to secure the end closures

against each end of the cylinder. To simplify the model, the flange; bolt circle; and tie rods were not included. These features were not expected to significantly affect the cylinder stresses because the stiffness of the flange is low and the clamping load is small compared to the loads that result from the hydrostatic pressure.

One of the two end closures has a 1-inch threaded hole in the end plate for the penetrator, which provides feedthrough for the strain gage lead wires from the interior strain gages. The hole was included in the model. The penetrator was not modeled. The axial thrust load for the penetrator was included by multiplying the pressure applied to the end area of the plate by an appropriate area ratio.

The end ring is held in place in the end closure assembly by the o-ring. The o-ring provides centering of the end ring relative to the end plate and end plug. This insures that the end ring is held concentric with the end plug until the end closures are secured with the tie rods. The o-ring was not included in the initial model. After this initial cylinder test, the o-ring was replaced by a "quad" ring. The quad ring was included in all subsequent FE models.

The frictional sliding and contact between the cylinder and end closure was modeled by using the nonlinear frictional slideline capabilities of NIKE2D. Three interfaces were modeled. These were the interface between the cylinder end and the end ring, the interface between the end ring and the end plate, and the interface between the inner surface of the cylinder and the tapered surface of the end plug. These interfaces were modeled by using a slideline option that allows for sliding friction or a gap, as required, for the specified initial clearances and for overall equilibrium. The slideline feature prevents penetration of one material into the other. The normal pressure and maximum shear stress on the contacting surfaces are related by a specified coefficient of friction. Frictional sliding occurs as demanded for overall equilibrium. This permits sliding of the cylinder ends relative to the end rings and sliding of the end rings relative to the end plates. The end ring has a slight conical taper on the side, which contacts the end plate. The initial clearance due to this taper closes as the pressure is applied. This action provides for a controlled rotation of the cylinder end. There is also an initial radial clearance between the inner radius of the cylinder and the outer radius of the end plug. This clearance closes as the external pressure is applied, providing radial support to the cylinder as the pressure increases. The FE mesh is shown in Fig. 1.3.1-2.
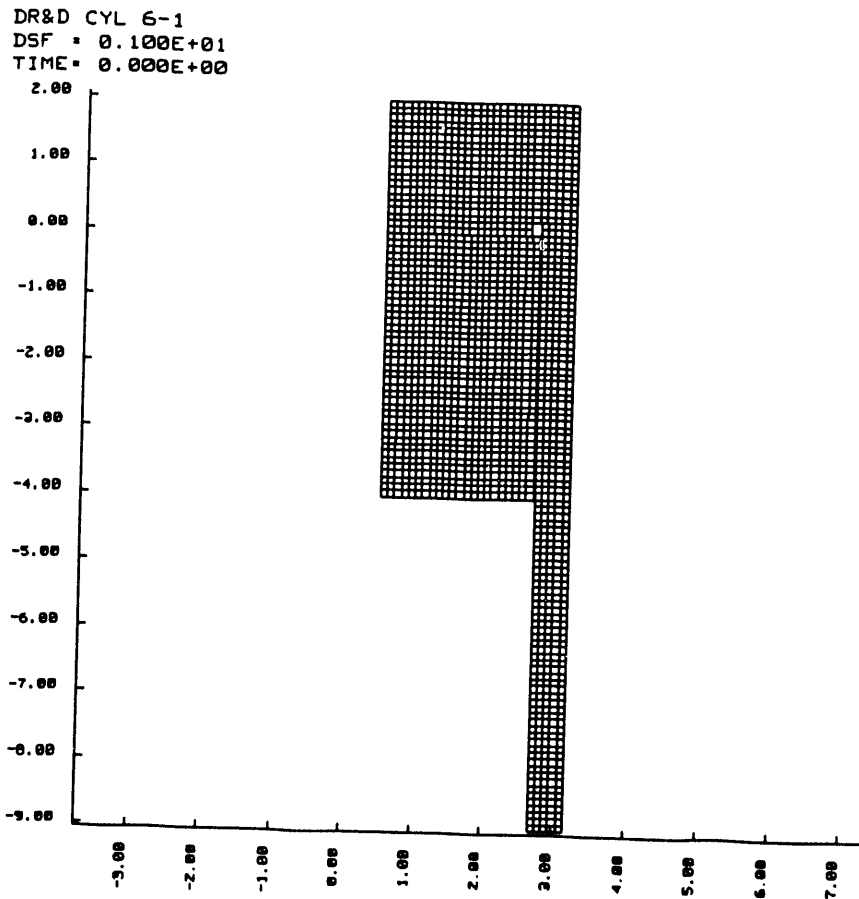
Fig. 1.3.1-2. Finite element mesh.

The elements in this model were two-dimensional four-noded axisymmetric quadrilateral isoparametric solid elements. The NIKE2D code has only the four-noded quadrilateral element in its element library. These elements are essentially linear elements and use a low order of interpolation and numerical integration. This type of element requires a relatively fine mesh to reduce discretization errors and to provide the required accuracy. Other codes such as NISA II,[31] ABAQUS,[32] and ADINA[33] offer higher-noded elements having higher order interpolation and integration. A coarser mesh can be used with these elements than with the linear four-noded element. However, NIKE2D has the advantage of automatic mesh generation with MAZE and automatic generation of slideline and pressure data for frictional slidelines that make it attractive for this application. Model generation for ABAQUS and ADINA is more laborious and tedious because of the limited mesh generation capabilities provided with these codes. Both MAZE and NIKE2D also offer automatic bandwidth optimization of the stiffness matrix. This is particularly beneficial when slidelines are used. The model in Fig. 1.3.1-3 contained 1868 elements and 2083 nodes. The model had a total of 4160 unconstrained degrees of freedom.

The cylinder material was modeled as an orthotropic material by using smeared elastic constants for the laminate. The elastic constants were computed with the NDPROP code, which yields volume-averaged composite elastic properties from input layer properties and laminate stacking sequence. The smeared elastic properties are given in Table 1.3.1-1. The in-plane properties were also checked with the CLASS code.

Table 1.3.1-1. Orthotropic material elastic constants for cylinder C6-1

Component	r	θ	z	rz	θz	θr
Young's Modulus (MSI)	1.676	15.852	8.387	-	-	-
Shear Modulus (MSI)	-	-	-	.643	.857	.754
Poisson's Ratio	-	-	-	.0778	.0555	.3954

Poisson ratios in Table 1.3.1-1 are given in the load-strain convention. The components in Table 1.3.1-1 refer to the coordinate direction and subscript index for tensor components (i.e., first subscript indicates the load direction and the second subscript indicates the direction of the strain response).

1.3.2 Stress Analysis Results

FE stress analysis results from the model shown in Fig. 1.3.1-2 are summarized in this section. These results are illustrative of the analyses results obtained for each test cylinder. A separate model is required for each test cylinder assembly because of differences in cylinder dimensions, material properties, and end closure design.

An incremental nonlinear solution method was applied with the pressure increasing incrementally in accordance with a linear increase from 0 psi to a maximum value of 20,000 psi. The load was applied in 20 equal load increments. Equilibrium iterations and stiffness matrix reformations were permitted at each load step. The solution converged over the entire range of pressures within the tolerances prescribed.

The analysis results were postprocessed with the ORION code. In general, several types of plots were generated at selected load states. These included contour plots of the displacements, stresses, and strains; displaced outline plots; and interface plots. Line plots of selected variables were also produced for selected boundary lines on the cylinder. The line plots give the variation of the selected variable along the chosen boundary. Line plots are selected for free edges or planes of symmetry. Interface plots are produced for contacting surfaces.

The displaced outline plots are particularly useful for visualizing the deformations and the relative displacement of mating parts during the load application. In this case, the displaced outline plots show the closing of the clearance between the cylinder and end plug

as pressure is increased. This was used to verify the end plug design calculations. The displaced outline plot of the cylinder is shown in Fig. 1.3.1-3 for an applied pressure of 20,000 psi. This plot shows the cross section of the cylinder and portions of the end plug, end plate, and end ring. The reader should be aware that the aspect ratio of this plot is not 1:1, because a zoom feature was used in ORION to select the area for plotting.
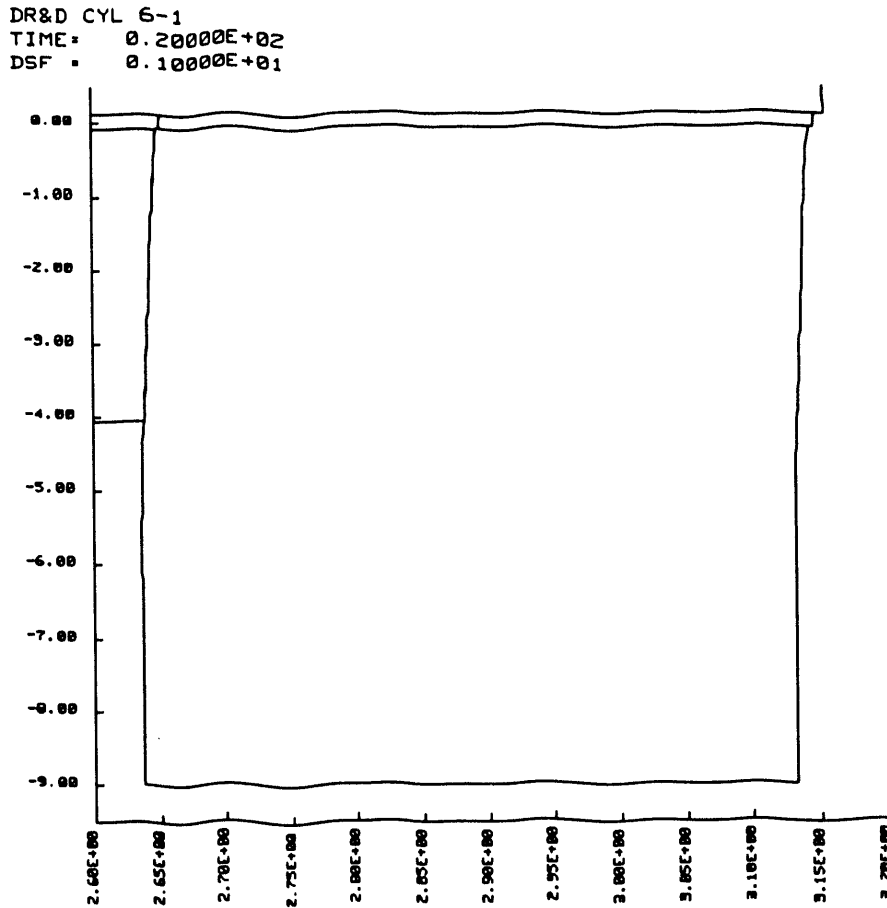
Fig. 1.3.1-3. Displaced outline of cylinder cross-section.

This plot shows that at the maximum pressure (20,000 psi), the initial radial clearance between the cylinder and plug has completely closed along the entire length of the plug. This was also confirmed by the interface plot of the normal pressure between the cylinder and the plug.

Contour plots were generated for displacements, stresses, and strains for values of several different pressures. To illustrate the results, plots for 20,000 psi are included. The contour plots for radial and axial displacements are given in Figs. 1.3.1-4 and 1.3.1-5. The radial displacement of the cylinder inner radius at 20,000 psi is slightly greater than the initial radial clearance at the end of the plug. This result validates the design of the taper

and gap of the plug. The axial displacement contour lines in the cylinder (see Fig. 1.3.1-5) are nearly horizontal which indicates that the axial load is nearly uniform across the end face of the cylinder. This result verifies the function of the end ring.

Stress contour plots for each component of stress are shown in Figs. 1.3.1-6 through 1.3.1-9. These stresses are the smeared composite stresses rather than layer stresses. Layer stress values can be estimated from the composite stress values given the ply ratio of the lay-up. The axial stress and shear stress plots are used to determine the peak bending and shear stress in the cylinder near the end of the plug. These contour plots indicate that the bending stress is below 5 ksi and that the peak shear stress is approximately 700 psi.

Strain contour plots for each component of strain are given in Figs. 1.3.1-10 through 1.3.1-13. The strain values apply to either the layered or smeared materials because of strain compatibility in the laminate formulation.

Interface plots for the interface between the cylinder end face and the end ring were generated for a range of load states. Figs 1.3.1-14 and 1.3.1-15 give the plots for the normal pressure and shear stress. The abscissa in Figs. 1.3.1-14 and 1.3.1-15 is the distance along the interface measured from the outer radius toward the inner radius. Each curve in these plots corresponds to a single pressure value. The state numbers correspond to the pressure, expressed in ksi, plus one (i.e., state 21 corresponds to 20,000 psi). The pressure curves at the higher load states are nearly horizontal, indicating uniform loading of the cylinder end by the end closure. The peak axial stress occurs at the outer radius of the cylinder but is only slightly higher than the axial stress value at the inner radius (i.e., 79 ksi versus 64 ksi). The interface shear stress values are low except for the end point values (near the corners of the cylinder cross section). These values are probably not accurate; the FE method has inaccuracies at corner elements due to the four-noaed element and the interpolation of the interior point values to the edges.
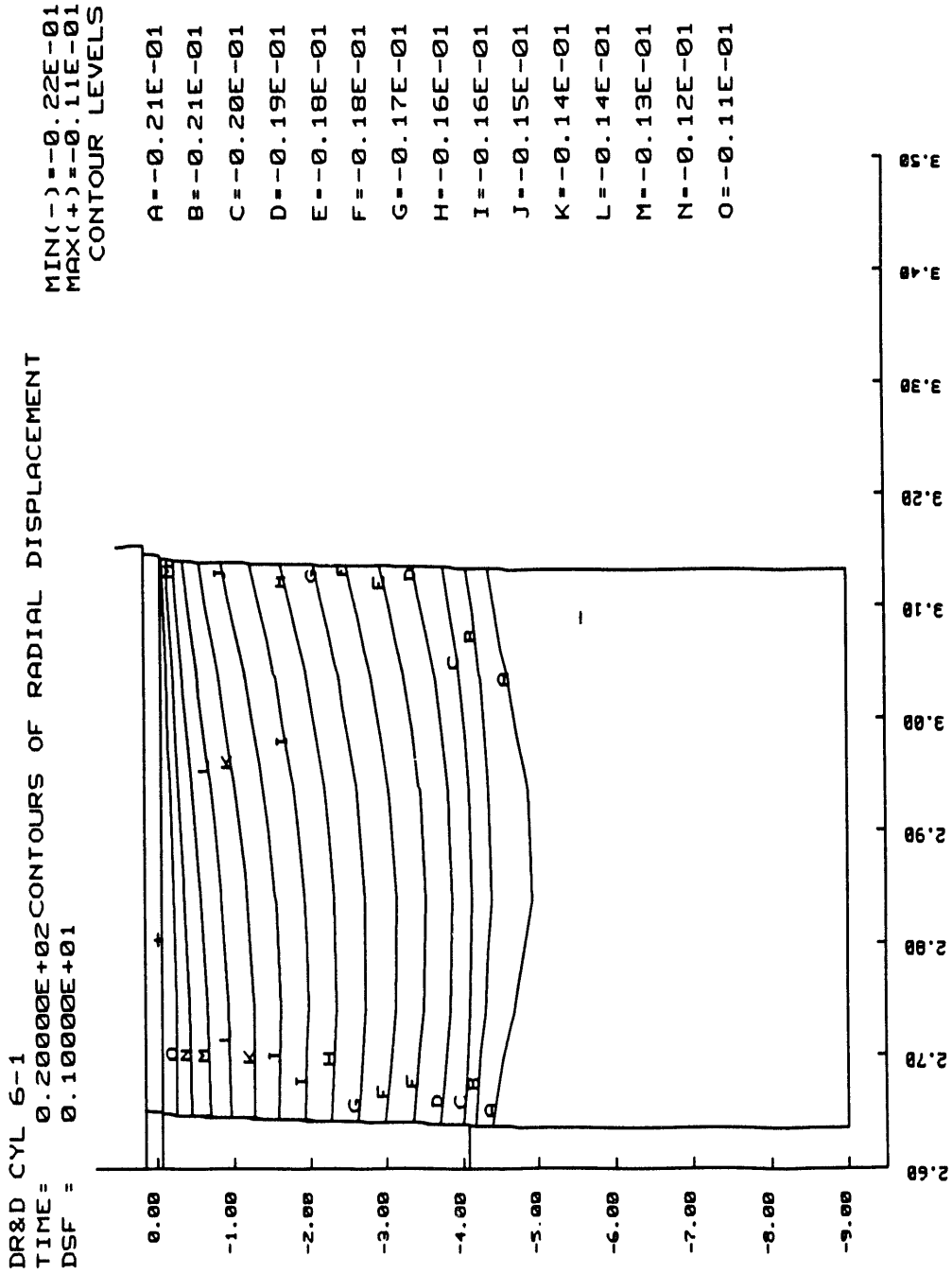
Fig. 1.3.1-4. Contours of radial displacement.
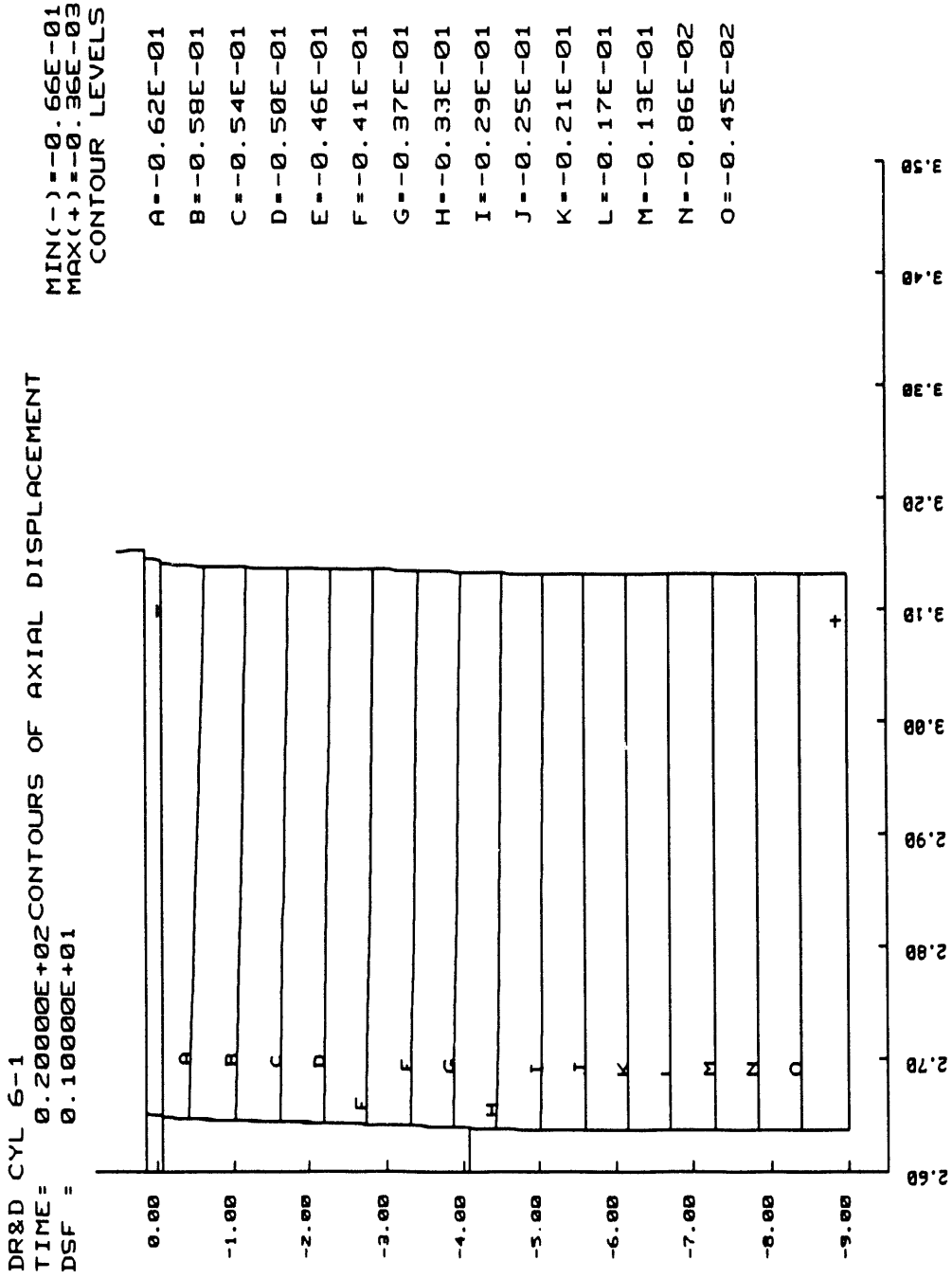
Fig. 1.3.1-5. Contours of axial displacement.
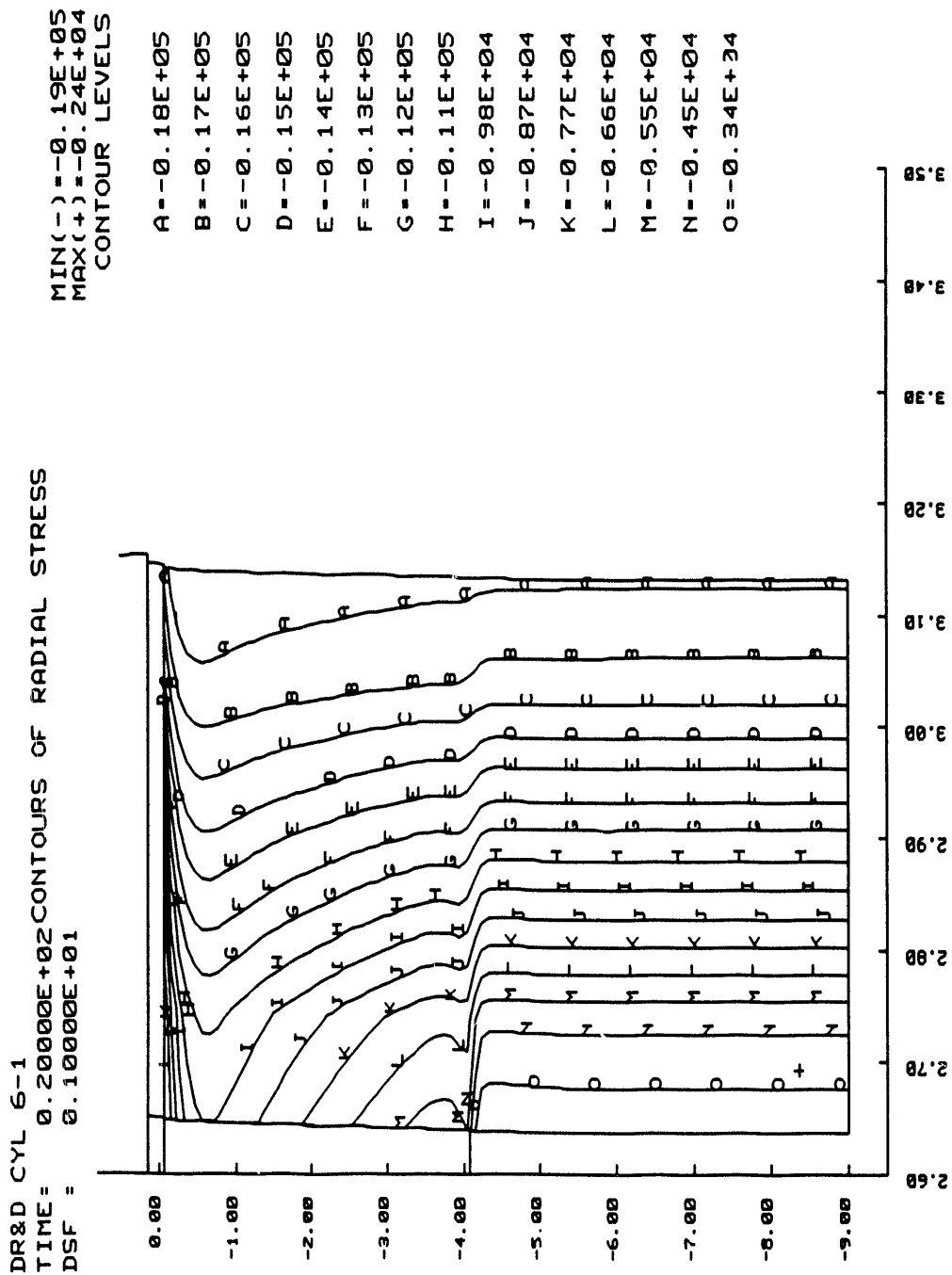
Fig. 1.3.1-6. Contours of radial stress.
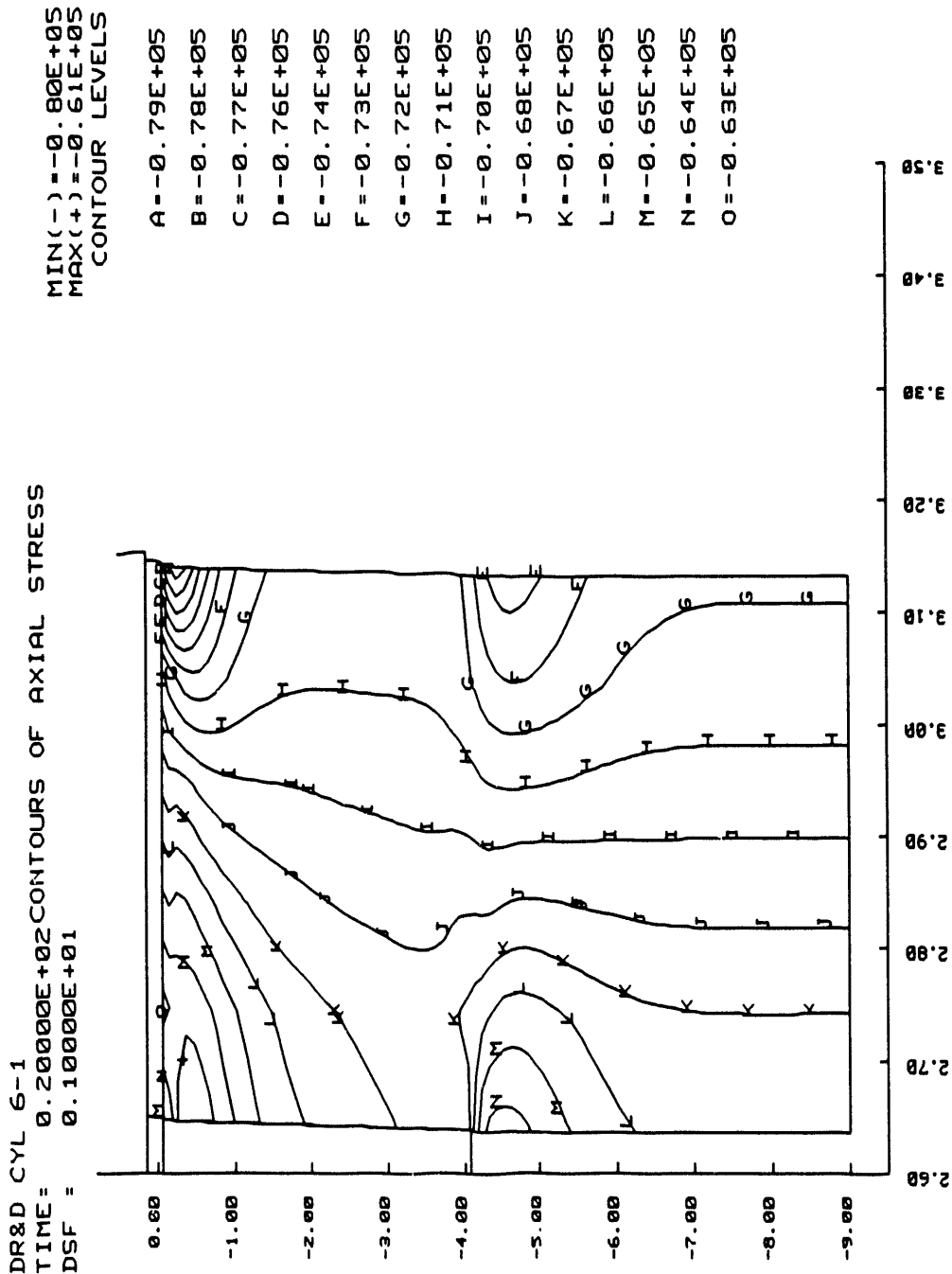
Fig. i.3.1-7. Contours of axial stress.
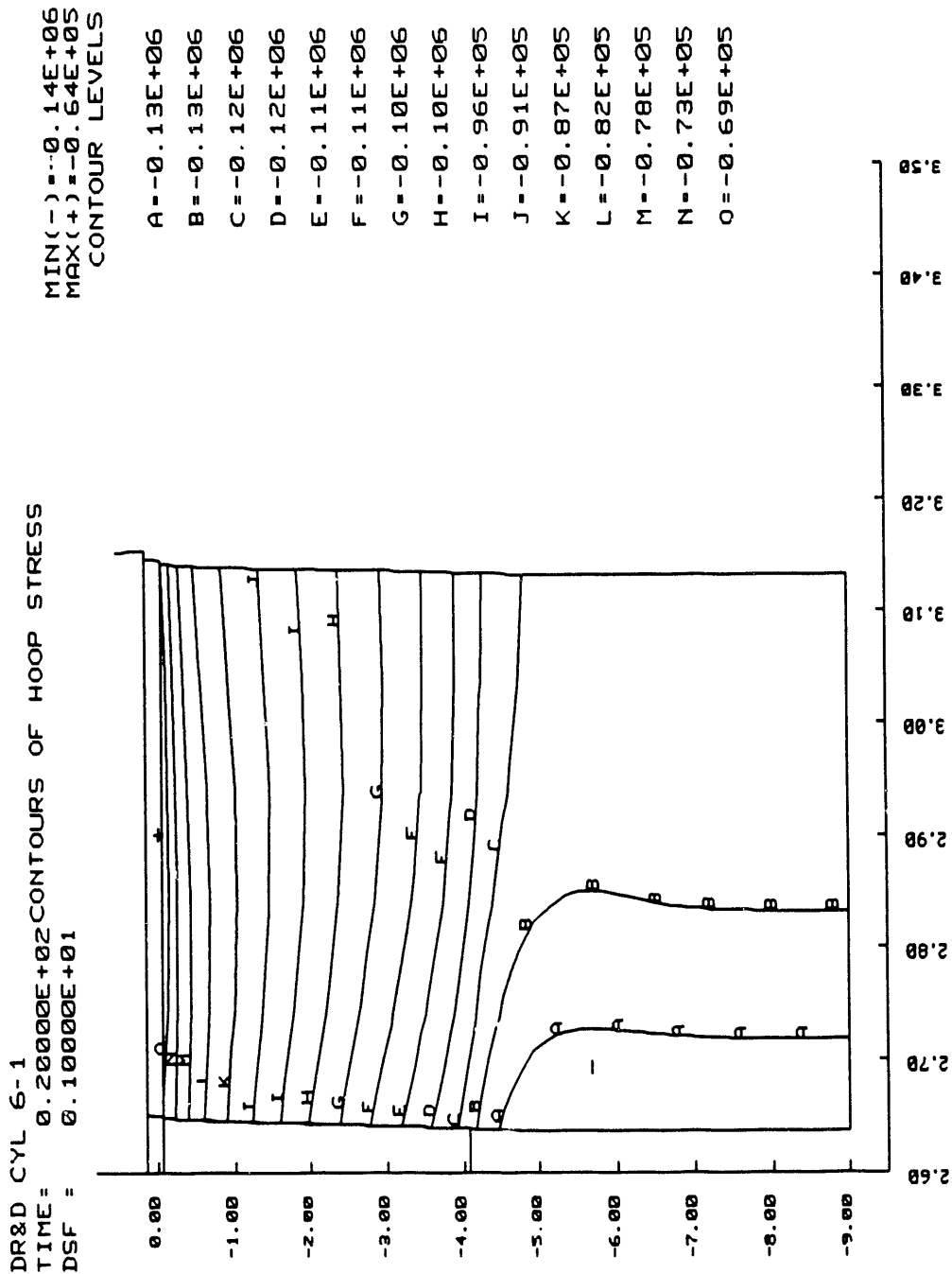
Fig. 1.3.1-8. Contours of hoop stress.

62
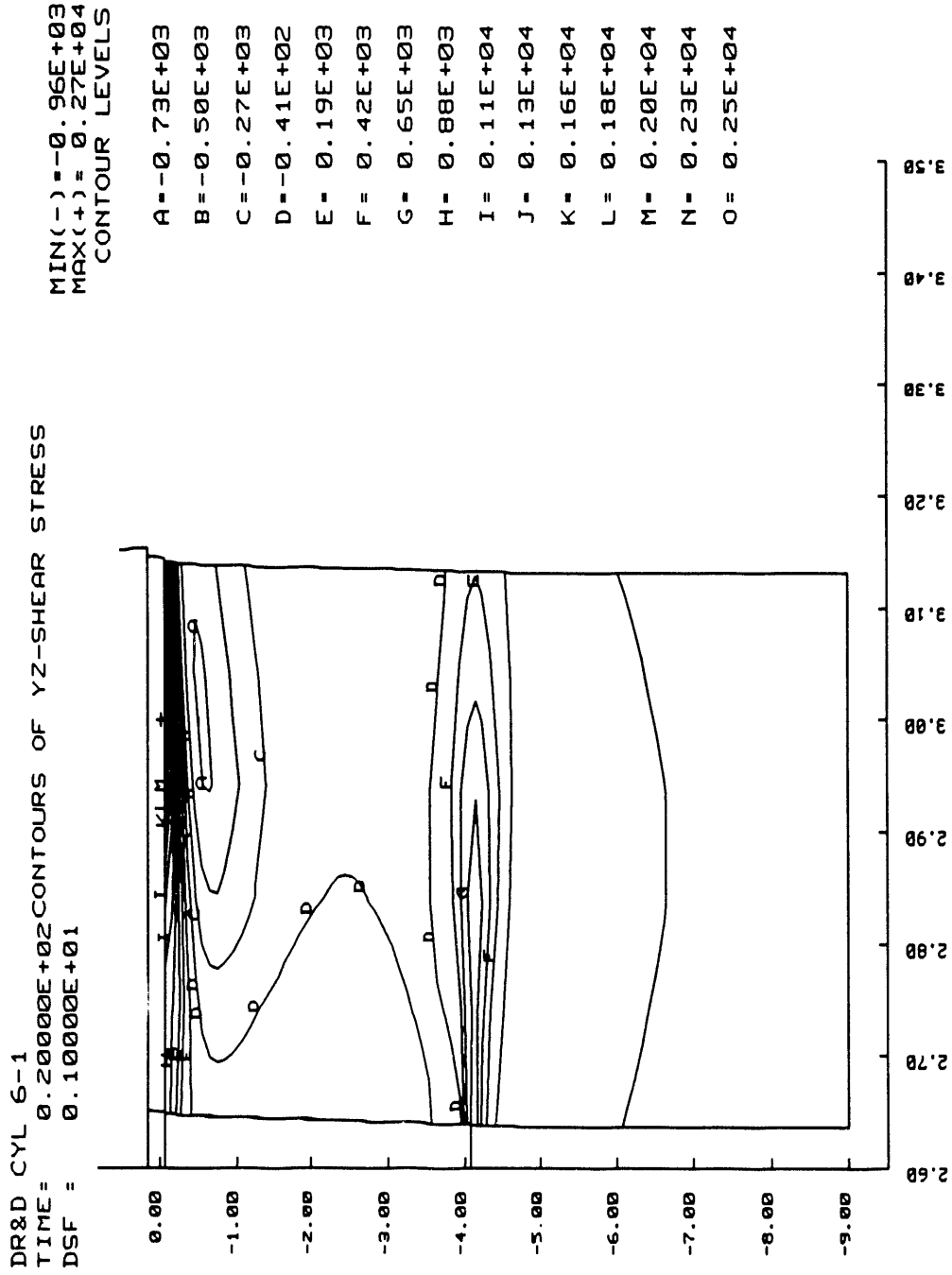
Fig. 1.3.1-9. Contours of RZ shear stress.
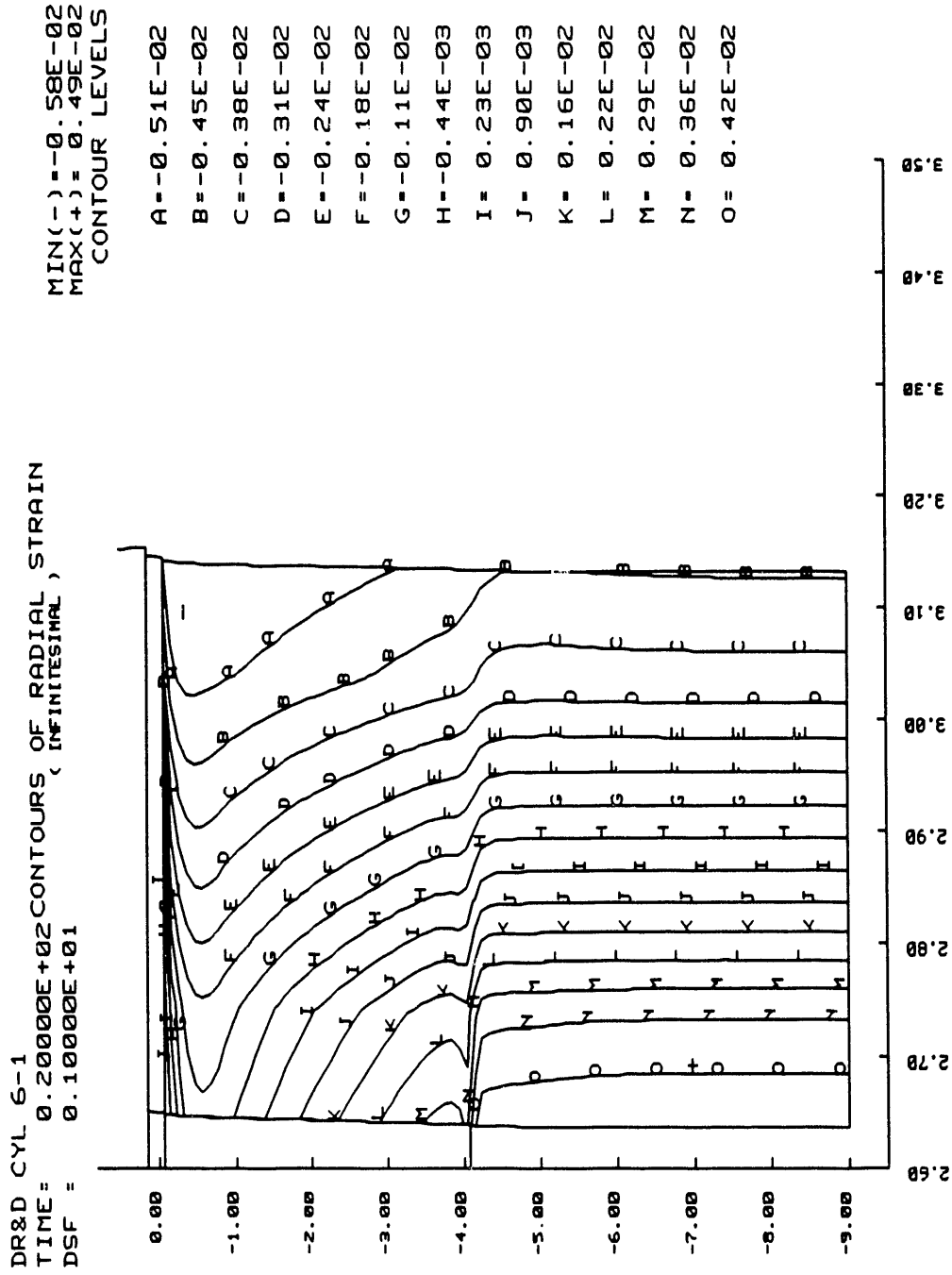
Fig. 1.3.1-10. Contours of radial strain.
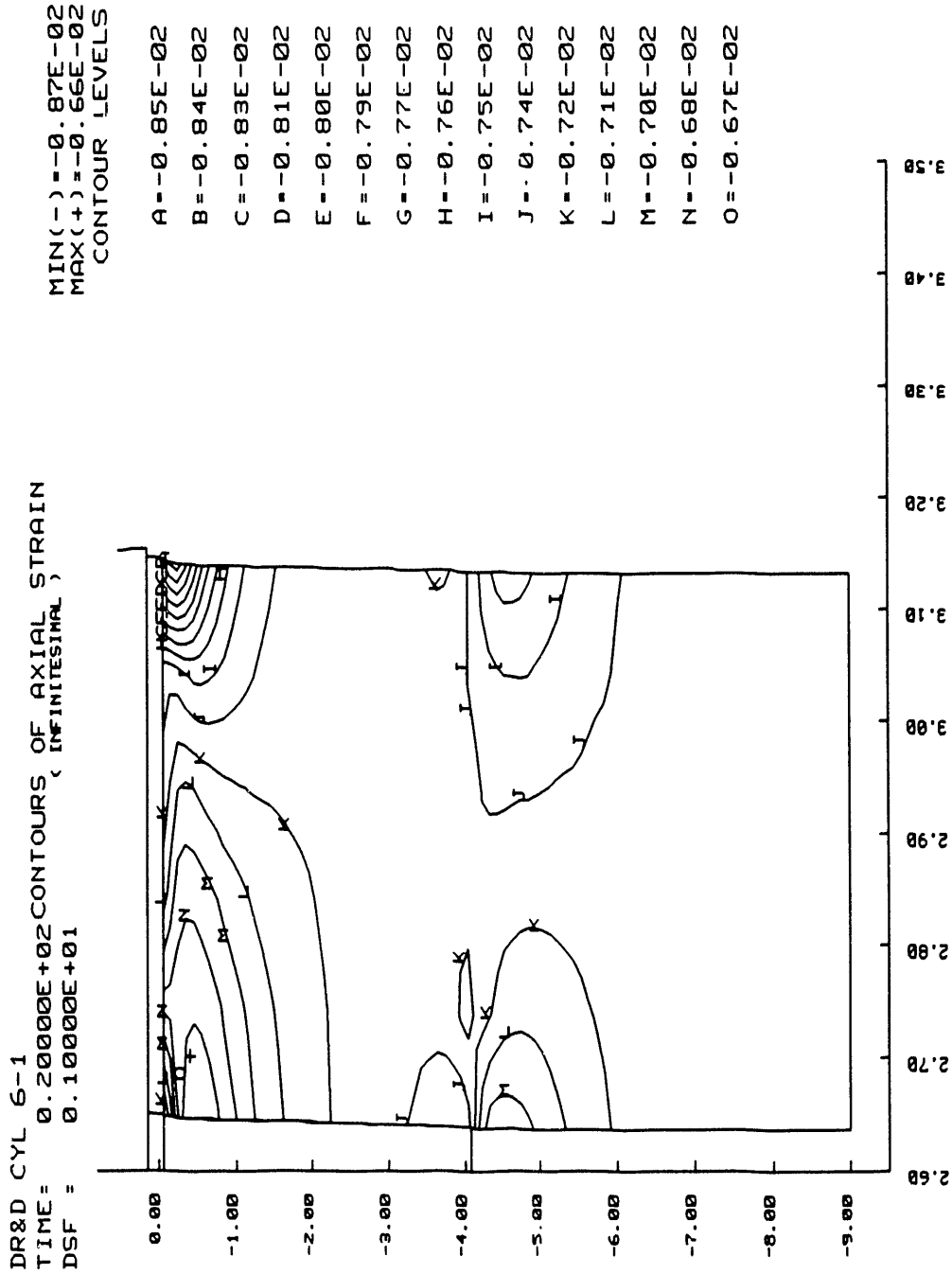
Fig. 1.3.1-11. Contours of axial strain.

65
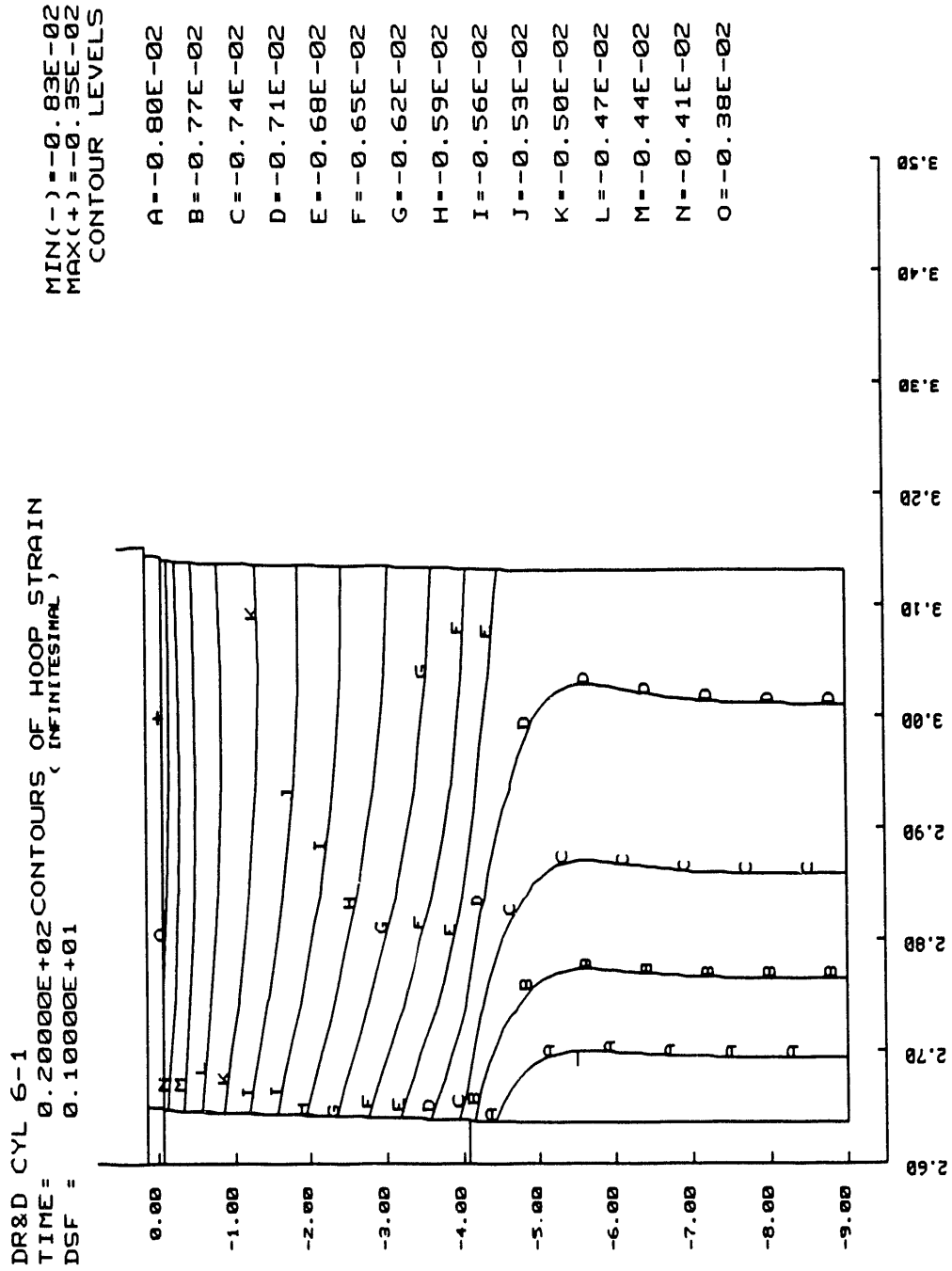
Fig. 1.3.1-12. Contours of hoop strain.
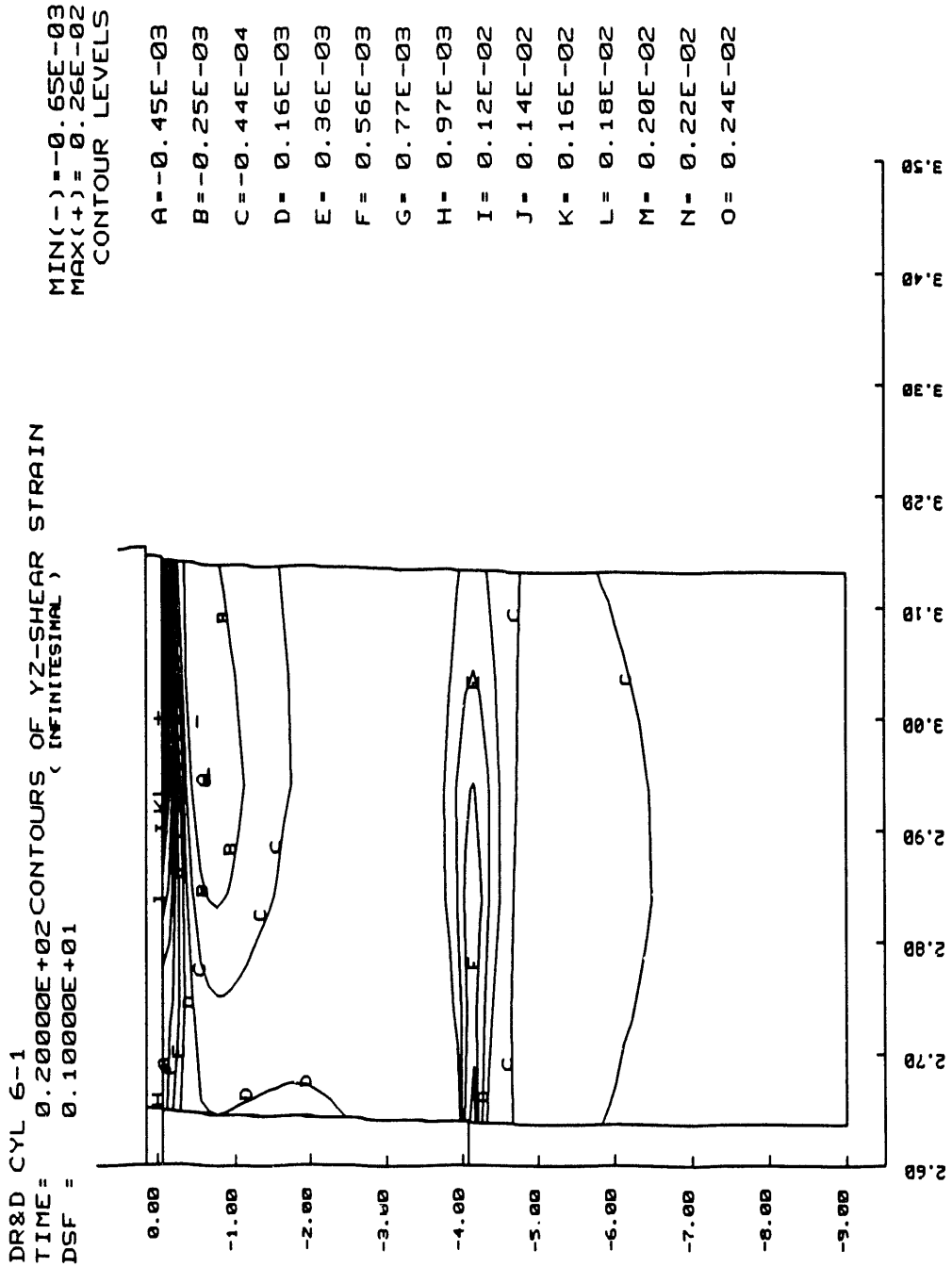
Fig. 1.3.1-13. Contours of RZ shear strain.
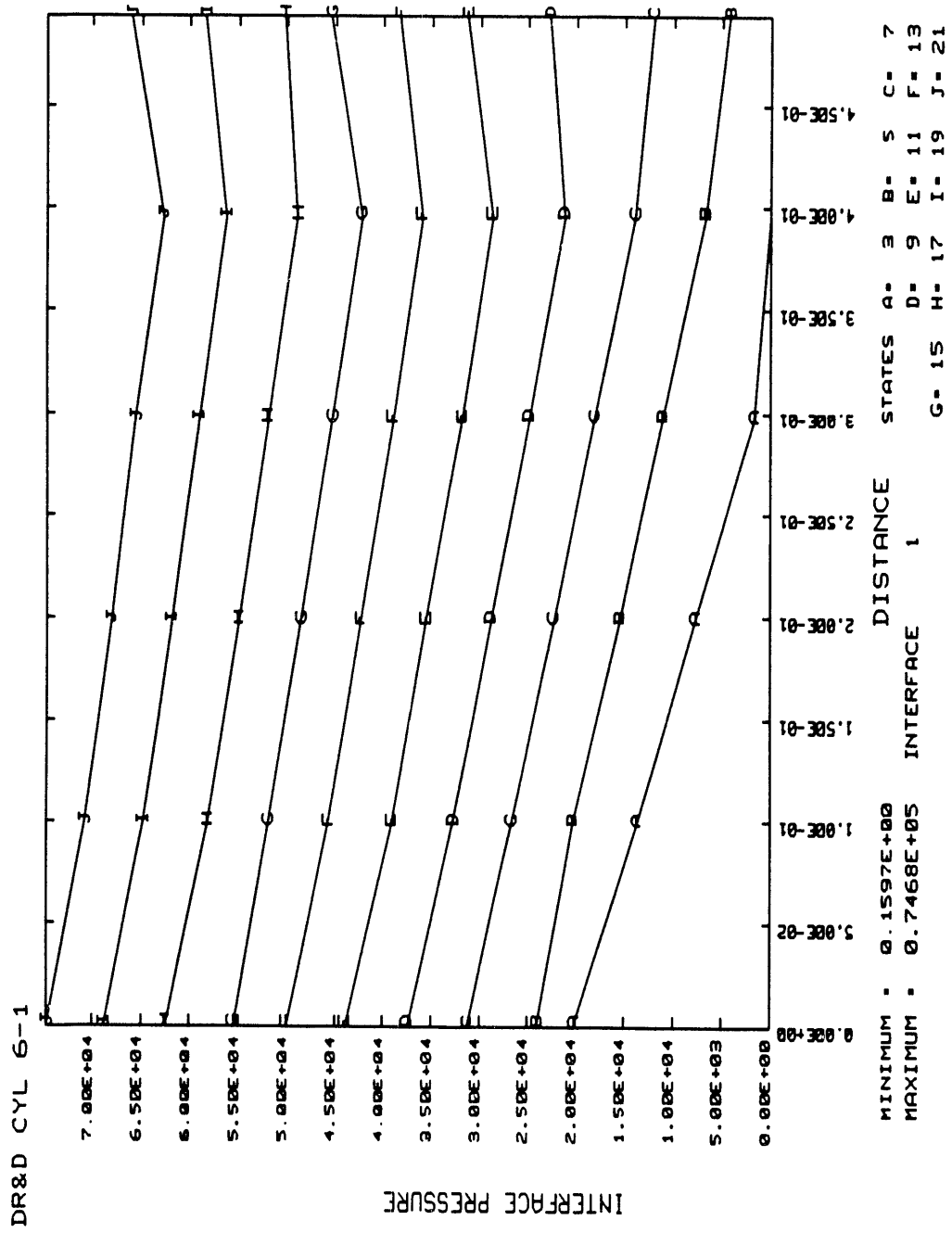
Fig. 1.3.1-14. Pressure profile history on cylinder end surface.
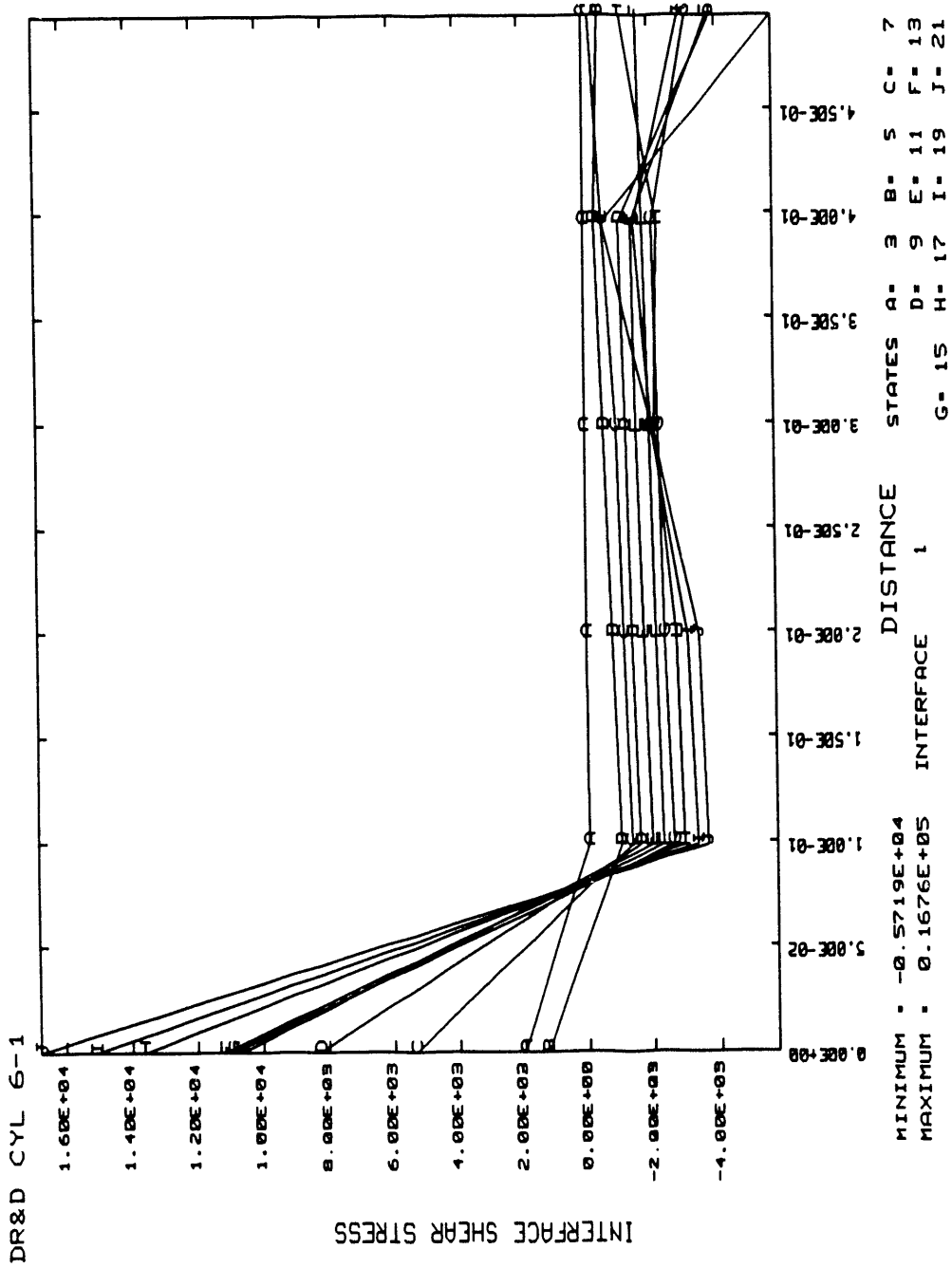
Fig. 1.3.1-15. Shear profile history on cylinder end surface.

1.4 FINITE ELEMENT STABILITY ANALYSIS

The FE method is also being applied to the analysis of the buckling of the various test cylinders. As is the case with the stress analysis task, the FE method is used to supplement the analytical solutions. In general, the closed-form solutions are restricted to perfect cylinder geometry, simple boundary conditions, and shell theory assumptions. The effects of actual end constraints, cylinder imperfections, and radial deformations are not included. The FE method has the capabilities for inclusion of these effects, albeit at the expense of large three-dimensional FE models. Of particular interest is the effect of cylinder out-of-roundness and thickness variation on the elastic stability of thick-section composite cylinders. The influence of the end closures on buckling is also of interest.

Initial activities have concentrated on the evaluation of several FE codes for application to the buckling analysis of rings and cylinders. These codes are NIKE2D, NIKE3D, ADINA, and NISA. Sample problems were formulated to evaluate each code and to obtain results for comparison with the analytic solutions. These evaluations included linear and nonlinear analysis methods. Deficiencies were identified for the NIKE codes and for NISA. Additional analyses are planned for ADINA, and the ABAQUS code will be evaluated.

Results, to date, indicate that the incremental nonlinear analysis approach using either NISA or the NIKE codes gives variable results for the predicted buckling pressure. Results for perfect cylinders are unreliable. During the incremental loading, the solution can continue to converge at pressures higher than the classical bifurcation buckling pressure and beyond the point of singularity of the tangent stiffness matrix. Results are dependent on convergence tolerances for the incremental solution. When defects such as out-of-roundness are included, critical pressures are sensitive to defect level and type of defect. In this case results are useful only if the defect represents an actual condition for the particular test cylinder. Also, results obtained with NISA with the linearized buckling option were not in good agreement with analytical results. Buckling pressure for a ring sample problem was typically 25% higher than the analytical value. As yet, this difference is unexplained. Results with NISA also show extreme sensitivity to the geometric accuracy of the FE mesh. These effects are currently still being evaluated.

1.5 FAILURE ANALYSIS

Theories for compression failure of composite laminates will be acquired and/or developed. These will include microbuckling and fiber kinking modes of failure and other modes such as delamination and fiber compressive failure. These theories will be applied at the ply level by using lamina principal stresses derived from the analytic and FE solutions. Consideration for prebuckling deformations will be made in the failure prediction. Edge stresses will also be considered.

1.5.1 Criteria

The closed-form analytic solutions previously discussed were used to calculate the ply-level stress distributions in a composite cylinder subjected to hydrostatic pressure. The stresses in the cylindrical coordinate system were rotated to the lamina principal material directions and failure theories were applied at the ply level. In the program CCAP, first-ply

failure was predicted based on Hashin's[17] criteria and the Tsai-Wu[12] criterion. Hashin's three-dimensional failure criteria for unidirectional fiber composites was applied to each ply in a laminated cylinder. These criteria not only determined the critical pressure for first-ply failure but also the failure mode. The four distinct failure modes considered are tensile fiber mode, tensile matrix mode, compressive fiber mode, and compressive matrix mode. Each mode is modeled separately, and the criteria are formulated in terms of quadratic stress polynomials, which results in a piecewise smooth failure surface. First-ply failure is determined by the minimum value of a stress ratio, R, defined to be

$$\{\sigma\}_{MAX} = R\{\sigma\}_{APPLIED} \quad . \tag{1.5.1-1}$$

For an applied unit pressure, the magnitude of R determines the critical pressure and the location of the minimum value defines the first ply to fail. For the failure criteria developed by Hashin,[17] the stress ratio for each mode and mechanical loading only are as follows. In the case of a tensile fiber mode, $\sigma_{11} > 0$,

$$R = \cfrac{1}{\sqrt{\left(\cfrac{\sigma_{11}}{\sigma_A^+}\right) + \left(\cfrac{\sigma_{12}}{\tau_A}\right)}} \quad , \tag{1.5.1-2}$$

where σ_{11} and σ_{12} are principal stresses, σ_A^+ is the axial tensile strength, and τ_A is the axial shear strength of the layer. Note here that the strengths are entered as absolute values and the stress components are entered with the appropriate algebraic sign for tension or compression. For the compressive fiber mode, $\sigma_{11} < 0$,

$$R = -\frac{\sigma_A^-}{\sigma_{11}} \quad , \tag{1.5.1-3}$$

where σ_A^- is the axial compressive strength. The allowable axial compressive strength for each layer may be based on a microbuckling or kink band model. For the tensile matrix mode, $\sigma_{22} + \sigma_{33} > 0$,

$$R = \cfrac{1}{\sqrt{\left(\cfrac{\sigma_{22} + \sigma_{33}}{\sigma_T^+}\right)^2 - \cfrac{\sigma_{22}\sigma_{33}}{\tau_T^2} + \left(\cfrac{\sigma_{12}}{\tau_A}\right)^2}} \quad , \tag{1.5.1-4}$$

where σ_{22} and σ_{33} are principal stresses, σ_T^+ is the transverse tensile strength, and τ_T is the transverse shear strength. For the compressive matrix mode, $\sigma_{22} + \sigma_{33} < 0$,

$$R = -\frac{b}{2a} + \sqrt{\left(\frac{b}{2a}\right)^2 + \frac{1}{a}} \quad , \tag{1.5.1-5}$$

where

$$a = \left(\frac{\sigma_{22} + \sigma_{33}}{2\tau_T}\right)^2 - \frac{\sigma_{22}\sigma_{33}}{\tau_T^2} + \left(\frac{\sigma_{12}}{\tau_A}\right)^2 \quad , \tag{1.5.1-6}$$

$$b = \left(\frac{\sigma_{22} + \sigma_{33}}{\sigma_T^-}\right)\left[\left(\frac{\sigma_T^-}{2S_T}\right)^2 - 1\right] \quad , \tag{1.5.1-7}$$

and σ_T^- is the transverse compressive strength. The Tsai-Wu criterion used in the program, CCAP, was also implemented by Roy in his program, CYLIN, and in the program, CYLAN. This is a three-dimensional quadratic stress interaction criterion which, expressed in tensor notation, can be written as

$$F_i\sigma_i + F_{ij}\sigma_i\sigma_j = 1 \quad , \tag{1.5.1-8}$$

where $i = 1,2,...,6$. For this criterion to be independent of the sign of the shear stress and for a generalized plane deformation axisymmetric analysis, Eq. (1.5.1-8) becomes

$$F_{11}\sigma_1^2 + F_{22}\left(\sigma_2^2 + \sigma_3^2\right) + F_{66}\tau_{12}^2 + 2F_{12}\sigma_1\left(\sigma_2 + \sigma_3\right)$$
$$+ 2F_{23}\sigma_2\sigma_3 + F_1\sigma_1 + F_2\left(\sigma_2 + \sigma_3\right) = 1 \quad , \tag{1.5.1-9}$$

where the F_{ij} and F_i strength parameters are given in Eq. (1.5.1-10). The expression for the stress ratio R is the same as Eq. (1.5.1-5) but with the expressions for a and b being given in Eqs. (1.5.1-11) and (1.5.1-12), respectively. Roy also predicted first-ply failure based on a two-dimensional stress state (thin wall solution) and Tsai-Wu's criterion. In this case, Eq. (1.5.1-9) is used with σ_3 set equal to zero.

$$F_{11} = \frac{1}{\sigma_A^+\sigma_A^-} \quad , \qquad F_{22} = \frac{1}{\sigma_T^+\sigma_T^-} \quad , \qquad F_{66} = \frac{1}{S_A^2} \quad ,$$

$$F_{12} = -\frac{1}{2}\sqrt{F_{11}F_{22}} \quad , \qquad F_{23} = -\frac{1}{2}F_{22} \quad , \tag{1.5.1-10}$$

$$F_1 = \frac{1}{\sigma_A^+} - \frac{1}{\sigma_A^-} \quad , \qquad F_2 = \frac{1}{\sigma_T^+} - \frac{1}{\sigma_T^-} \quad ,$$

$$a = F_{11}\sigma_1^2 + F_{22}\left(\sigma_2^2 + \sigma_3^2\right) + F_{66}\tau_{12}^2 + 2\left[F_{12}\sigma_1\left(\sigma_2 + \sigma_3\right) + F_{23}\sigma_2\sigma_3\right] \quad , \tag{1.5.1-11}$$

$$b = F_1\sigma_1 + F_2\left(\sigma_2 + \sigma_3\right) \quad . \tag{1.5.1-12}$$

1.5.2 Failure Analysis Results

A sensitivity analysis was performed with the failure criteria described in the previous section by using three different allowables for the transverse compressive strength, 10, 15, and 20 ksi. The remaining strength parameters used are as follows:

$$\sigma_A^+ = 500 \text{ ksi} \qquad \sigma_A^- = 250 \text{ ksi}$$
$$\sigma_T^+ = 5 \text{ ksi} \qquad \sigma_T^- = 10,15,20 \text{ ksi}$$
$$\tau_A = 10 \text{ ksi} \qquad \tau_T = 5 \text{ ksi}$$

The results of this sensitivity study for cylinders C6-1, C6-2, and C6-3 are presented in Tables 1.5.2-1 and 1.5.2-2. The results show that, compared to the other criteria, the two-dimensional Tsai-Wu criterion used in CYLIN predicts the largest allowable hydrostatic pressure for all three cylinders and all three transverse compressive strengths, whereas Hashin's criteria predicts the smallest pressures. All criteria predict an increase in the allowable pressure for first-ply failure when the transverse compressive strength is increased. Cylinder C6-1 has a larger allowable pressure than cylinder C6-3, and C6-3 has a larger allowable pressure than C6-2, with one exception (see Table 1.5.2-2).

As stated earlier, the application of Hashin's criteria identifies one of four different failure modes associated with the allowable pressure at first-ply failure. For allowable transverse compressive strengths equal to 10 ksi and 15 ksi, the results indicate a compressive matrix mode of failure. An increase in the allowable transverse compressive strength changes the failure mode to a compressive fiber mode. This change in failure mode occurs for all three cylinders.

The location of the first ply to fail is seen to be a function of the cylinder configuration. For cylinder C6-1, which has a 2:1 ratio of hoop to axial plies, and for a transverse compressive strength equal to 10 ksi, the innermost axial ply is predicted to fail first at $P = 13.404$ ksi. The allowable pressure increases to 20.219 ksi when the transverse compressive strength is 15 ksi and the compressive matrix mode of failure occurs in the innermost hoop ply. Increasing the transverse compressive strength to 20 ksi increases the allowable pressure to 25.720 ksi and the innermost hoop ply fails in a compressive fiber mode. The first ply to fail in the 1:1 cylinder, i.e., C6-3, was the innermost axial ply for transverse compressive strengths equal to 10 ksi and 15 ksi. The failure mode changes from a compressive matrix mode to a fiber mode and the location of the first-ply failure changes to the innermost hoop ply when the transverse compressive strength is increased to 20 ksi. Cylinder C6-2 had three times as many hoop layers as axial layers and the first-ply failure was located in the innermost hoop ply for transverse compressive strengths equal to 10 ksi and 15 ksi. When a transverse compressive strength was specified to be 20 ksi, the outermost axial ply was predicted to fail first in a compressive fiber mode.

Table 1.5.2-1. Cylinder first-ply failure analysis

Cylinder	Failure criteria	Y_c^a = 10 ksi		Y_c^a= 15 ksi		Y_c^a = 20 ksi	
		Layer	p_{cr} (ksi)	Layer	p_{cr} (ksi)	Layer	p_{cr} (ksi)
C6-1	Hashin	3[b]	13.404	1[b]	20.219	1[c]	25.720
	Tsai-Wu	1	14.134	1	21.830	1	29.733
	Roy(3-D)	1	14.200	1	21.933	1	29.880
	Roy(2-D)	3	15.097	3	23.315	3	31.807
	CYLAN	1	13.644	1	21.090	1	28.785
C6-2	Hashin	1[b]	11.407	1[b]	17.110	27[c]	22.381
	Tsai-Wu	1	11.930	1	18.411	1	25.117
	Roy(3-D)	1	11.989	1	18.498	1	25.234
	Roy(2-D)	1	13.322	1	20.550	1	28.031
	CYLAN	1	11.407	1	17.637	1	23.976
C6-3	Hashin	3[b]	11.834	3[b]	18.775	1[c]	21.003
	Tsai-Wu	3	12.375	1	19.433	3	26.816
	Roy(3-D)	3	12.454	3	19.559	3	26.993
	Roy(2-D)	3	13.485	3	20.695	3	28.138
	CYLAN	3	12.4.0	3	19.142	3	26.010

[a] Transverse compressive strength
[b] Compressive matrix mode
[c] Compressive fiber mode

Notes:

Layer no. 1 = innermost hoop ply
Layer no. 3 = innermost axial ply
Layer no. 27 = outermost axial ply

Roy(3-D) - Thick wall solution
Roy(2-D) - Thin wall solution

Table 1.5.2-2. Percent difference in predicted failure pressures

Criteria	$\sigma_T = 10$ ksi		$\sigma_T = 15$ ksi		$\sigma_T = 20$ ksi	
	$P_2{}^a < P_3{}^b$	$P_3 < P_1{}^c$	$P_2 < P_3$	$P_3 < P_1$	$P_2 < P_3$	$P_3 < P_1$
Hashin	3.61	11.71	8.87	7.14	-6.56	18.34
Tsai-Wu	3.60	12.44	5.26	10.98	6.33	9.81

^{a} Predicted failure pressure for cylinder C6-2
^{b} Predicted failure pressure for cylinder C6-3
^{c} Predicted failure pressure for cylinder C6-1

1.5.3 Experimental Correlation

The capabilities of the analytical tools developed for this project were demonstrated in Sects. 1.1, 1.2, and 1.5. In addition to these analytical capabilities, the development of a performance model requires the design and testing of test articles. The 2:1 hoop to axial ply ratio cylinder was designed and fabricated as described in Sect. 2. The cylinder was then hydrostatically pressure tested up to 20 ksi without failure occurring. The testing procedure and experimental results are discussed in detail in Sect. 3. From the results of the failure analysis, the cylinder test pressure of 20 ksi is seen to be consistent with the range of predicted failure pressures. Also, it is interesting that for the C6-1 cylinder configuration the analytic predictions for strength and buckling failures are comparable.

For the test pressure of 20 ksi, the maximum hoop stress and axial stress are 194 ksi and 178 ksi, respectively. These are the highest reported values achieved, to date, in a graphite composite cylinder. The peak hoop and axial strains are 0.84% and 0.73%, respectively. The theoretical predictions from CCAP for the interior hoop strains at the cylinder midbay are compared with the experimental results in Fig. 1.5.3-1. The predicted strains are seen to be in excellent agreement with two of the three strain gages. The average value of the three midbay interior gages at a pressure of 19 ksi is equal to 0.83%, which is slightly larger than the calculated strain of 0.80%. The comparison between theory and experiment for the midbay exterior hoop strains is presented in Fig. 1.5.3-2. The average measured strains are again seen to be slightly larger than the theoretical strains, with the agreement between the two being acceptable. Figs. 1.5.3-3 and 1.5.3-4 illustrate the correlation between theory and experiment for the midbay interior and exterior axial strains, respectively. The theoretical results for the axial strains slightly overpredict the measured results but are considered to be in satisfactory agreement with each other.

The correlation of predicted ply-level stresses and implementation of a specific failure criteria associated with an observed damage mode is an important step in developing performance models. However, this phase of the experimental correlation was not performed for cylinder C6-1 because of the record 20-ksi pressure achieved without failure with no observed damage.

Cylinder C6−1
Midbay Interior Hoop Strains
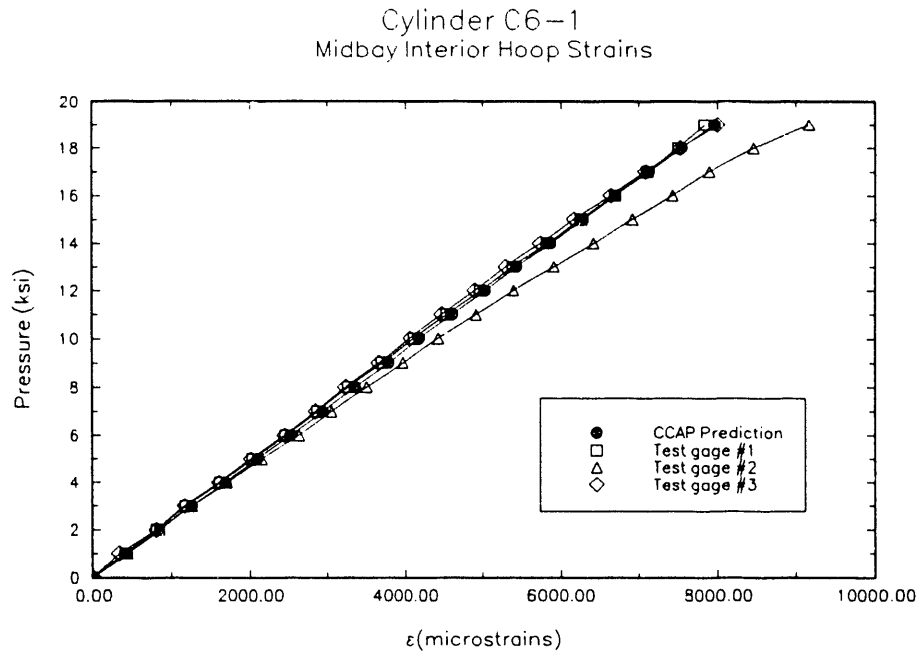
Fig. 1.5.3-1. Theoretical and experimental comparison for the midbay interior hoop strains.

Cylinder C6−1
Midbay Exterior Hoop Strains
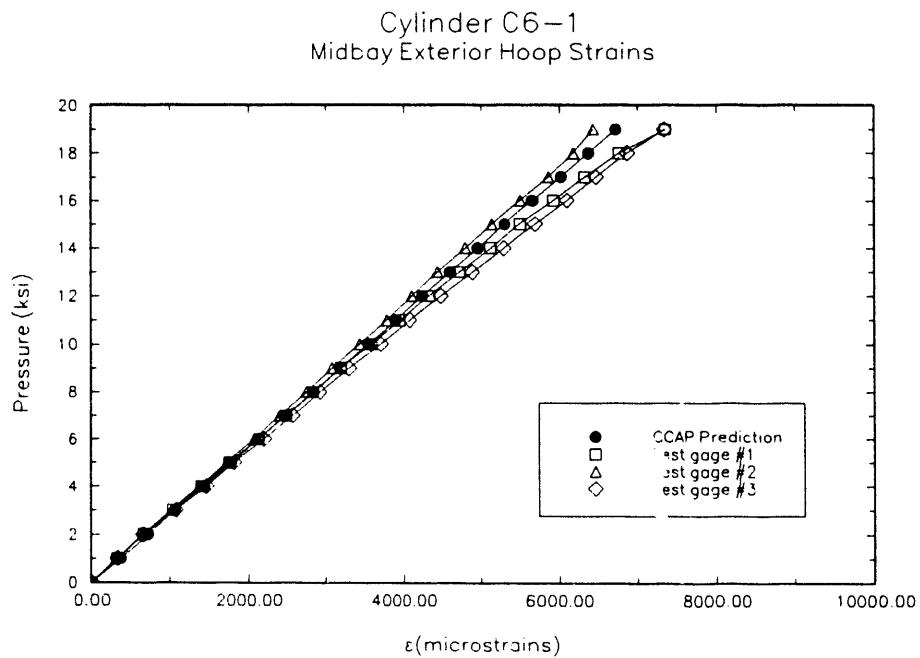
Fig. 1.5.3-2. Theoretical and experimental comparison for the midbay exterior hoop strains.

Cylinder C6−1
Midbay Interior Axial Strains
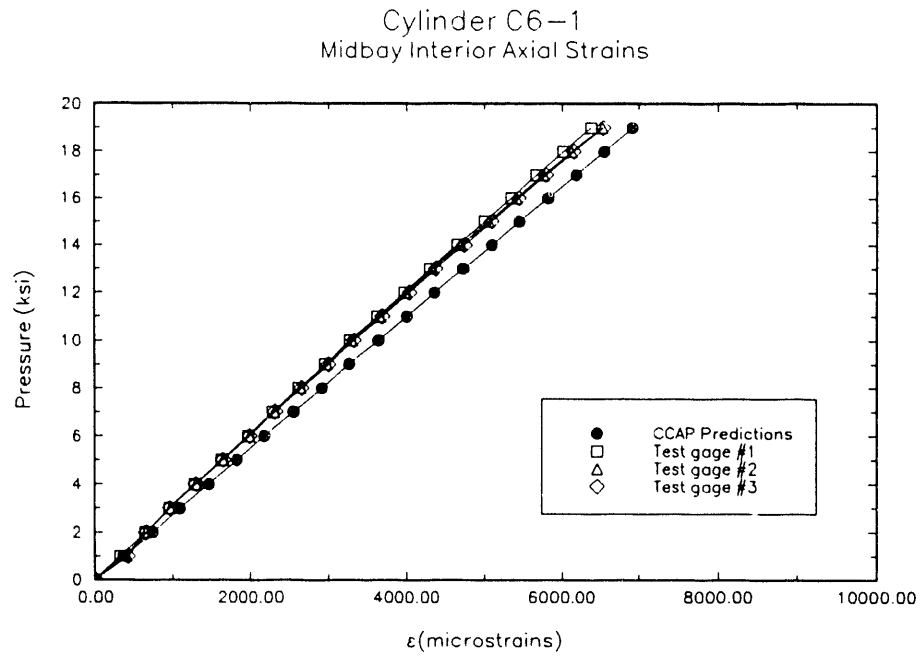
Fig. 1.5.3-3. Theoretical and experimental comparison for the midbay interior axial strains.

Cylinder C6−1
Midbay Exterior Axial Strains
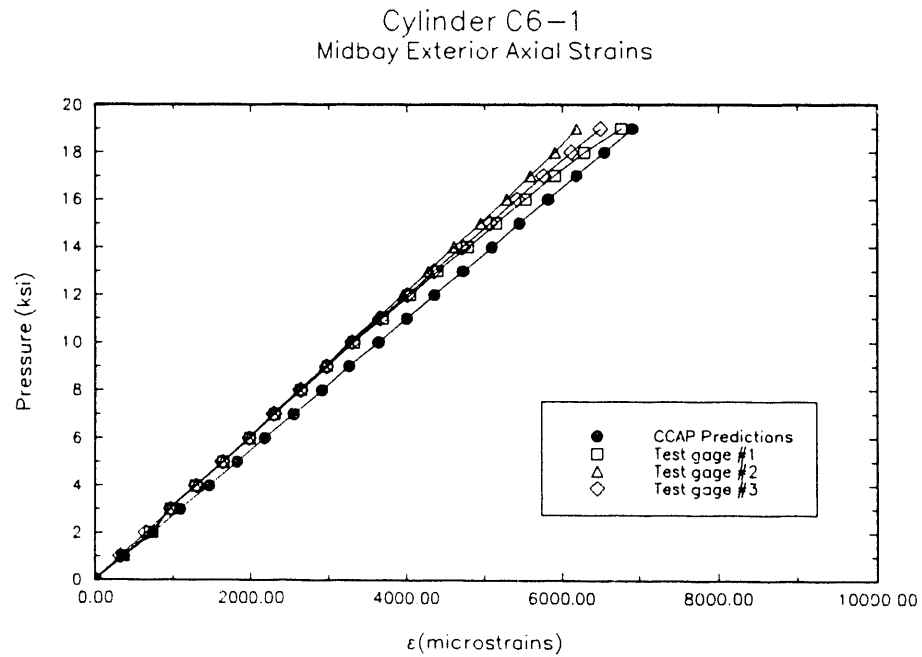
Fig. 1.5.3-4. Theoretical and experimental comparison for the midbay exterior axial strains.

2. TEST ARTICLE DEVELOPMENT/FABRICATION

The objective of this task is to develop the requisite fabrication technology for making test articles in a controlled, reproducible manner and to supply the test articles for the project. This also includes the software programs for control of the filament winding machine.

The task deliverables are the demonstration test articles made to design specifications by a controlled process. This also includes the laboratory tests and inspections to verify the composition and final dimensions of the cylinders.

2.1 TEST ARTICLE TOOLING DESIGN/FABRICATION

This task involves the design and fabrication of tooling for the fabrication of thick-section composite cylinders by the wet filament winding process. This includes the auxiliary equipment for the winding machine including the winding mandrels and compaction equipment. The efforts in this task are aimed at the optimization of the winding process including fiber placement, compaction, and composite cure. Particular emphasis will be given to the development of process improvements to reduce layer thickness variation and waviness and to improve fiber compaction.

2.2 TEST ARTICLE FABRICATION

During the first year of the project, three cylinder designs were fabricated. These designs are described in detail in Sect. 3.1. Fabrication details are discussed in this section.

The first of these cylinders (designated as C6-1) was a nominal 0°/90° 1:2 lay-up similar to previous cylinders fabricated for the Naval Ocean Systems Center[5] and the David Taylor Research Center.[3] Prior to fabricating this first cylinder, refinements were made to the winding program to improve uniformity of the axial layers. Otherwise, this 1:2 lay-up was similar to other graphite cylinders made in other programs.

The lay-ups for the other two cylinders (C6-2 and C6-3) were a significant departure from the previous fabrication experience in the Applied Technology Division of ORNL. These cylinders were first-of-a-kind and, therefore, required that new winding programs be developed. Because of schedule and cost considerations, no trial fabrications of these lay-ups were done before the cylinder fabrications.

Cylinder C6-1 was fabricated successfully on the first attempt. This cylinder achieved record performance in hydrotest. The other two cylinders were also successfully fabricated but were not tested because of delaminations that occurred after fabrication. Cylinder C6-2 (0°/90° 1:3) delaminated during initial cylinder cutoff. Cylinder C6-3 (0°/90° 1:1) delaminated during ring specimen cutoff. These cylinders apparently had significant residual fabrication stresses which precipitated the delaminations. The rough-cut cylinders were ultrasonically inspected to determine the extent of the delaminations within the test cylinder gage length. The results indicated areas of delamination in both cylinders. The delaminations were also visible at each end of each cylinder after final machining. Further investigation of this problem was beyond the scope of the present investigation. Additional studies should be conducted in the future to determine the cause of the residual stresses if these lay-ups are fabricated again.

Cylinders C6-1, C6-2, and C6-3 were wet wound on an aluminum mandrel by using a four-axis computer controlled winding machine. A combination comb and roller feedeye was used to maintain fiber placement during axial and hoop fabrication. Sprocket-shaped "pin-rings" were attached to each end of the mandrel to maintain placement of the axial strands. Winding pattern band advance for the axial layers was chosen to maximize coverage for the increasing part diameter. Axial layer band advance calculations for the cylinders are listed in Tables 2.2-1, 2.2-2, and 2.2-3. The lay-up designs were 2:1, 3:1, and 1:1 ratios of hoop oriented fiber (90°) to axially oriented fiber (0°). The specific lay-up configuration for the cylinders were as follows:

Cylinder C6-1	(2 hoops: 1 axial)	$90[90_2/0_2/90_2]_{12}90$
Cylinder C6-2	(3 hoops: 1 axial)	$90[90_3/0_2/90_3]_9 90$
Cylinder C6-3	(1 hoop: 1 axial)	$90[90/0_2/90]_{18}90$

The materials of construction for both the axial and hoop layers of all three cylinders were Hercules IM6-G carbon fiber from lot X672-3P, and Union Carbide ERL-2258, a 50/50 blend of diglycidyl ether of bisphenol A and bis (2,3 epoxycyclopentyl) ether. The system was cured with 25 pphr m-phenylenediamine.

The same nominal processing conditions were utilized for all three cylinder designs. The 76-cm-long (30 in.) aluminum mandrel was preheated to 54°C (130°F) prior to fabrication initiation. The resin temperature was maintained between 52°C (125°F) and 57°C (135°F) during impregnation, and heat was applied to the mandrel during the winding operation to promote resin bleed-out. The carbon tows were tensioned at the 5- to 5.5-kg (11- to 12-lb) range during hoop winding and the 2- to 2.5-kg (4- to 5-lb) range during axial winding. The cylinder was fabricated in two stages with a B-staged cure, approximately 54°C (130°F), for a minimum of 16 hours between stages. The incremental B-staged cure was performed at a thickness of approximately 0.75 cm (0.3 in.), which was nominally 6 layers [or 0.10 cm (0.04 in.)] greater than half thickness. After completion of the winding, the part was staged at 54°C (130°F) for 16 hours and then cured in a forced air oven. The part was ramped to 85°C (185°F), held for two hours, ramped to 152°C (305°F), held for four hours, and allowed to cool to ambient overnight. The cylinder was removed from the mandrel by chilling the part and mandrel with liquid nitrogen. The cylinder was sampled for composition and dimensionally inspected.

The compositional data for the three cylinders are listed in Table 2.2-4. As shown in this table, the fiber volume fraction increased as the ratio of the hoops to axials increased (as would be expected); the void level remained a nominal 1.4 percent for all three cylinders.

The target tube dimensions were approximately 13.49 cm (5.31 in.) inside diameter (ID) and nominally 1.27 cm (0.5 in.) thick. The total number of layers for the three cylinders was held constant, and the thickness was allowed to vary so that the layer thickness decrease, resulting from increasing the hoop layer to axial layer ratio, was tolerated. The measured diameters and thicknesses of the three cylinders are shown in Table 2.2-5.

Table 2.2-1. Band advance calculations for cylinder C6-1
design: 2:1 [90/0] IM6/ERL-2258

Layer		Added thickness (in.)	Added diameter (in.)	Part diameter (in.)	Circum. (in.)	Bandwidth advance (degrees)
0	Mandrel			5.310	16.682	
	3 hoops	0.021	0.039	5.349	16.804	7.258
1	2 axials	0.014	0.028	5.377	16.892	
	4 hoops	0.028	0.056	5.433	17.068	7.146
2	2 axials	0.014	0.028	5.461	17.156	
	4 hoops	0.028	0.056	5.517	17.332	7.037
3	2 axials	0.014	0.028	5.545	17.420	
	4 hoops	0.028	0.056	5.601	17.596	6.932
4	2 axials	0.014	0.028	5.629	17.684	
	4 hoops	0.028	0.056	5.685	17.860	6.829
5	2 axials	0.014	0.028	5.713	17.948	
	4 hoops	0.028	0.056	5.769	18.124	6.730
6	2 axials	0.014	0.028	5.797	18.212	
	4 hoops	0.028	0.056	5.853	18.388	6.633
7	2 axials	0.014	0.028	5.881	18.476	
	4 hoops	0.028	0.056	5.937	18.652	6.539
8	2 axials	0.014	0.028	5.965	18.740	
	4 hoops	0.028	0.056	6.021	18.916	6.448
9	2 axials	0.014	0.028	6.049	19.003	
	4 hoops	0.028	0.056	6.105	19.179	6.359
10	2 axials	0.014	0.028	6.133	19.267	
	4 hoops	0.028	0.056	6.189	19.443	6.273
11	2 axials	0.014	0.028	6.217	19.531	
	4 hoops	0.028	0.056	6.273	19.707	6.189
12	2 axials	0.014	0.028	6.301	19.795	
	3 hoops	0.021	0.042	6.343	19.927	

Table 2.2-2. Band advance calculations for cylinder C6-2
design: 3:1 [90/0] IM6/ERL-2258

	Layer	Added thickness (in.)	Added diameter (in.)	Part diameter (in.)	Circum. (in.)	Bandwidth advance (degrees)
0	Mandrel			5.310	16.682	
	4 hoops	0.028	0.056	5.366	16.858	7.261
1	2 axials	0.014	0.028	5.394	16.946	
	6 hoops	0.042	0.084	5.478	17.210	7.112
2	2 axials	0.014	0.028	5.506	17.298	
	6 hoops	0.042	0.084	5.590	17.562	6.970
3	2 axials	0.014	0.028	5.618	17.649	
	6 hoops	0.042	0.084	5.702	17.913	6.833
4	2 axials	0.014	0.028	5.730	18.001	
	6 hoops	0.042	0.084	5.814	18.265	6.701
5	2 axials	0.014	0.028	5.842	18.353	
	6 hoops	0.042	0.084	5.926	18.617	6.575
6	2 axials	0.014	0.028	5.954	18.705	
	6 hoops	0.042	0.084	6.038	18.969	6.453
7	2 axials	0.014	0.028	6.066	19.057	
	6 hoops	0.042	0.084	6.150	19.321	6.335
8	2 axials	0.014	0.028	6.178	19.409	
	6 hoops	0.042	0.084	6.262	19.673	6.222
9	2 axials	0.014	0.028	6.290	19.761	
	4 hoops	0.028	0.056	6.346	19.937	

Table 2.2-3. Band advance calculations for cylinder C6-3
design: 1:1 [90/0] IM6/ERL-2258

Layer		Added thickness (in.)	Added diameter (in.)	Part diameter (in.)	Circum. (in.)	Bandwidth advance (degrees)
0	Mandrel			5.310	16.682	
	2 hoops	0.014	0.028	5.338	16.770	7.299
1	2 axials	0.014	0.028	5.366	16.858	
	2 hoops	0.014	0.028	5.394	16.946	7.223
2	2 axials	0.014	0.028	5.422	17.034	
	2 hoops	0.014	0.028	5.450	17.122	7.149
3	2 axials	0.014	0.028	5.478	17.210	
	2 hoops	0.014	0.028	5.506	17.298	7.076
4	2 axials	0.014	0.028	5.534	17.386	
	2 hoops	0.014	0.028	5.562	17.474	7.005
5	2 axials	0.014	0.028	5.590	17.562	
	2 hoops	0.014	0.028	5.618	17.649	6.935
6	2 axials	0.014	0.028	5.646	17.737	
	2 hoops	0.014	0.028	5.674	17.825	6.867
7	2 axials	0.014	0.028	5.702	17.913	
	2 hoops	0.014	0.028	5.730	18.001	6.799
8	2 axials	0.014	0.028	5.758	18.089	
	2 hoops	0.014	0.028	5.786	18.177	6.734
9	2 axials	0.014	0.028	5.814	18.265	
	2 hoops	0.014	0.028	5.842	18.353	6.669
10	2 axials	0.014	0.028	5.870	18.441	
	2 hoops	0.014	0.028	5.898	18.529	6.606
11	2 axials	0.014	0.028	5.926	18.617	
	2 hoops	0.014	0.028	5.954	18.705	6.544
12	2 axials	0.014	0.028	5.982	18.793	
	2 hoops	0.014	0.028	6.010	18.881	6.483
13	2 axials	0.014	0.028	6.038	18.969	
	2 hoops	0.014	0.028	6.066	19.057	6.423
14	2 axials	0.014	0.028	6.094	19.145	
	2 hoops	0.014	0.028	6.122	19.233	6.364
15	2 axials	0.014	0.028	6.150	19.321	
	2 hoops	0.014	0.028	6.178	19.409	6.306
16	2 axials	0.014	0.028	6.206	19.497	
	2 hoops	0.014	0.028	6.234	19.585	6.250
17	2 axials	0.014	0.028	6.262	19.673	
	2 hoops	0.014	0.028	6.290	19.761	6.194
18	2 hoops	0.014	0.028	6.318	19.849	
	2 hoops	0.014	0.028	6.346	19.937	

Table 2.2-4. Compositional data for compression cylinders C6-1, C6-2, and C6-3

Cylinder	Density (gm/cm^3)	Volume fiber (%)	Volume resin (%)	Volume void (%)
C6-1	1.5750	68.28	30.33	1.39
C6-2	1.5765	68.58	30.00	1.42
C6-3	1.5629	65.82	32.82	1.37

Table 2.2-5. Average dimensions for compression cylinders C6-1, C6-2, and C6-3

Cylinder	Inside diameter [cm (in.)]	Outside diameter [cm (in.)]	Thickness [cm (in.)]
C6-1	13.506 (5.318)	16.025 (6.308)	1.260 (0.495)
C6-2	13.501 (5.315)	15.984 (6.293)	1.241 (0.489)
C6-3	13.502 (5.317)	16.158 (6.355)	1.328 (0.519)

3. TEST DEVELOPMENT/DEMONSTRATION

The objective of this task is the development of the test methodology for adequate characterization of composite materials under compression. This includes the development of specific test methods for cylinders and/or rings in addition to specialized test fixtures for performing tests. This also includes the testing of the demonstration articles and the generation of data for evaluation and validation of design codes.

The deliverables under this task include the est methods and fixturing and the test data on the demonstration test articles obtained by a controlled test methodology.

The focus of this task will be the development of test specimens and test fixtures for adequate characterization of composite materials under hydrostatic compression (conventional test approaches are not adequate). This task will also generate useful data on demonstration test articles for evaluation and validation of design codes. Efforts will also be directed at recommending improved test methodology and/or standard test methods for cylinders. Existing American Society for Testing and Materials (ASTM) procedures for pressure testing cylinders and rings are not current.

Prototype test devices will be designed, analyzed, and evaluated experimentally. In selecting test devices, ORNL will be sensitive to current practices and to ASTM requirements for acceptance of new test methods. However, test selection will not be based solely on the criteria of wide acceptance or universality but rather on ability to control parameters which govern a particular mode of failure. Also, different tests will likely be required to completely characterize the different modes of failure in compression.

The activities under this task include the design of the test cylinders and end closures and the hydrostatic testing of the test articles.

3.1 TEST ARTICLE DESIGN

Under this task, the various test articles are designed and drawings for fabrication and machining prepared. The design of each test cylinder includes the specification of the materials and the laminate stacking sequence. The designs are based on the parametric studies conducted under Task 1. Results from stress and buckling analyses are the basis for the selection of material type and specification of material lay-up and the test article dimensions. Each test article is specified in drawing form to the required level of detail to accomplish the fabrication, cutoff, and final machining.

During the first year, three different cylinder designs were completed for the IM6/ERL-2258/MPDA composite system. These cylinders had different ply ratios to explore the effect of this primary variable on performance and mode of failure. These designs were for 0/90 cross-ply layups with ratios of 1:1, 1:2, and 1:3 (axial/hoop). The number of layers and total laminate thickness were held constant in these designs to eliminate size effect from the experimental program. The stacking sequence for each design is given in Sect. 2.2. The selection of the range of ply ratios was based on broad parametric studies that used the performance model. Details of these parametric studies will be published later. The dimensions and smeared elastic constants for these designs are given in Table 3.1-1.

Table 3.1-1. Equivalent smeared properties & geometric parameters
for IM6/ERL-2258 cylinders

Property	Cylinder construction		
	C6-1 (2:1) $90/(90_2/0_2/90_2)_{12}/90$	C6-2 (3:1) $90/(90_3/0_2/90_3)_9/90$	C6-3 (1:1) $90/(90/0_2/90)_{18}/90$
E_x (MSI)	8.3872	6.6630	11.834
E_θ (MSI)	15.852	17.571	12.409
E_r (MSI)	1.6763	1.6666	1.6831
$\nu_{x\theta}$	0.029371	0.026499	0.037518
ν_{xr}	0.38942	0.38683	0.39367
$\nu_{\theta r}$	0.39537	0.39355	0.39420
$G_{x\theta}$ (MSI)	0.85702	0.85702	0.85702
G_{xr} (MSI)	0.64292	0.61723	0.69431
$G_{\theta r}$ (MSI)	0.75425	0.77995	0.70287
I.D. (in.)	5.318	5.315	5.317
O.D. (in.)	6.308	6.293 (6.351 nom.)	6.355
R_i (in.)	2.6590	2.6575	2.6585
R_o (in.)	3.1540	3.1465 (3.1755 nom.)	3.1775
R_m (in.)	2.9065	2.902 (2.9165 nom.)	2.918
h (in.)	0.495	0.489 (0.518 nom.)	0.519
R_m/h	5.8717	5.9346 (5.6303 nom.)	5.6224
$2R_m/L$ (L=10 in.)	1.7203	1.7229	1.7135
$D_{\theta\theta}$ (psi)	164300	174400	151200
layer t (in.)	0.006689	0.006608 (0.007 nom.)	0.007013

3.2 TEST FIXTURE DESIGN/FABRICATION

This task consists of the design activities related to the test fixturing for the various test articles. Activities include the development and design of improved end closures for hydrostatic testing of cylinders and ring specimens. One goal is to reduce the discontinuity stresses at the cylinder ends that result from the use of rigid end closures. A typical end closure assembly of the type developed in this program is shown in Fig. 3.2-1. This closure is based on the concept of the contoured end plug, which was originally proposed by Miller.[34] The design shown in Fig. 3.2-1 is an improved concept end closure that incorporates an end plug with contour that achieves very low discontinuity stresses. The details of this design and the supporting theory will be published in a later report.

Analysis capabilities for use in designing cylinder end closures are developed under Task 1. Emphasis is given to developing closed-form analytic solutions for cylinder stresses that permit the efficient design of end closures without having to resort to detailed FE stress analysis. Each test assembly is analyzed to determine operational stress levels to insure end plug design adequacy. Analytical solutions are compared to FE results for validation of computed stresses.
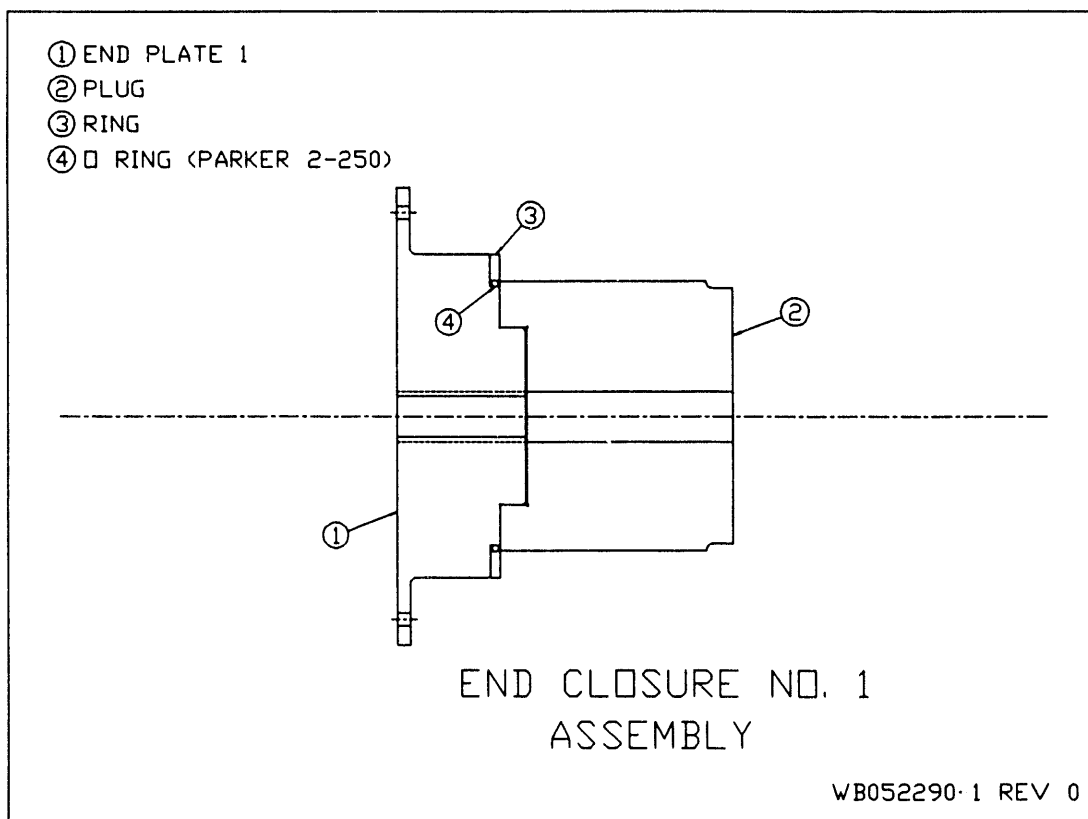
Fig. 3.2-1. End closure assembly.

3.3 DEMONSTRATION TESTING

This task consists of the test activities for the various test articles. Tests are performed at different test sites depending on the pressure and containment requirements for a particular test assembly. Tests are monitored using diagnostic methods for detecting failure initiation to facilitate identifying modes of failure. The imploded cylinders are subjected to posttest examination to confirm the suspected failure modes.

3.3.1 Cylinder Testing

Under this task, the hydrostatic testing of thick-section composite cylinders is accomplished. This effort includes the contracting for testing services and the logistics for shipping the test cylinders and end closures. This also includes the specification of the instrumentation, including strain gage and acoustic emission and the actual witnessing of each test. The compilation of data from the cylinder test reports, dimensional inspections, and laboratory analyses is included in this task. The fabrication of the end closure assemblies and replacement and/or modifications to the end plugs is also accomplished under this task.

3.3.1.1 Test article

The initial cylinder which was tested, cylinder C6-1, was made of IM6 fiber with ERL-2258 resin in an exact construction of $90[90_2/0_2/90_2]_{12}90$. The cylinder had an average internal diameter of 5.318 in. and an average outer diameter of 6.308 in. The cylinder overall length was 18.00 in. The minimum unsupported length at full pressure was 10 in.

3.3.1.2 Cylinder strain gaging

A total of 24 strain gages were affixed to the interior and exterior walls of the test cylinder. The location and orientation of these gages is shown in Figs. 3.3.1.2-1.
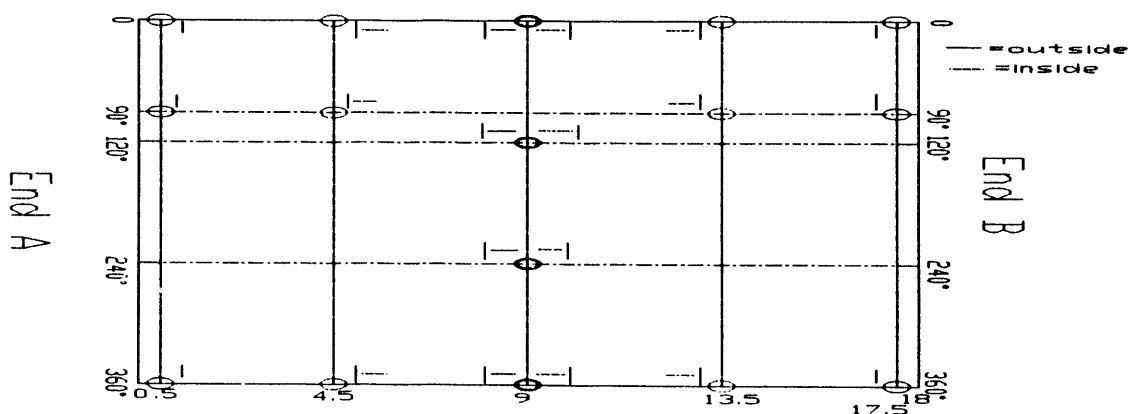
Fig. 3.3.1.2-1. Cylinder strain gage placement.

The axial locations for these gages were at midbay, at 4.5-in from either end, and at 0.5-in. from either end. The three midbay gages were located on both the interior and exterior walls and consisted of three biaxial gages, located at 120-degree intervals, that recorded hoop and axial strains. The two gages at 4.5-in. from each end were located on only the interior wall and were biaxial gages located at 0 and 90 degrees, that recorded hoop and axial strains. The gages at 0.5-in. from each end were located only on the exterior wall and were uniaxial gages, located at 0 and 90 degrees, that recorded hoop strain only.

3.3.1.3 Test facility

The cylinder was tested under contract with Hydrospace Engineering Services of Richardson, Texas, at the Stachiw Associates facility in El Cajon, California. The test facility consisted of a pressure vessel rated for use up to 20,000-psi hydraulic pressure. Pressure control was achieved manually by starting and stopping the pressurization system, by observing an analog gage indicating vessel pressure. Pressure was increased incrementally, stopping pressurization at 1000-psi intervals for strain gage readings. The approximate rate of pressurization was 2000 psi/min, with slower pressurization at the higher pressures. The vessel had associated feedthroughs for multichannel strain gage readout. Strain gage readout consisted of decade boxes connected to a single channel digital strain indicator. Individual gage readings were made manually by switching in the appropriate gage and writing down the reading on a data sheet. Acoustic emission monitoring was provided by attaching an acoustic emission pickup on the outside of the pressure vessel at mid-height. The accumulated number of events was recorded from a digital indicator as a function of pressure. Also, the event amplitude and count were plotted as a function of time and pressure on a strip chart recorder. Finally, the pressure level was monitored by a pressure transducer and plotted versus time on a strip chart recorder. Photographs of the test facility are shown in Figs. 3.3.1.3-1 and 3.3.1.3-2.

3.3.1.4 Test article assembly

The cylinder under test, C6-1, was assembled to the steel and aluminum end plugs prior to testing (see test cylinder assembly drawing in Fig. 1.3-1). The assembly drawing of one end closure is shown in Fig. 3.2-1. The internal strain gage wires were passed through the end plug and the wires were potted and sealed in place. Steel tie rods were attached to both end plugs to assist in holding the assembly together. Finally, the junction between the cylinder and the end plugs was sealed with a rubber potting compound to provide the initial seal for pressurization. Photographs of the cylinder assembly are shown in Figs. 3.3.1.4-1 and 3.3.1.4-2.
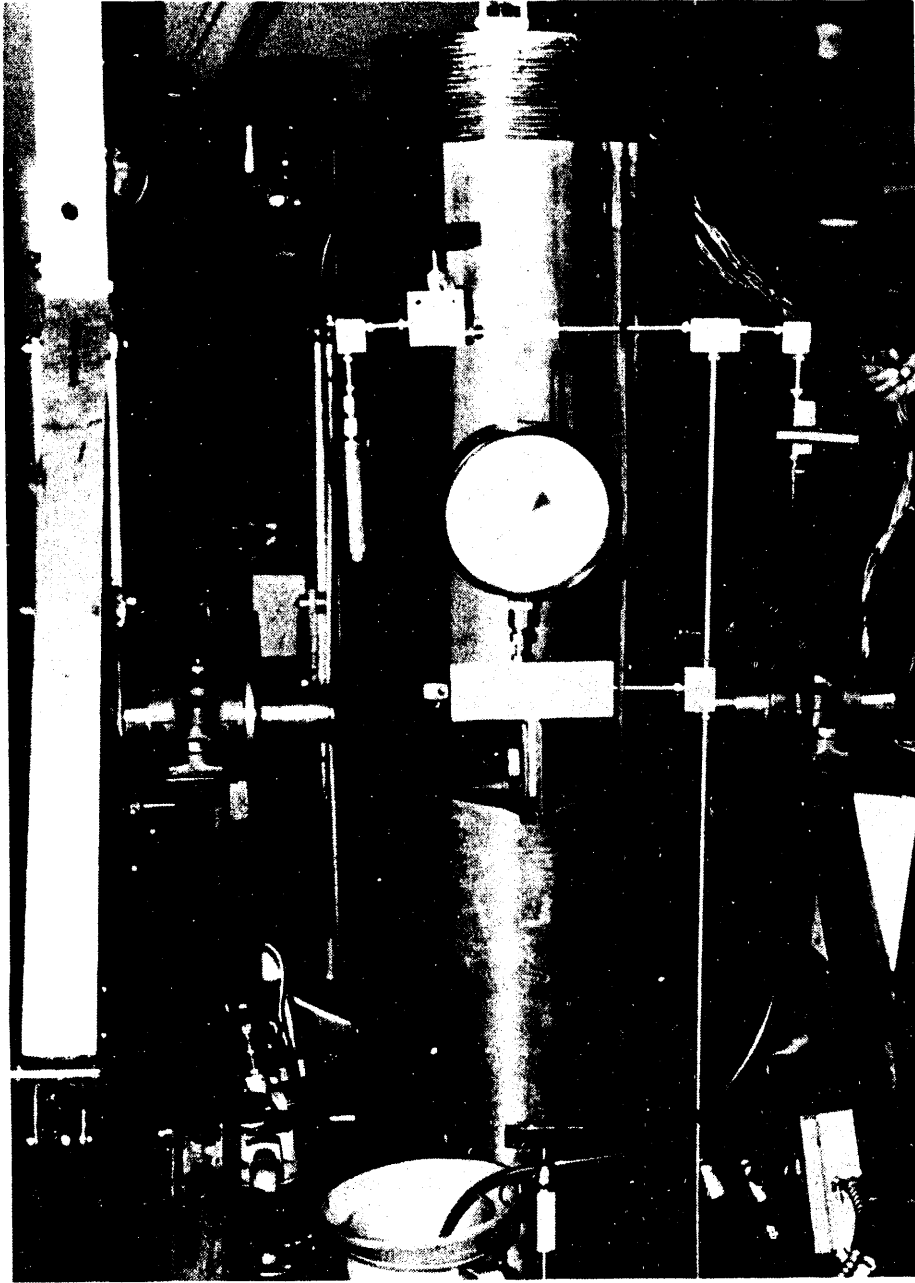
Fig. 3.3.1.3-1. Stachiw Associates test facility pressure vessel (20,000-psi capacity).
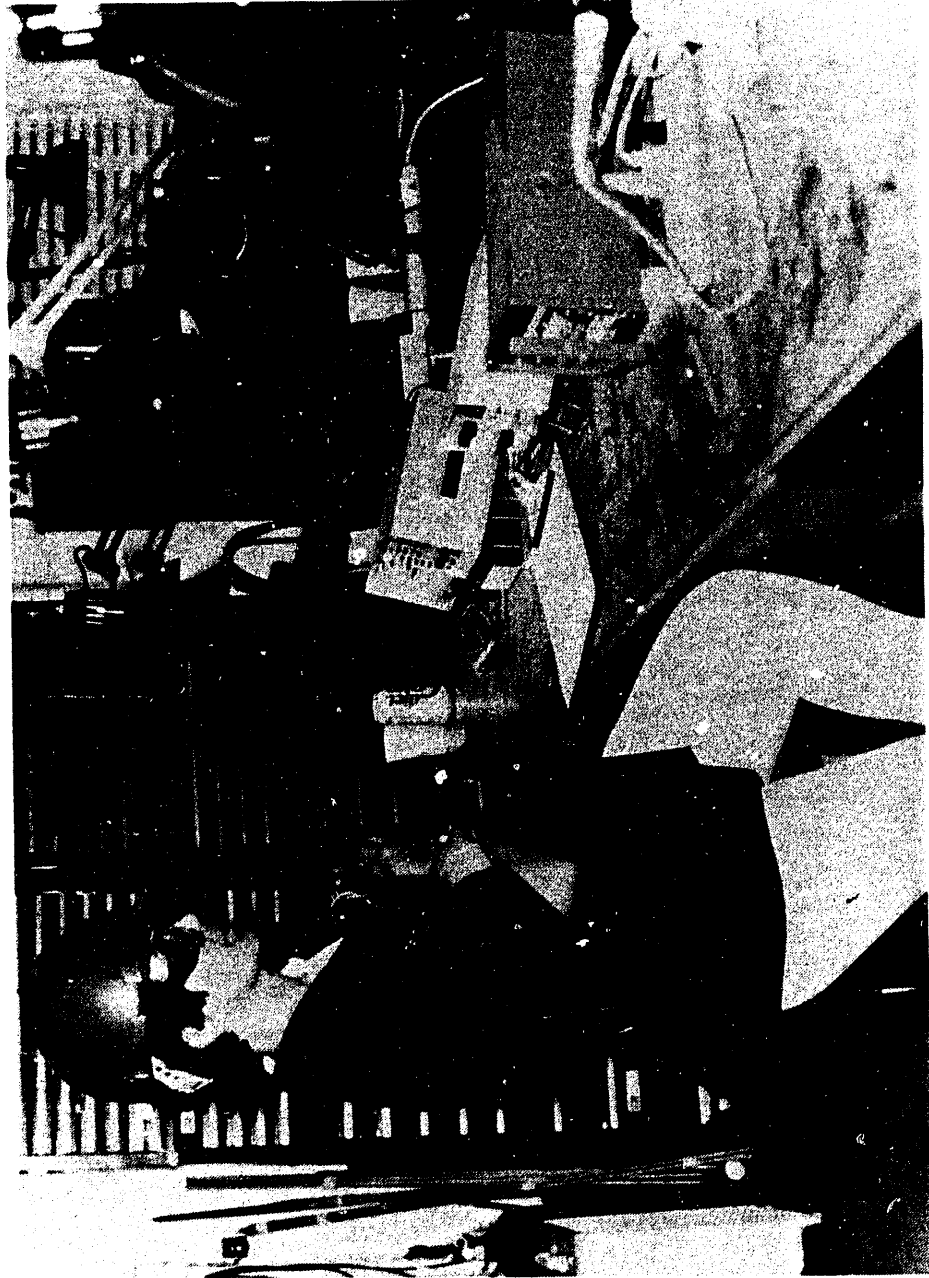
Fig. 3.3.1.3-2. Test facility instrumentation.
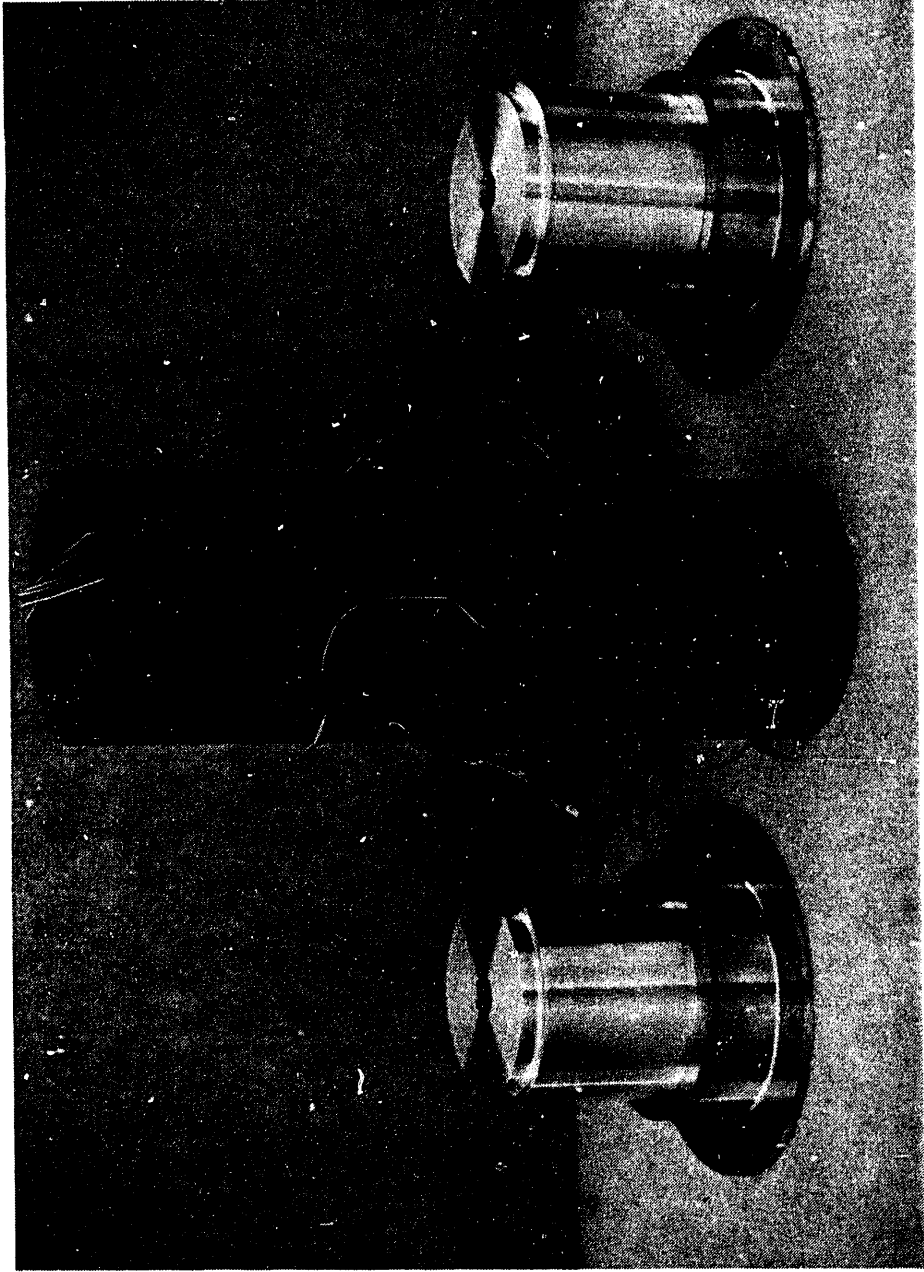
Fig. 3.3.1.4-1. Test cylinder C6-1 and steel and aluminum end closures.

Fig. 3.3.1.4-2. Cylinder C6-1 test assembly.

3.3.1.5 Testing

The cylinder was placed into the pressure vessel (see Fig. 3.3.1.3-1), the strain gage wires were fed out through a pressure feedthrough, and the pressure vessel was sealed. Pressurization began, with stops for strain gage readings made at each 1000-psi interval. The 24 channels of strain gages plus the acoustic emission count were recorded at each 1000-psi interval. Pressurization continued to the limit of the facility, which was 20,000 psi. Very little acoustic emission activity was noted, and there was no failure of the test cylinder. To preclude possible time dependent failure of the cylinder, once a pressure of 20,000 psig was reached, the vessel was depressurized after only a few seconds without waiting to acquire all 24 channels of strain data. One channel of strain data only was acquired at 20,000 psig. Complete strain data was acquired up to a pressure of 19,000 psig.

3.3.1.6 Strain gage results

Plots of the acquired strain vs pressure data are presented in Figs. 3.3.1.6-1 through 3.3.1.6-7. As may be seen from Fig. 3.3.1.6-1, interior wall midbay hoop strain levels of 0.8 to 0.9% were achieved with this specimen.
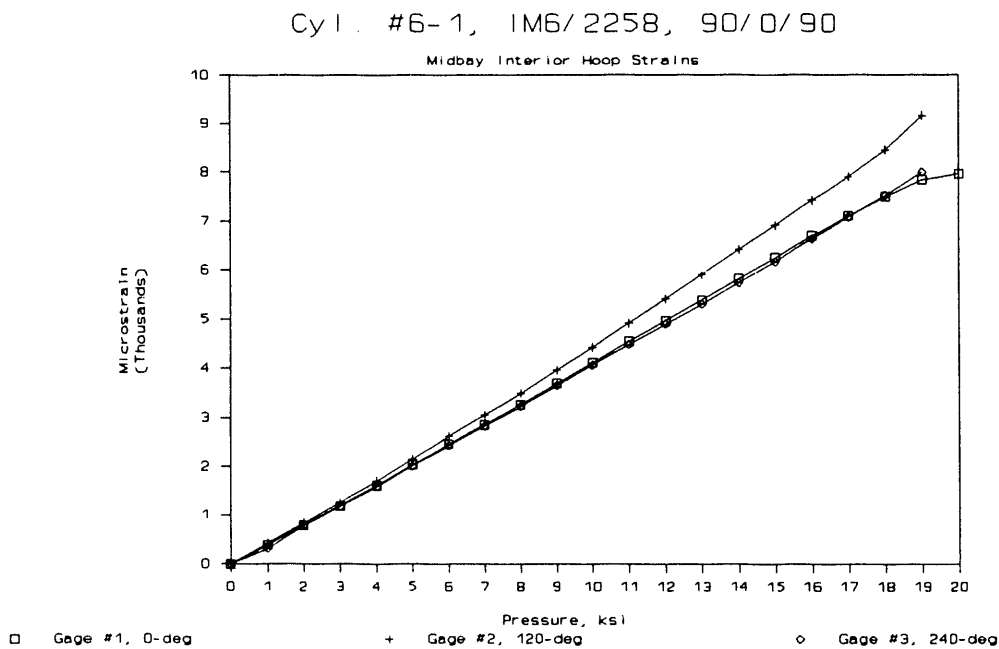
Fig. 3.3.1.6-1. Midbay interior hoop strains vs pressure.

Cyl #6-1, IM6/2258, 90/0/90

Midbay Exterior Hoop Strains

□ Gage #8, 0-deg   + Gage #9, 120-deg   ◇ Gage #10, 240-deg
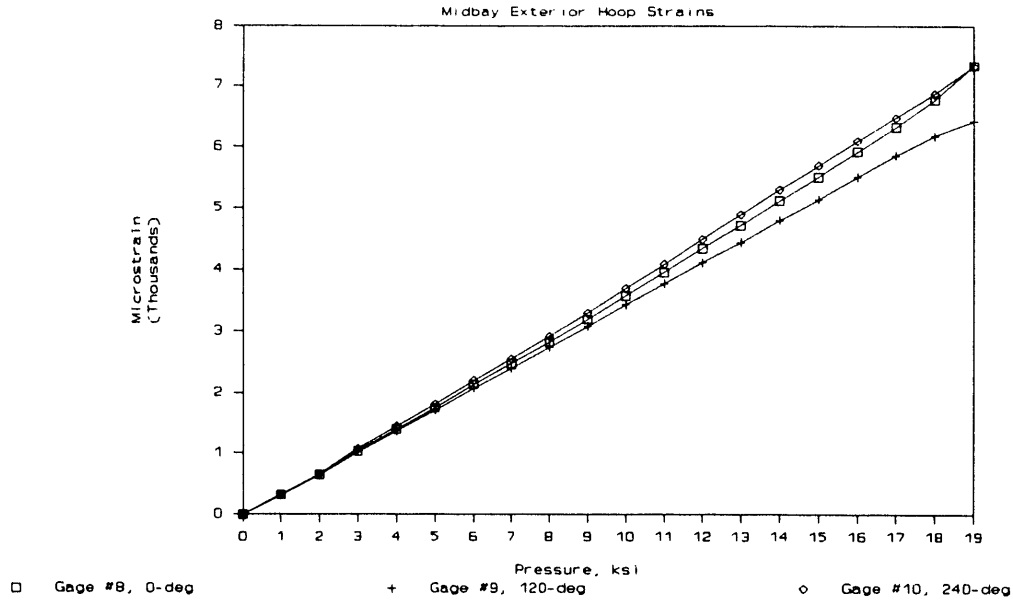
Fig. 3.3.1.6-2. Midbay exterior hoop strains vs pressure.

Cyl #6-1, IM6/2258, 90/0/90

Midbay Interior Axial Strains

□ Gage #1, 0-deg   + Gage #2, 120-deg   ◇ Gage #3, 240-deg
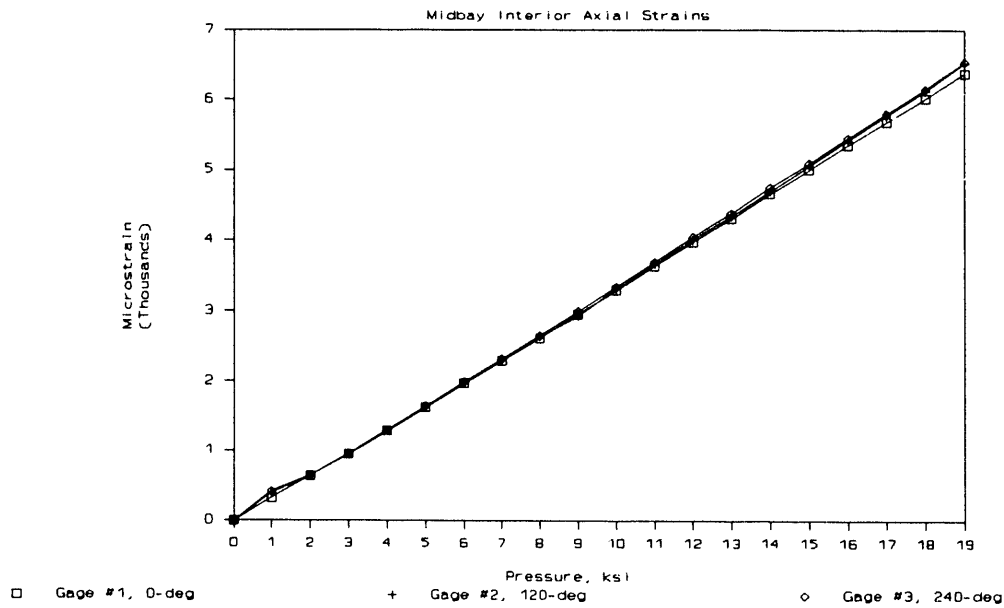
Fig. 3.3.1.6-3. Midbay interior axial strains vs pressure.

Cyl #6-1, IM6/2258, 90/0/90

Midbay Exterior Axial Strains
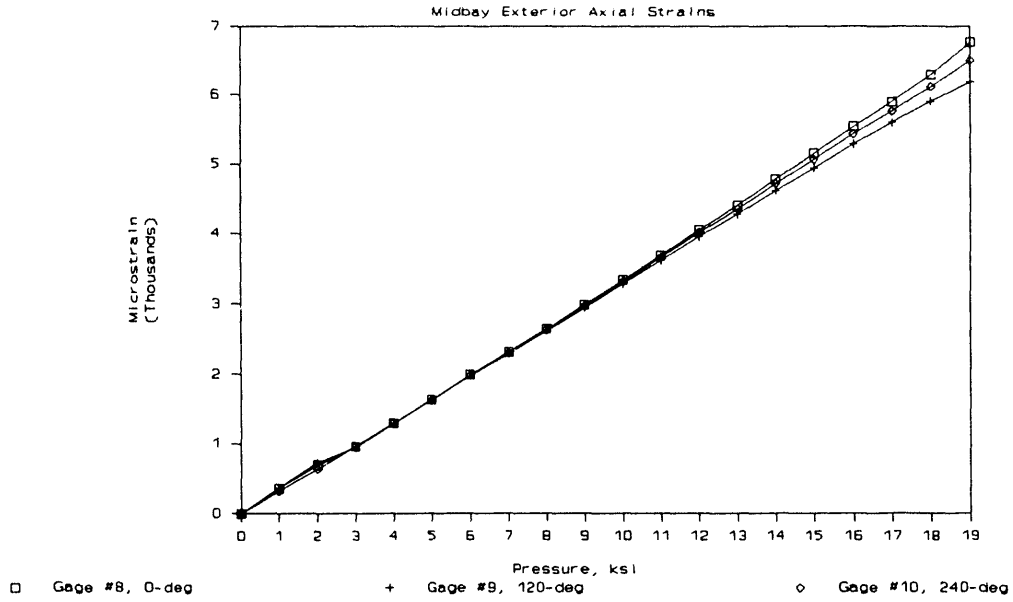
Fig. 3.3.1.6-4. Midbay exterior axial strains vs pressure.

Cyl #6-1, IM6/2258, 90/0/90

4.5" from End, Interior Hoop Strains
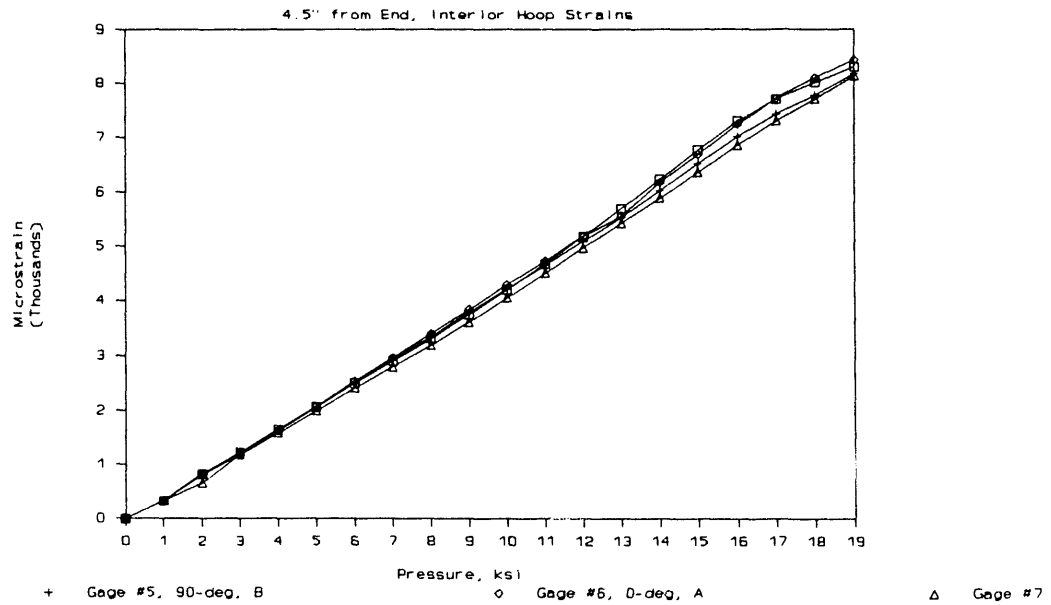
Fig. 3.3.1.6-5. Interior hoop strains at 4.5 in. from end vs pressure.

Cyl. #6-1, IM6/2258, 90/0/90

4 5" from End, Interior Axial Strains
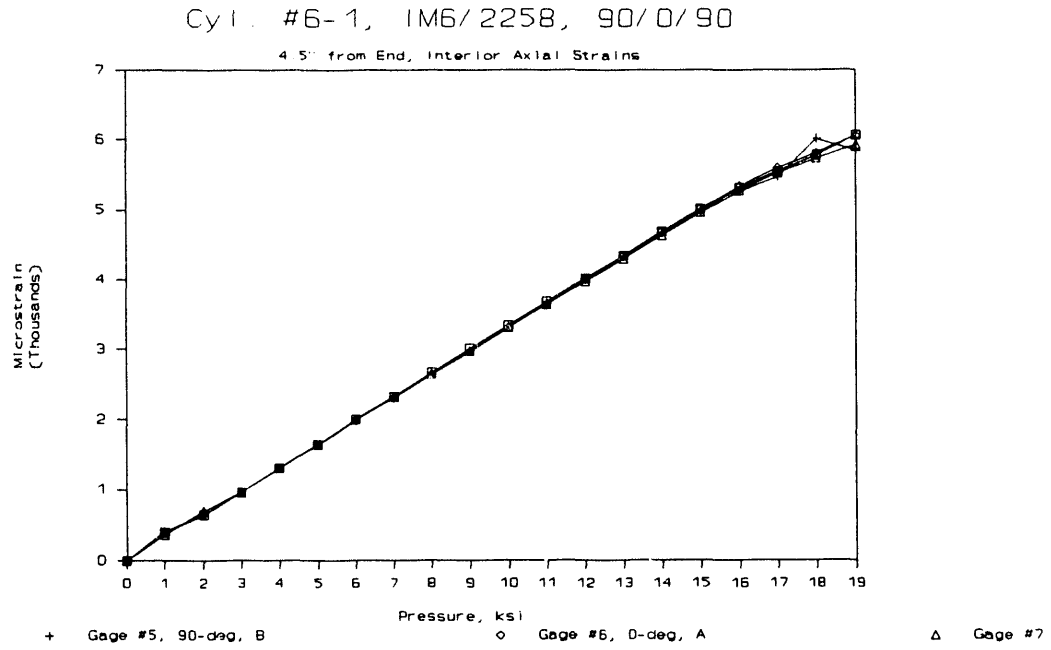
Fig. 3.3.1.6-6. Interior axial strains at 4.5 in. from end vs pressure.

Cyl. #6-1, IM6/2258, 90/0/90

0 5" from End, Exterior Hoop Strains
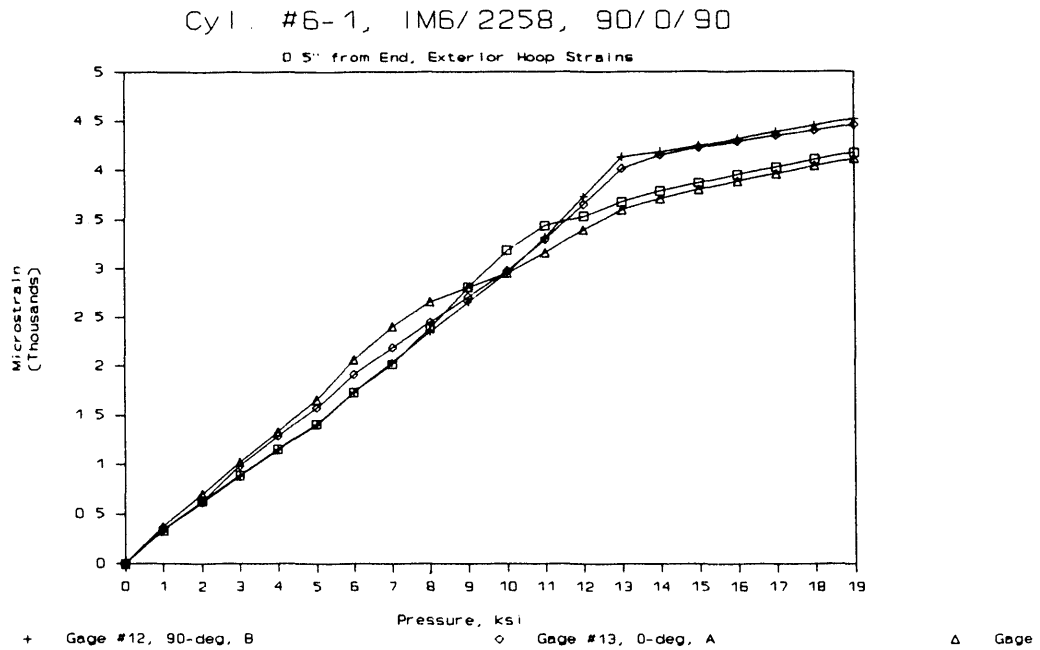
Fig. 3.3.1.6-7. Exterior hoop strains at 0.5 in. from end vs pressure.

The gage located at the 120-degree location recorded an increasingly greater compressive hoop strain with pressure than did the gages located at 0 degrees or 240 degrees. However, on the exterior of the cylinder, the gage at the 120-degree location showed an increasingly smaller compressive hoop strain with pressure than did the gages at the 0-degree or the 240-degree locations. This would suggest that circumferential bending, producing tension on the exterior wall and compression on the inner wall, was occurring as a function of pressure at the 120-degree location.

A similar situation occurred with respect to the midbay axial strains. The interior gage at the 0-degree location showed an increasingly smaller axial strain with pressure while the exterior gage showed an increasingly greater axial compressive strain with pressure. This would tend to indicate the progression of some degree of axial bending which produced compression on the exterior wall and tension on the interior wall, or a bowing inward of the cylinder at midbay.

As illustrated in Fig. 3.3.1.6-7, the hoop strain at 0.5 in. from the cylinder end vs pressure showed a change of slope between 10,000 and 13,000 psi external pressure where the contracting cylinder begins to contact the internal plug. This provided increased hoop stiffness to the assembly.

3.3.1.7 Posttest cylinder inspection

After pressurization, the test assembly was taken apart and the cylinder was inspected visually. No evidence of damage was noted, with the exception of some slight scuffing on the interior of the cylinder at the approximate location of the end of the aluminum end plugs. Evidently, the cylinder contracted such that the full length of the contoured end plug was contacted.

3.3.2 Ring Testing

Tests of ring specimens cut from each end of the cylinder were performed. The rings were tested in the 6-in. diam. strain-controlled test fixture described in ref. 8.

3.3.2.1 Ring specimens

Short rings were cut from the ends of cylinders C6-1, a 90/0/90 construction, and C6-3, a 90/0 construction. The rings had a 6.3-in. OD, a 5.3-in. ID, and a 0.5-in. axial length. The rings were ground to remove approximately 0.020 in. diametral from their as-wound outer surface. The rings were instrumented with two hoop-direction uniaxial strain gages located 180-degrees apart on the ring ID surface.

Six rings were cut from each end, labeled "A" and "B", of cylinder C6-1. However, due to delaminations extending to one end of the cylinder, which were discovered during machining of cylinder C6-3, six rings were cut from only the "A" end of cylinder C6-3. Ultrasonic examination showed that the area where the C6-3 rings were cut did not exhibit delaminations.

3.3.2.2 Test fixture

The rings were tested in the ORNL strain-controlled ring test fixture.[6-9] This fixture places the rings in the central tapered bore of a large steel cylinder. A matching piston forces the rings, through lateral pressure, down the tapered bore, producing increasing hoop compressive strain in the rings. The level of compressive strain achieved is monitored by strain gages attached to the ring ID surface. Acoustic emission was monitored by attaching an acoustic emission pickup to the outer surface of the steel cylinder at the approximate axial location of failure of the rings.

3.3.2.3 Testing

The order of testing was rings from the "A" end of cylinder C6-1, from the "B" end of cylinder C6-1, and from the "A" end of cylinder C6-3. The rings were placed into the bore of the test fixture and the piston rate was adjusted to displace the rings down the tapered bore at a rate of 1in./min. This produced an approximate hoop strain rate on the ring ID of 0.135 %/min. During testing, the piston load, the piston diplacement, the strain gage readings, and the acoustic emission count were measured as a function of time. Testing continued until maximum load capability was reached.

3.3.2.4 Test results

The rings from cylinder C6-1 exhibited an average failure strain of 7935 microstrain compressive strain with a standard deviation of 894 microstrain. The rings from cylinder C6-3 exhibited an average failure strain of 9673 microstrain with a standard deviation of 717 microstrain.

The laminate modulus was calculated by assuming linear elasticity for the ring material. The composite stress on the inner and outer diameters was calculated by using the Lekhnitsky relations, and the ring critical buckling radial pressure was calculated. These results are shown in Table 3.3.2.4-1, along with previously obtained results from rings from the AUSS scale cylinder, a geometrically similar cylinder of the same material with a nominal $90_{25}/0$ construction.

The failure mode observed for the rings from C6-1 was a shear type fracture at an angle to the axial plane, usually accompanied by a single major delamination at the mid-thickness of the ring. Failure resulted in a single drop in load carrying capability of the ring to zero.

In contrast, the failure mode observed for the rings from C6-3 was a progressive failure, with the initial failure observed to be delamination of the innermost ply, followed by a partial reduction in load from its peak value. Further increases in load caused delamination of the second innermost ply, which usually resulted in gross failure of the remainder of the ring. Much more postfailure delamination through the thickness of the ring was observed in these rings. Previously tested hoop-wound rings of this material showed only local delaminations near the fracture site. By comparison, much more global delaminations were seen in these two materials. The greater amount was seen in the material with the greater proportion of axial plies, cylinder C6-3.

Table 3.3.2.4-1. Calculated ring test results

Material	Laminate	Dimensions					Properties				Str. (r=a)	Str. (r=b)	Str. P_{cr}	Timo. Buck. P_{cr}	Ratio
		a	b	t	R_o/t	L	E_θ (MSI)	E_r (MSI)	k	D_{xx}					
C6-1	[90/0/90]	2.6587	3.1440	0.4853	5.98	0.500	15.71	1.489	3.248	150,900	124.66	121.44	18561	18536	1.00
C6-3	[90/0]	2.6586	3.1570	0.4984	5.83	0.500	12.25	1.489	2.868	129,200	118.49	112.15	17848	15765	1.13
AUSS	[90$_3$/0$_2$]$_{MS}$	2.6596	3.1615	0.5019	5.80	0.502	15.57	1.469	3.256	161,200	133.84	130.90	20508	19614	1.05

4. PROJECT MANAGEMENT

This task responsibility includes the coordinating responsibility for all the activities of the project and the reporting responsibility to the Director. In addition, the attendance at meetings and conferences for the purpose of presentation of results is accomplished under this task.

CONCLUSIONS

This report describes initial activities and results from a three-year project to develop performance models for thick-section composite cylinders loaded in compression. The activities are both analytical and experimental in scope. The work, as described, covers the various elements of the project including design, analysis, fabrication, and testing. Particular emphasis is given to the validation of the stress and failure models by carefully designed tests of cylinders subjected to hydrostatic loading. Significant effort has been applied to the design of improved metal end closures for hydrostatic testing. The first cylinder tested using the improved end closures achieved a record pressure and stress level for a graphite composite cylinder.

Several analytical efforts were initiated to develop improved solutions for stresses, buckling, and failure of thick-section composite cylinders. These activities included an evaluation of existing theories found in open literature, at universities, and at other government laboratories. Although these investigations are still ongoing, several significant results have already been achieved. On the basis of preliminary results, the following conclusions and recommendations are made:

1. Accurate determination of the stresses in thick, laminated composite cylinders requires a three-dimensional analysis that includes the radial deformations and which appropriately accounts for the discrete layers by orientation and radial position within the thickness of the cylinder. Elasticity solutions such as Hyer's provide an initial analysis capability that is valid in the midplane region of the cylinder where effects of the end closures are minimal. Accurate determination of the detailed stresses in the end regions of the cylinder, where localized transverse shear and bending stresses are caused by the end closures, can only be accomplished at present by FE analysis. Analytic solutions that include the axial bending and transverse shear gradients are presently limited to shell formulations. The shell theories do not adequately treat the radial deformations in thick cylinders and can only approximate the transverse shear deformations. Three-dimensional elasticity solutions that accurately treat the radial deformations and which also include the axial variations have not yet been developed. These solutions are needed to facilitate the design of improved end closures and to reduce the analysis burden associated with detailed FE analysis. These solutions would also greatly facilitate the development of failure theories for thick composite cylinders.

2. Examination of the solutions of Hyer and Roy indicated numerical difficulties for isotropic layers or for transversely isotropic axial layers ($\theta = 0°$). The difficulty was traced to repeated roots in the characteristic equation for these special cases.

3. Modifications to the elasticity solution of Hyer by Starbuck successfully eliminated the numerical difficulties that arise from the repeated roots in the case of isotropic layers and in the case of transversely isotropic axial layers.

4. Comparison of results from the modified Hyer theory (Starbuck's CCAP) with results from Hyer's original code (ELCYL) indicated exact agreement except for the above special cases.

5. Comparisons of results from CCAP, ELCYL, and Roy's CYLIN show minor differences between CYLIN and the other two codes. These differences were not resolved even after modifying the CYLIN code to use the outer radius rather than the mean radius for determining the axial pressure area.

6. Accurate strains but not accurate layer stresses can be predicted by modeling a laminated cylinder as a single layer having equivalent smeared properties.

7. Results from CCAP using smeared properties were also compared with the FEM results. Excellent agreement was obtained in all cases except for the radial strains, which were underestimated by the FEM. The close agreement for displacements and strains suggests that the layer stresses could be extracted from the smeared composite stresses in a postprocessing step. This step would be required if failure criteria are to be applied in the regions of stress discontinuity near the end closures.

8. Comparison of the three-dimensional solution in CCAP with laminated shell theory (LST) and with the CYLAN code indicated that results were not in exact agreement for axial and hoop components of stress and strain. Assuming a two-dimensional stress state for analyzing laminated cylinders subjected to hydrostatic pressure will underpredict the hoop strains and overpredict the axial strains. Consequently, accurate predictions for strains requires a three-dimensional analysis. Results from CYLAN were in better agreement with the three-dimensional analysis than were results from LST. This suggests that the radial normal strain correction in CYLAN improves the accuracy over LST for thick cylinders.

9. As is the case with stress analysis, three-dimensional analysis methods are required for buckling analysis of thick-section laminated composite cylinders. Available closed-form solutions are based on various shell theories which all rely on thin shell assumptions for validity. The accuracy of these theories has not yet been established for thick cylinders. At present, the range of applicability of these theories can only be determined by experiment or by FE analysis. General three-dimensional buckling solutions are needed to provide the required analysis capability.

10. A cylinder buckling solution based on an extension of Flugge's theory by Starbuck gave results that were in close agreement with the solution of Cheng and Ho. The extended solution was for an unsymmetric laminated cylinder and was based on the general curvature relations of Ambartsumyan.

11. A version of Starbuck's formulation with Donnells's approximate curvature expressions gave results that were in close agreement with the theories of Jacobsen, Baker, and Jones.

12. For the cylinders investigated in this study, i.e., cylinders having only axial and hoop layers in a dispersed lay-up (with n = 72), the effects of the discrete layers are negligible. Modeling the laminated cylinders as a single layer having equivalent smeared properties predicted nearly identical buckling pressures as the 72-layer cylinder model.

13. The computed critical pressures for hydrostatic or lateral loading based on the Donnell approximation (i.e., Jacobsen, Baker, and Jones) are consistently higher than the computed critical pressures based on the Ambartsumyan curvatures (Cheng & Ho and Starbuck). The Donnell-based pressures are also higher than those based on Starbuck's theory with curvatures from Timoshenko and Love and on Whitney's theory with transverse normal strains.

14. For the cylinders investigated in this study, the radial normal strain correction of Whitney had a negligible effect on the buckling pressures. This is contrary to the result obtained in the application of laminated shell theory to the stress analysis of thick laminated cylinders. In these results it was found that the radial strain correction improved the accuracy of the computed layer stresses.

15. Critical pressures for buckling of finite length cylinders (L/D=1.7) subjected to hydrostatic or lateral loading increased only slightly when the cylinder hoop to axial ply ratio was increased from 1:1 to 3:1. The critical pressure increased by only 2.6% for an increase in circumferential flexural stiffness of 15.3%. The insensitivity of the critical pressure to the circumferential stiffness was not expected. This result suggests that the effect of the supported ends of the finite length cylinder dominates the buckling behavior of thick cylinders and that the circumferential stiffness effect is of secondary importance.

16. Critical pressures for buckling of infinitely long cylinders (i.e., L/D --> ∞) subjected to hydrostatic or lateral loading increase in proportion to the circumferential bending stiffness.

17. Critical pressures for buckling of infinitely long cylinders subjected to hydrostatic or lateral loading that are computed from theories which utilize the Donnell approximation for the curvatures are higher than predictions based on the theories that utilize the curvature expressions of Ambartsumyan or Timoshenko and Love. The ratio of the asymptotic values is 4/3. Determination of which of these values is correct will require FE analysis to resolve the discrepancy.

18. Critical pressures for buckling of long cylinders subjected to axial loading as predicted by the theory of Jones are much higher than the predictions from the other theories. The analytic solution of Jones predicts an infinite critical pressure as the cylinder length becomes infinite.

19. The initial FE stress analysis of thick laminated cylinders was based on smeared elastic properties for the laminate. Techniques for FE modeling of the individual layers are being evaluated. The evaluation includes several different analysis codes and computing facilities.

20. FE stress results based on smeared equivalent orthotropic elastic constants provide composite stress values that are useful for evaluating the adequacy of an end closure design for specific test cylinder dimensions and laminate construction. Agreement between FE and three-dimensional elasticity solutions with smeared properties for displacements, strains, and composite (smeared) stresses in thick cylinders containing many layers indicates that accurate layer stresses could be extracted from the composite stresses in a postprocessing step.

21. The failure analysis of thick-section laminated composites is complex in nature because of the large number of possible failure modes that occur at the micro and macro material levels. As yet, no single criteria has been proposed that includes all the possible modes. Rather, specialized models have been proposed, each emphasizing one or more modes that are believed to be the dominant modes or the initiating modes for thick composite cylinders loaded in compression. The shear number of failure criteria that have been proposed is great; thus, the evaluation of all of them would be no small task. Failure criteria have been classified in various ways by many researchers. Labels such as "engineering failure criteria" and "phenomenological failure criteria" have been attached to specific criteria. A loose interpretation of these labels would be that the engineering criteria neglect the material imperfections and specific modes of failure whereas the phenomenological criteria consider the imperfections and treat the actual failure modes. Some criteria have been referred to as micromechanical, because the analysis is applied at the layer or constituent level; others have been referred to as macromechanical, when the analysis is done at the laminate level. There is no universally accepted approach for cataloging the many criteria. More important, there has not been a careful comparison of even the most popular theories nor a rigorous testing of them against experiment.

22. Results from the initial analyses and experiments indicate that the engineering type failure criteria give useful predictions for expected performance of thick-section composite cylinders under certain conditions. Material strength allowables, which are inserted into the criteria, must be based on representative tests of unidirectional rings and cylinders, and the cylinder stresses must be derived from an accurate three-dimensional stress analysis applied at the layer level.

23. For the five different failure criteria examined in this study, the predicted failure pressures for three different cylinder designs differed by less than 20%.

24. The Hashin criteria gives the lowest failure pressure for the cases analyzed. The two-dimensional form of the Tsai-Wu criteria gave the highest pressures.

25. The Hashin failure criteria discriminates between matrix and fiber modes of failure whereas the Tsai-Wu criteria does not. Both indicate the identity of the first ply to fail. Hashin's criteria delineates failure between four basic modes: tensile fiber mode, tensile matrix mode, compressive fiber mode, and compressive matrix mode. For the graphite fiber reinforced cylinders studied in this investigation, the first-ply failure mode and location were seen to be strong functions of the allowable transverse compressive strength used in Hashin's criteria. The Hashin criteria should permit a more complete validation since both the first-ply failure location and mode are predicted and can be separately confirmed in addition to the cylinder failure pressure.

26. Failure analysis results for the record cylinder (C6-1), when the analysis is based on the Hashin criteria with > 15-ksi transverse compressive strength, are consistent with the pressure achieved in testing. Buckling predictions for the 10-in. unsupported length were close to the strength predictions for the 20-ksi value of transverse compressive strength. It is not possible to speculate as to the expected mode of failure for this cylinder because the values are close and the test was terminated at 20,000 psig without failure.

27. The delaminations that occurred during cutting of IM6 graphite cylinders C6-2 and C6-3 were likely caused by higher than normal residual fabrication stresses. These two cylinders were fabricated with ply ratios that had not been previously fabricated at ORNL with the IM6 graphite material. Successful fabrication of these laminate constructions may require exploratory tests that are beyond the scope of this project. At the minimum, sufficient trial fabrications should be done to explore several changes in the winding process, which are expected to reduce the tendency for occurrence of this premature failure mode. For the time being, no further attempts will be made to fabricate these lay-ups with graphite.

28. The maximum hoop strain value achieved during the hydrotest of cylinder C6-1 was slightly higher than the value obtained from tests of ring specimens cut from the ends of the cylinder. This was the result even though the test cylinder did not fail and therefore the strain level had not yet reached the ultimate strain value in the cylinder test. This result indicates that strain controlled ring tests of cross ply material rings cut from test cylinders provide strain values that are conservative relative to values for a hydrostatically loaded cylinder. This difference in ultimate strains for the two tests may be a result of the difference in stress states for the ring and cylinder.

29. Ring tests of 2-in.-diam. unidirectional rings from an earlier program[6,7] achieved ultimate hoop strains of over 1%. These data were used to estimate the 250-ksi value for the fiber direction compression strength used in the initial failure analysis. Later tests[8] of 6-in.-diam. unidirectional rings

of the same material gave lower strains than were achieved on the 2-in. rings and slightly less than the hoop strain in the record cylinder. Also, the ultimate strains values of rings cut from the AUSS model scale cylinder were slightly higher than for the rings cut from the record cylinder.[8] The compressive strength allowables will be revised as additional data become available.

RECOMMENDATIONS

The following recommendations are based on the initial analytical and experimental results.

1. A three-dimensional elasticity solution for thick-section laminated composite cylinders, including the effects of axial bending and transverse shear, should be developed. This solution is needed to provide a stress analysis capability for analyzing cylinders with realistic boundary conditions.

2. To provide an interim analysis capability, existing shell theories that include transverse shear deformation effects should be applied to the analysis of laminated composite cylinders subjected to axial bending and transverse shear.

3. Shell buckling theories should be modified to include the transverse shear and radial deformation effects.

4. The effect of residual thermal and hygroscopic stresses should be included in the stress terms of the applied failure criteria.

5. Additional failure modes, e.g., ply buckling, need to be incorporated into the closed form analytic solution. This will require a non-axisymmetric analysis to allow the deformations to vary around the circumference of the laminated cylinder. These modes could also be incorporated into the failure criteria as submodels for computing the compressive strength allowables.

6. The ability of existing FE codes and other numerical techniques to accurately predict the critical buckling pressure for hydrostatically loaded thick composite cylinders requires further investigation.

7. Continued effort is needed towards designing, fabricating, and testing demonstration articles for validation of failure criteria.

8. A hydrostatic test capability beyond the present capacity of 20,000 psig is needed to permit testing of thicker cylinders to ultimate material failure. Present facilities are marginal for evaluating available materials.

9. Efforts to standardize test method and equipment for hydrotesting thick-section laminated composite cylinders should be increased. Particular attention should be given to the standardization of the methodology for the design of metal end closures. This must include the setting of acceptable maximum values for bending and transverse shear stresses. Appropriate tests of each material should be conducted to establish the maximum values.

REFERENCES

1. H. J. Garala, *Structural Evaluation of Externally-Pressurized, 4-Inch Diameter, Graphite Composite Cylinders*, NDW-DTNSRDC 4610/3 (Rev. 3-80), David Taylor Naval Ship Research and Development Center, Bethesda, Md., Aug. 1984.

2. H. J. Garala, *Experimental Evaluation of Graphite-Epoxy Composite Cylinders Subjected to External Hydrostatic Compression Loading*, Society of Experimental Mechanics.

3. H. J. Garala, *Structural Evaluation of 8-Inch Diameter Graphite-Epoxy Composite Cylinders Subjected to External Hydrostatic Compressive Loading*, DTRC-89/016, Ship Structures and Protection Department, David Taylor Naval Ship Research and Development Center, Bethesda, Md., Sep. 1989.

4. J. S. Maye, *Preliminary Consideration for Developing Designs of Composite, Ring-Stiffened Cylinders Under Hydro-Static Loading*, DTRC-SSPD-91-172-41, Ship Structures and Protection Department, David Taylor Naval Ship Research and Development Center, Bethesda, Md., Apr. 1991.

5. J. D. Stachiw and B. Frame, *Graphite-Fiber-Reinforced Plastic Pressure Hull Mod 2 for the Advanced Unmanned Search System Vehicle*, Technical Report 1245, Naval Ocean Systems Center, San Diego, Calif., Aug. 1988.

6. H. W. Blake, *Compression Failure of Graphite/Epoxy Rings Under Strain Control Loading*, K/ETAC-5, Oak Ridge Gaseous Diffusion Plant, Martin Marietta Energy Systems, Inc., Jun. 1987.

7. H. W. Blake, *Compression Failure of Graphite/Epoxy Rings Under Strain Control Loading*, Joint Symposium on Composite Materials Science and Engineering, American Society for Composites/University of Delaware Center for Composite Materials, Sep. 23-25, 1987.

8. H. W. Blake, *Compression Failure Modes of Six-Inch-Diameter Composite Rings*, ORNL/ATD-37, Oak Ridge National Laboratory, Martin Marietta Energy Systems, Inc., May 1990.

9. D. E. Welch, *Analysis of Composite Ring Compression Test Data*, ORNL/ATD-24, Oak Ridge National Laboratory, Martin Marietta Energy Systems, Inc., Nov. 1989.

10. M. W. Hyer, "Hydrostatic Response of Thick Laminated Composite Cylinders," *Jrl. Reinforced Plastics & Composites*, Vol. 7, pp. 255-262, Aug. 1988.

11. A. K. Roy and S. W. Tsai, "Design of Thick Composite Cylinders," *Jrl. of Pressure Vessel Tech.*, Trans. of ASME, Vol. 110, pp. 255-262, Aug. 1988.

12. S. W. Tsai and E. M. Wu, "A General Theory of Strength for Anisotropic Materials," *J. Composite Materials*, Vol. 5, p. 58, 1971.

13. S. A. Ambartsumyan, *Theory of Anisotropic Shells*, NASA Technical Translation, NASA TTF-118, 1964.

14. J. M. Whitney, "On the Use of Shell Theory for Determining Stresses in Composite Cylinders," *J. Comp. Matl.*, Vol. 5, pp. 340-353, Jul. 1971.

15. A. E. H. Love, *A Treatise on the Mathematical Theory of Elasticity*, 4th. ed., Dover Publications, New York, 1944.

16. S. W. Tsai. and T. Hahn, *Introduction to Composite Materials*, Technomic Publishing Co., Lancaster, Penn., 1980.

17. Z. Hashin, "Failure Criteria for Unidirectional Fiber Composites," *J. App. Mech.*, Vol. 47, pp. 329-334, Jun. 1980.

18. M. Stein and J. Mayers, *A Small-Deflection Theory for Curved Sandwich Plates*, NACA Report 1008, 1951.

19. H. R. Jacobsen, *Optimum Construction of Reinforced Plastic Cylinders Subjected to High External Pressure*, Final Report, Douglas Report SM-45871, Mar. 1964.

20. E. H. Baker, L. Kovalevsky, and F. L. Rish, *Structural Analysis of Shells*, Krieger Publishing Co., Inc., Malabar, Fla., 1972.

21. S. Cheng and B. P. C. Ho, "Stability of Heterogeneous Aeolotropic Cylindrical Shells Under Combined Loading," *AIAA Jrl.*, Vol. 1, No. 4, pp. 892-898, Apr. 1963.

22. R. M. Jones, "Buckling of Circular Cylindrical Shells With Multiple Orthotropic Layers and Eccentric Stiffeners," *AIAA Jrl.*, Vol. 6, No. 12, pp. 2301-2305, Dec. 1968.

23. R. M. Jones and H. S. Morgan, "Buckling and Vibration of Cross-Ply Laminated Circular Cylindrical Shells," *AIAA Jrl.*, Vol. 13, No. 5, pp. 664-671, May 1975.

24. D. Bushnell, "Computerized Analysis of Shells-Governing Equations," *Computers & Struc.*, Vol. 18, No. 3, pp. 471-536, 1984.

25. S. P. Timoshenko and J. M. Gere, *Theory of Elastic Stability*, Eng. Soc. Monographs, 2nd. ed., McGraw-Hill, New York, 1961.

26. W. Flugge, *Stresses in Shells*, Springer-Verlag, New York, 1967.

27. Test Report, Private Communication from Cynthia A. Cesena of Hydrospace Engineering Services to D. E. Welch, Oak Ridge National Laboratory, Oak Ridge, Tenn., July 1990.

28. J. O. Hallquist, *NIKE2D - A Vectorized, Implicit, Finite Deformation, Finite Element Code for Analyzing the Static and Dynamic Response of 2-D Solids*, UCID-19677, Lawrence Livermore National Laboratory, Feb. 1983.

29. J. O. Hallquist, *MAZE - An Input Generator for DYNA2D and NIKE2D*, UCID-19029, Rev. 2, Lawrence Livermore National Laboratory, Jun. 1983.

30. J. O. Hallquist, *ORION - An Interactive Post-Processor for the Analysis Codes NIKE2D, DYNA2D, and TACO2D*, UCID-19310, Rev. 1, Lawerence Livermore National Laboratory, Jul. 1983.

31. Engineering Mechanics Research Corporation, *Users Manual for NISA II, Numerically Integrated Elements for System Analysis, Version 90.0*, Troy, Mich., Apr. 1990

32. Hibbit, Karlsson and Sorensen, Inc., *ABAQUS Users Manual Ver. 4.7*, Providence, R.I.

33. ADINA R & D, INC., ADINA 5.0, *A Finite Element Program for Automatic Dynamic Incremental Nonlinear Analysis*, Watertown, Ma., Jun. 1987

34. R. J. Miller, *End Plugs for External Pressure Tests of Composite Cylinders*, STP 460, American Society for Testing and Materials, 1969.

DISTRIBUTION

Martin Marietta Energy Systems, Inc.

B. R. Appleton
H. W. Blake (10)
R. S. Carlsmith
J. L. Cook
B. J. Frame
W. Fulkerson
H. J. Grimsby
D. R. Johnson
J. E. Jones Jr.
W. S. Key
W. R. Martin
W. C. McWhorter
R. O. Meyers
R. E. Norris
D. U. O'Kain
J. T. Shaffer
B. B. Smith
J. M. Starbuck
J. O. Stiegler
A. J. Szady
R. C. Ward
D. A. Waters
D. E. Welch
R. E. Ziegler
A. Zucker
Manager, Laboratory Directed Research and Development
Laboratory Records - RC
Laboratory Records Department (2)
Central Research Library
Applied Technology Library

Department of Energy Field Office, Oak Ridge

Assistant Manager, Energy Research and Development

External Distribution

M.G. Abdallah, Hercules Advanced Materials and Systems Company, Mail Stop 2343L, P. O. Box 98, Magna, Utah 84044-0098

D. F. Adams, Mechanical Engineering Department, Composite Materials Research Group, University of Wyoming, P. O. Box 3295, Laramie, Wyoming 82071

A. Alexander, Custom Analytical Engineering Systems, Inc., Star Route Box 4A, Flintstone, Maryland 21530

J. M. Augl, Code K-31, Naval Surface Warfare Center, White Oak Laboratory, 10901 New Hampshire Avenue, Silver Spring, Maryland 20903-5000

R. Badaliance, Code 6380, Mechanics of Materials Branch, Naval Research Laboratory, 4555 Overlook Avenue, Southwest, Washington, D.C. 20375-5000

D. L. Bonanni, Ship and Structures and Protection Department, David Taylor Research Center, Bethesda, Maryland 20084-5000

C. E. Browning, Structural Materials, WRDC/MLB, Wright Research Development Center, Wright-Patterson Air Force Base, Ohio 45433-6523

B. P. Burns, Mechanics and structures Branch, SLCBR-1B-M, U. S. Army Ballistic Research Laboratory, Aberdeen Proving Ground, Maryland 21005-5066

A. A. Caiazzo, Materials Sciences Corporation, Union Meeting Corporate Center, 930 Harvest Drive, Blue Bell, Pennsylvania 19422

E. T. Camponeschi, Code 2802, Composites Program Office, David Taylor Research Center, Annapolis, Maryland 21042-5067

J. R. Carlberg, Ship and Structures and Protection Department, David Taylor Research Center, Bethesda, Maryland 20084-5000

R. F. Charette, Ship and Structures and Protection Department, David Taylor Research Center, Bethesda, Maryland 20084-5000

R. O. Claus, Electrical Engineering Department, Fiber and Electro-Optics Research Center, Virginia Polytechnic Institute and State University, 648 Whittemore Hall, Blacksburg, Virginia 24061

S. J. DeTeresa, Lawrence Livermore National Laboratory, Mail Stop L-338, P.O. Box 808, 7000 East Avenue, Livermore, California 94550

D. J. Dorr, Advanced Structures and Materials, McDonnell Douglas Aircraft Company, D.390, Mail Code 1021310, P. O. Box 516, St. Louis, Missouri 63166-0516

S. Earle, 5128, Department of Commerce, National Oceanic and Atmospheric Administration, 14th & Constitution Ave, NW, Washington, DC 20230

D. Flaggs, Lockheed Missiles & Space Company, O/93-30 B/251, 3251 Hanover Street, Palo Alto, California 94304

G. S. Friar, Advanced Technology Section, Research Branch, Benet Weapons Laboratory, Armament Research and Development Center, SMCAR-CCB - Watervliet Arsenal, Watervliet, New York 12189-4050

H. J. Garala, Code 1720.2, David Taylor Research Center, Bethesda, Maryland 20084-5000

J. W. Gillespie, Jr., Center for Composite Materials, University of Delaware, 201 CMSL, Newark, Delaware 19716

R. G. Gilliland, Engineering Materials and Processes, Aluminum Company of America, Alcoa Technical Center, Alcoa Center, Pennsylvania 15069

L. B. Greszczuk, McDonnell Douglas Space Systems Company, Mail Stop 13/3, 5301 Bolsa Avenue, Huntington Beach, California 92647

H. T. Hahn, The Pennsylvania State University, 227 Hammond Building, University Park, Pennsylvania 16802

B. M. Halpin, Jr., Composites Development Branch, SLCMT-MEC, U.S. Army Materials Technology Laboratory, Arsenal Street, Watertown, Massachusetts 02172-0001

M. W. Hyer, Engineering Science amd Mechanics Department, Virginia Polytechnic Institute and State University, 225 Norris Hall, Blacksburg, Virginia 24061

R. F. Jones, Code 1132SM, Office of Naval Research, 800 North Quincy Street, Arlington, Virginia 22217-5000

J. J. Kelly, DARPA/STP-ASTO, Defense Advanced Research Projects Agency, 1400 Wilson Bouievard, Arlington, Virginia 22209

R. Y. Kim, Research Engineer, University of Dayton Research Institute, 300 College Park Avenue, Dayton, Ohio 45469-0168

S. R. Kopf, E. I. du Pont de Nemours & Company, Chestnut Run Plaza, P. O. Box 80702, Wilmington, Delaware 19880-0702

G. Lee, Hitco, Inc., MS15C, 13722 Harvard Place, Gardenia, California 90249

G. F. Leon, Electric Boat Division/General Dynamics, Mail Stop D442, 75 Eastern Point Road, Groton, Connecticut 06340

J. S. Mayes, Ship and Structures and Protection Department, David Taylor Research Center, Bethesda, Maryland 20084-5000

T. Morton, Code 2802, Composites Program Office, David Taylor Research Center, Annapolis, Maryland 21402-5067

R. J. Nuismer, Hercules Composite Structures, Mail Stop X11K4, P.O. Box 98, Magna, Utah 84044-0098

G. P. O'Hara, Applied Math and Mechanics Section, Research Branch, Benet Weapons Laboratory, Armament Research and Development Center, SMCAR-CCB - Watervliet Arsenal, Watervliet, New York 12189-4050

W. Phyillaier, Code 1720.2, David Taylor Research Center, Bethesda, Maryland 20084-5000

V. Peros, Martin Marietta Aero & Naval Systems, Mail Stop 700, 103 Chesapeake Park Plaza, Baltimore, Maryland 21220

E. A. Rasmussen, Code 1720.4 Ship and Structures and Protection Department, David Taylor Research Center, Bethesda, Maryland 20084-5000

D. B. Rogers, School of Engineering and Technology, Tennessee State University, 3500 John A. Merritt Boulevard, Nashville, Tennessee 37209

R. Rockwell, Code 1720, Submarine Structures Division, David Taylor Research Center, Bethesda, Maryland 20084-5000

B. W. Rosen, Materials Sciences Corporation, Union Meeting Corporate Center, 930 Harvest Drive, Blue Bell, Pennsylvania 19422

A. J. Roy, University of Dayton Research Institute, 300 College Park Avenue, Dayton, Ohio 45469-0001

B. E. Sandman, Code 8215, Design and Structures, Naval Underwater Systems Center, Newport, Rhode Island 02841

F. J. Spicola, Code 8215, Naval Underwater Systems Center, Newport, Rhode Island 02841

J. D. Stachiw, Code 9402, Naval Ocean Systems Center, 273 Catalina Boulevard, San Diego, California 92152-5000

J. L. Stachiw, (2), Stachiw Associates, P.O. Box 2343, El Cajon, California 92021

M. S. Stahl, College of Business Adminstration, The University of Tennessee, Knoxville, 8 Humanities Building, Knoxville, Tennessee 37996-0100

S. Starrett, Mechanics Division, Southern Research Institute, 2000 Ninth Avenue, South, P.O. Box 55305, Birmingham, Alabama 35205

K. B. Su, Engineering Technology Laboratory, E. I. du Pont de Nemours & Company, 80304 Experimental Station, Wilmington, Delaware 19880-0304

R. F. Swan, Code 92RL, Advanced Submarine Research and Development, Naval Sea Systems Command, Department of the Navy, Washington, D. C. 20362-5101

S. R. Swanson, Department of Mechanical and Industrial Engineering, University of Utah, 3209 MEB, Salt Lake City, Utah 84112

S. W. Tsai, Department of Aeronautics and Astronautics, Durand Building, Stanford University, Stanford, California 94305

S. S. Wang, National Center for Composite Materials Research, University of Illinois,

216 Talbot Laboratory, 104 South Wright Street, Urbana, Illinois 61801

J. M. Whitney, Mechanics and Surface Interaction Branch, WRDC/MLBM, Wright Research and Development Center, Wright-Patterson Air Force Base, Ohio 45433-6533

I. Wolick, Code 6383, Naval Research Laboratory, Washington, D. C. 20375-5000

Office of Scientific and Technical Information (2), P.O. Box 62, Oak Ridge, Tennessee 37831

—

DATE
FILMED
01/28/92